Volume 21, Number 6

December, 1966

SOVIET ATOMIC ENERGY

АТОМНАЯ ЭНЕРГИЯ
(ATOMNAYA ÉNERGIYA)

TRANSLATED FROM RUSSIAN

CONSULTANTS BUREAU

SOVIET ATOMIC ENERGY

Soviet Atomic Energy is a cover-to-cover translation of *Atomnaya Énergiya*, a publication of the Academy of Sciences of the USSR.

An arrangement with Mezhdunarodnaya Kniga, the Soviet book export agency, makes available both advance copies of the Russian journal and original glossy photographs and artwork. This serves to decrease the necessary time lag between publication of the original and publication of the translation and helps to improve the quality of the latter. The translation began with the first issue of the Russian journal.

Subscription
(12 Issues): $95

Single Issue: $30
Single Article: $15

Order from:

CONSULTANTS BUREAU
227 West 17th Street, New York, New York 10011

SOVIET ATOMIC ENERGY

A translation of *Atomnaya Énergiya*

Volume 21, Number 6 December, 1966

CONTENTS

CONTENTS

(continued)

The Russian press date (podpisano k pechati) of this issue was 12/3/66. Publication therefore did not occur prior to this date, but must be assumed to have taken place reasonably soon thereafter.

THE 1.5-GeV ELECTRON SYNCHROTRON IN TOMSK POLYTECHNIC INSTITUTE

A. A. Vorob'ev, M. N. Volkov, A. G. Vlasov,
V. A. Vizir', I. A. Gabrusenko, M. I. Dvoretskii,
G. I. Dimov, A. N. Didenko, V. V. Ivashin,
V. N. Eponeshnikov, V. A. Kochegurov, V. M. Kuznetsov,
S. A. Kuznetsov, V. N. Kuz'min, B. N. Kalinin,
P. P. Krasnonosen'kikh, N. A. Lashuk, L. I. Minenko,
Yu. K. Petrov, G. A. Sipailov, B. A. Solntsev, G. P. Fomenko,
I. P. Chuchalin, M. T. Shivyrtalov, and P. M. Shanin

UDC 621.384.612

A 1.5-Gev electron synchrotron is described. The synchrotron is of the weak-focusing type with a magnetic-field fall-off index of n = 0.58 The machine operates under pulse conditions, with a repetition frequency of 1 cps. The injector is a 5.5-MeV microtron. A voltage of 240 kV is required to accelerate electrons to 1.5 GeV, and this is designed to be supplied by two resonators. An energy of 1.1 GeV and an accelerated-beam intensity of $1.2 \cdot 10^{10}$ particles per pulse was obtained in 1965 on a synchrotron with one resonator.

Work on setting up the "Sirius" synchrotron in Tomsk Polytechnic Institute began in 1954 on the initiative and under the direction of A. A. Vorob'ev.

The "Sirius" synchrotron (Fig. 1) differs from other analogous accelerators in a number of features. For weak focusing, its energy is comparatively high, and together with the long acceleration period this enables the effect of quantum fluctuations on the motion of the particles in cyclical accelerators to be studied.

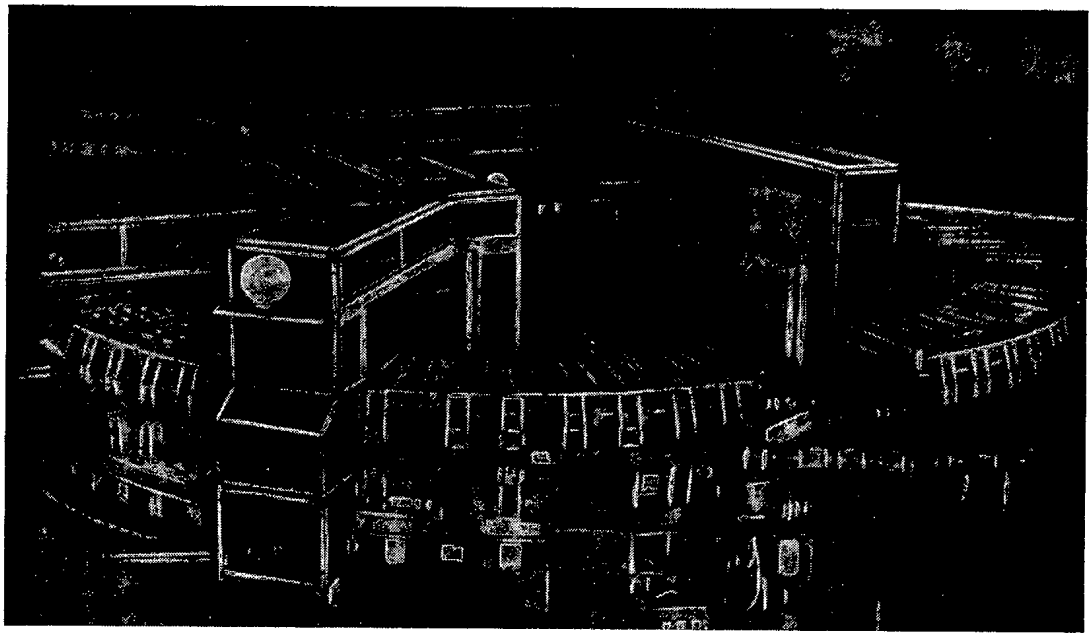

Fig. 1. General view of synchrotron "Sirius."

Translated from Atomnaya Énergiya, Vol. 21, No. 6, pp. 435-439, December, 1966. Original article submitted August 1, 1966.

Injection on the curvilinear part of the magnet was used for the first time. Investigations showed that the difficulties associated with conducting the beam in a stray magnetic field could be overcome, and that the electrical field of the inflector could be made three times lower than that required for injection in the rectilinear gap. This enabled the injection energy to be brought up to 12 or 15 MeV with reasonable voltages on the inflector plates, i.e., to produce a substantial increase in the number of particles accelerated in the synchrotron.

The synchrotron "Sirius" operates under pulse conditions with a repetition frequency of 1 cps, selected from economic considerations. The pulse condition required the development of a high-power switching system (over 60 kVA).

The individual components of the accelerator are described below.

ELECTROMAGNET AND ITS SUPPLY SYSTEM

The electromagnet of the synchrotron consists of four sectors separated by linear gaps free from magnetic field. The radius of the equilibrium orbit in the sectors is 423 cm, the length of the rectilinear part 157 cm, and the magnetic-field fall-off index 0.58.

The electromagnet units of the synchrotron are made of É-12 electrotechnical sheet steel 0.5 mm thick. The maximum induction in the steel is 16,000 G. The required accuracy in manufacturing the plates was achieved by two-stage stamping. Each magnet sector consists of 24 C-shaped units with the gap on the outside. The height of the gap at the radius of the equilibrium orbit is 12 cm. A steel block 60 mm thick serves as base for the sectors.

The blocks are fixed to welded bearing girders, which in turn are fixed into a reinforced-concrete foundation. The blocks are set to an accuracy of ± 0.15 mm in height and ± 0.1 mm in radius. The setting with respect to height is achieved with a hydro-leveling system and with respect to radius by means of special measuring calipers. Magnetic measurements were carried out in all the units before assembly. The order of the units in the sectors was determined from the results of these measurements, on the principle of minimizing the lower harmonics obtained on expanding the magnetic-field inhomogeneities into a Fourier series. The median geometric plane of the units was established to an accuracy of $\pm 1.5 \cdot 10^{-3}$ rad relative to the horizontal and ± 0.2 mm in height. In the radial direction the units were set to an accuracy of ± 0.4 mm. The azimuthal dimension of the magnetic sectors was established with a theodilite, to an accuracy of $3 \cdot 10^{-4}$ rad, by setting the end units of the sectors exactly and varying the dimensions of the individual units inside the sectors. The geometric angle of the sectors equalled $88°59' \pm 1'$. The weight of the active steel in the magnet was 115 tons. The windings of the electromagnet were copper tubes of outer diameter 22 and inner diameter 12 mm. These were cooled with distilled water, the flow being 22 m^3/h.

Correction for the following characteristics of the magnetic field is provided in the synchrotron at the injection stage: magnetic-field index and median surface radial component of magnetic field at each end of the sector, first and second harmonics of inhomogeneities, and effective angle of the sector.

After assembly of the electromagnet, magnetic measurements were made in order to ascertain the required correction parameters. The measuring program included investigations relating to various levels of magnetic field, the azimuthal and radial distributions of field index, the shape of the median surface, and the radial component of the field in the rectilinear gaps.

The magnetic measurements showed that the greatest distortions of magnetic field on injection were due to the residual magnetization of the magnetic circuit, as a result of which the radial distortion of the orbit reached ± 4.8 cm and the magnetic-field fall-off index 1.02. In order to remove the residual magnetization, the electromagnet is demagnetized after each working cycle by the unipolar current pulse of amplitude 400 A flowing through the principal winding of the electromagnet. The greatest vertical distortions of the orbit (up to ± 1.7 cm) at the level of the injection field were due to the Earth's magnetic field in the rectilinear gaps.

After demagnetization, the magnetic-field fall-off index $n = 0.8$, and the radial and vertical distortions of the orbit are ± 1.82 cm and ± 1.7 cm respectively. The magnetic-field corrections system enabled the distortion of the orbit in the vertical plane to be reduced to ± 0.5 cm and that in the

horizontal plane to ± 0.52 cm for low fields. The magnetic-field fall-off index at the level of the injection field equals 0.58 after correction.

For medium and high fields (500 to 12,000 Oe), the distortion of the field is insignificant and lies withing tolerance limits (± 1 cm). The tolerances on the deviation of n were set at ± 0.03 for n = 0.58.

The electromagnet is excited by a condenser-battery discharge into the electromagnet windings via a thyratron switch. The current pulses are of sinusoidal shape with a half-wave period of 84 msec and an amplitude of 5140 A. The pulse repetition frequency is 1 cps. The condenser battery is charged from a controlled rectifier rated at 800 kW, operating on the Larionov principle. In the intervals between current pulses, the condenser battery is charged from 10 to 12.4 kV. The battery comprises 1728 pulse condensers of the IM-3/100 type connected in series-parallel. The current is switched by 18 TR1-85/15 thyratrons connected in antiparallel. Division of the current between the thyratrons is effected by means of two-pin anode dividers. The rate of growth of the magnetic field at the moment of injection is reduced from 450,000 to 110,000 Oe/sec by means of saturation chokes in series with the windings of the electromagnet. The reproducibility of the magnetic field from cycle to cycle is kept within ± 0.2% by stabilization of the voltage on the condenser battery. The demagnetizing pulse is created by a special circuit. This circuit consists of a three-phase rectifier, an 1800-μF condenser battery, and two TR1-85/16 switching thyratrons.

ACCELERATOR CHAMBER AND VACUUM SYSTEM

The accelerator chamber consists of four circular and four straight sections. The circular sections include 16 curved porcelain sectors glued together with an epoxy compound. The conducting coating in the porcelain sections is formed by a film of stannic oxide. The cross section of the working part of the chamber is oval in shape, 23 cm over the radius and 8.4 cm vertical.

The straight parts are made of copper tubes with an internal diameter of 23 cm.

The vacuum chamber is evacuated with four N-5T pumps rated at 4000 liter/sec each and two N-5S pumps rated at 500 liter/sec.

After continuous pumping for 72 h, the vacuum in the middle of the curvilinear parts reaches $3 \cdot 10^{-6}$ mm Hg.

In order to indicate the presence of the electron beam during the initial turns, some 20 different indicating devices (fluorescent grids and probes, Faraday cylinders, shadow flags) are placed in the accelerator chamber; these enable the electron current to be measured and the position of the beam to be determined relative to the cross section of the chamber.

INJECTION SYSTEM

The injector used for the synchrotron is a microtron, giving a beam of 5-MeV (±0.5%) electrons, with a pulse current of 30 to 40 mA and a pulse length of 3 μsec.

The energy of the injected electrons is maintained at the required level by stabilizing the magnetic field of the microtron to an accuracy of ± 0.2%. The electron beam emitted from the microtron is introduced into the accelerator along the vacuum tract. The beam is focused in the tract by means of two pairs of quadrupole lenses, enabling the over-all focal length to be varied by regulating the current in the windings. Two magnetic correctors placed after the lenses provide a parallel displacement and a change in the angular direction of the beam in the vertical and horizontal planes. An interrupter and collimator placed in the tract make it possible to limit both the geometrical dimensions and duration of the beam while the synchrotron is being adjusted. The electrons are introduced into the accelerator chamber by means of a straight electrostatic inflector placed in a gap of the electromagnet. The inflector plates are divided into three parts, to which voltages of 5.9 and 13 kV are supplied from separate sources (the gap between the inflector plates is 1 cm). The introduction of particles along the tangent to the orbit in the magnetic sector (in contrast to introduction in the linear gap) enabled the electric field between the inflector plates to be considerably reduced.

The supply to the principal units of the microtron and injection tract is stabilized to an accuracy of ± 0.2%, and that of the inflector to ± 0.05%.

ACCELERATING SYSTEM

The electrons are accelerated in the synchrotron by two toroidal brass resonators, in each of which a hf voltage with an amplitude of 120 kV is designed to be excited. The resonators are constructed in such a way that their working cavities (situated in vacuum) experience no mechanical loading. For a working frequency of 36.5 Mc/sec, the Q of the resonator equals 2000 and the shunt resistance 50 kΩ. The resonator incorporates elements for adjusting the frequency and eliminating hf-resonance discharges. The resonators are excited from the final stages of a hf generator, the excitation pulse being fed to the first resonator at the instant of the quasi-betatron state and to the second after 20 msec, when the radiative energy losses of the electrons become considerable. Quite stringent demands are imposed on the rate of voltage rise in the hf generator. For an equilibrium accelerating voltage of 1500 V, the optimum value of the initial voltage equals 4500 V and this must be established in 1 to 2 μsec.

In order to satisfy the demands laid on the form of the hf voltage envelope, anode-grid-cathode modulation is used in the final stage feeding the first resonator. The anode modulation is effected by a rectangular voltage pulse, the grid modulation by a voltage determining the law of amplitude variation of the hf voltage during acceleration, and the cathode modulation by a short pulse in the initial period of acceleration, in order to reduce the growth time of the amplitude of the hf voltage in the resonator gap. In the final stage exciting the second resonator, anode-grid modulation is used. The final stages comprise tubes of the GU-4A type and are set in the center of the accelerator.

The hf generator is based on a multistage circuit. The hf tract is divided into two channels at a high power level after the penultimate stage. The generator power is 160 kW.

ACCELERATOR CONTROL AND ARRANGEMENT

The operation of the individual systems of the accelerator are controlled by a synchrogenerator. The control-pulse generation system consists of Permalloy magnetic-field detectors, turns encircling the electromagnet, an integrator, a delay system, and a control-pulse shaping circuit. The corresponding pulses are tied to the value of the magnetic field, with an accuracy of ±0.02% at low and ±0.1% at high fields. The stability of the control-pulse generating system is kept within ±0.002% by means of a standard-voltage source (50 V).

The operation of the magnet-supply system is controlled by a master generator giving pulses at a frequency of 1 cps.

The electron synchrotron, the electromagnet-supply system, and the central control desk are situated in individual rooms with a total area of 750 m^2. In order to reduce the thickness of the protective walls and the background of radioactive radiation outside the synchrotron room, the floor of the accelerator room is depressed 3 m below ground level. In addition to this, the synchrotron room is surrounded by an earth rampart 2 m high on the outside. Alongside the synchrotron room and at the same level is an experimental room into which beams of high-energy γ-radiation are directed.

STARTING THE ACCELERATOR

In the course of preparatory work prior to starting the synchrotron, the motion of the electrons in the accelerator chamber was studied. The first turns of the beam were adjusted at small injection currents, at which the background of γ-radiation fell below the tolerance level and enabled the synchrotron staff to observe the position of the electrons in the chamber visually by means of fluorescent grids and probes. Conditions were dangerous only near the microtron injector.

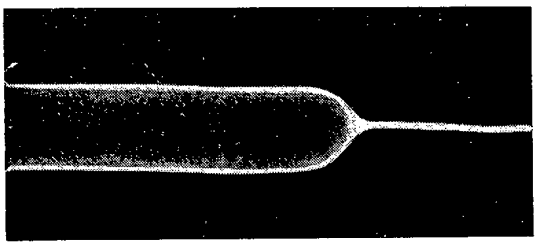

Fig. 2 Oscillogram of signal from the magnetic pickups.

For large injection currents, a television-based remote-observation system was used.

The first rotation of the electrons was obtained at once by setting up the calculated currents in the magnetic-field correction systems, the calculated voltages on the inflector plates, and the calculated injection phase.

The accelerator was started with a slightly reduced voltage on the electromagnet (10.4 instead of 12.4 kV),

using one resonator, in which a hf voltage with an amplitude of the order of 50 to 80 kV was excited. Under these conditions, the electrons were accelerated to an energy of the order of 1.1 GeV. Further increase in the energy of the accelerated electrons was limited by the amplitude of the hf voltage on the resonator.

In order to measure the circulating current, two magnetic pickups, comprising annular coil-bearing magnetic conductors, are set in one of the straight parts of the vacuum chamber. During injection and the quasibetatron state, the current is measured by means of a pickup with a Permalloy core. The pickup reproduces pulses up to 10 μsec long without noticeable distortions. The current of the bunched beam is measured during acceleration by means of a ferrite pickup tuned to a bunch-transmission frequency of 36.5 Mc/sec. The windings of the pickups are connected in series; the signals from these are amplified by a preamplifier and fed to a control-desk oscillograph, on which the current may be observed at any instant from injection to the end of acceleration. Figure 2 represents an oscillogram of a signal from the magnetic pickups, showing that there are no serious losses of electrons during acceleration.

For a 20-mA current taken from the microtron, some 10 to 12 mA were introduced into the chamber. The current built up in the quasibetatron state was of the order of 100 mA. The intensity of the electron beam at the end of acceleration was $1.2 \cdot 10^{10}$ particles per pulse.

This intensity is not the maximum possible for the synchrotron in question. The microtron operates in a comparatively easy condition; its amplitude and current-pulse length may be made greater. There are also other reserve conditions for increasing the accelerated charge.

At the present time, the construction of new resonators is being completed, and work on transforming the electromagnet supply system into the nominal state is being pursued; a new and higher-energy microtron is also being prepared, and other work is continuing with a view to providing the accelerator with its designed parameters.

LINEAR INDUCTION ACCELERATOR

A. I. Anatskii, O. S. Bogdanov,
P. V. Bukaev, Yu. P. Vakhrushin,
I. F. Malyshev, G. A. Nalivaiko,
A. I. Pavlov, V. A. Suslov, and
E. P. Khal'chitskii

UDC 621.384.622

The construction and operating principles of a heavy-current linear induction accelerator yielding 3-MeV electrons and pulse currents up to 200 A are described. Results obtained on one section of this accelerator are presented. The electron current is 180 A (pulsed) with an energy of 485 keV; the pulse duration at a level of 0.95 is 0.35 μsec.

The creation of electron accelerators with beam currents of hundreds and thousands of amperes makes it possible to study the energy stored in a beam of accelerated electrons. Such accelerators enable us to study the creation and maintenace of hot plasma [1] and also to explore possible new methods of acceleration [2]. Such investigations demand a relativistic electron beam of considerable extent with a uniform particle density over its whole length. Such beams may be obtained by the induction method of acceleration proposed by Buwers in 1923 [3]. This method enables us to set up an accelerator possessing the advantages of waveguide-type linear electron accelerators, especially as regards the simplicity of introducing and extracting the beam, and the possibility of increasing the energy by adding to the number of identical sections. In addition to this, with video-pulse operation of the accelerator, the focusing of the beam is considerably simplified, and practically all the particles may be drawn into the acceleration condition for any injection energy.

In 1962 members of the D. V. Efremov Scientific-Research Institute of Electrophysical Apparatus (NIIÉFA) designed a linear induction accelerator, calculated to produce an energy of 3 MeV and pulse currents up to 200 A. The first section of this accelerator was made and set up in 1963. Experience in making and setting up the first section enabled us, to a certain extent, to overcome the technological difficulties of production and to refine the operating characteristic of the accelerator. The experience thus built up enabled us to initiate manufacture of the whole complex of equipment.

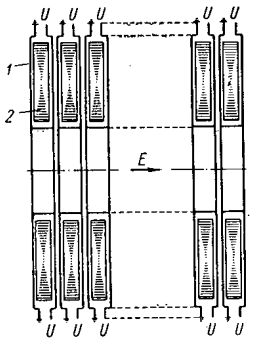

Fig. 1. Accelerator system: 1) exciting winding; 2) inductor core.

Assembly and adjustment work is being carried out at the present time. The starting of this accelerator enables us to indicate its various characteristics and advantages more fully, and opens the way to a wider use of the heavy-current induction accelerator in various fields of investigation.

OPERATING PRINCIPLES OF THE ACCELERATOR

The operating principles of the linear induction accelerator are based on the use of an electrical eddy field excited in the system for the acceleration of the electrons. The system consists of several ring-shaped transformers (Fig. 1).

It is obvious that, when there is a simultaneous change of magnetic flux in the transformer cores (inductors), an electrical eddy field

$$E = -\frac{n}{l} Q \frac{dB}{dt} \qquad (1)$$

is excited on the axis of the system, where E is the eddy field, n is the number of inductors in the system, l is the length of the system, Q is the cross section

Translated from Atomnaya Énergiya, Vol. 21, No. 6, pp. 439-445, December, 1966. Original article submitted April 14, 1966.

of the inductor core, and dB/dt is the rate of change of induction in the core. In order to obtain a relativistic beam of electrons with a charge density uniform over its whole length, we must ensure a linear variation of induction with time. In this case expression (1) has the form

$$E = -\frac{n}{l} Q \frac{\Delta B}{\tau_i}, \tag{2}$$

where ΔB is the induction increment, τ_i being the time for the rise in induction. The energy possessed by an electron in this system is

$$W = e \int_0^l E\, dl = enQ \frac{\Delta B}{\tau_i}, \tag{3}$$

where e is the charge on the electron. Constant rate of change of induction may be ensured by feeding the primary winding of the inductor with a voltage of rectangular form and a pulse length τ_i.

In order to obtain an accelerating field of hundreds of kV/m with reasonable accelerator dimensions, the value of $\Delta B/\tau_i$ should be 10^6 to 10^7 T/sec, which makes considerable demands on the material of the cores and switching equipment.

The geometrical dimensions of the accelerating system are chosen in accordance with the given inhomogeneity of particle energy $\Delta W/\Delta W_K$ at the output, on the assumption that the particles are accelerated without any change in the radial coordinate:

$$\frac{R}{l} \leqslant 4 \left(\frac{R}{r}\right)^2 \frac{\Delta W}{W_K}, \tag{4}$$

where R is the average radius of the inductor and r is the radius of the electron beam.

The maximum possible current of accelerated electrons in the apparatus, assuming the existence of focusing sufficient to compensate the repulsive effects of space charge, is mainly determined by the power of the switching element in the primary circuit of the inductor; at the present time this may be brought up to 1000 A/pulse, a value unattainable in accelerators of other types. This is one of the principal advantages of the linear induction accelerator.

CONSTRUCTION OF THE ACCELERATOR

The arrangement of the linear induction accelerator is shown in Fig. 2. The accelerator consists of a series of accelerating sections (Fig. 3a, b). Each section consists of 12 inductors. These are fixed with rubber gaskets in such a way that a hermetic cavity capable of sustaining a vacuum of $5 \cdot 10^{-6}$ mm Hg

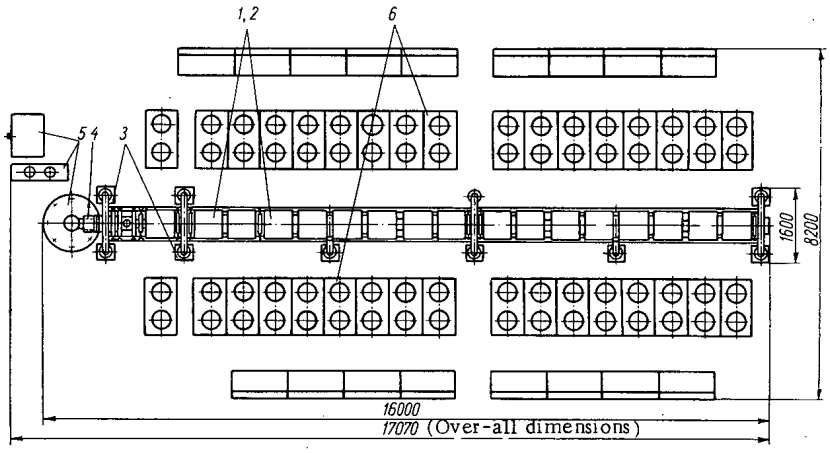

Fig. 2. Arrangement of principal equipment. 1), 2) Accelerating sections with focusing system; 3) vacuum pumps; 4) electron gun; 5) electron-gun pulse supply (spark gap, shaping line, pulse transformer); 6) pulse supply for accelerating sections.

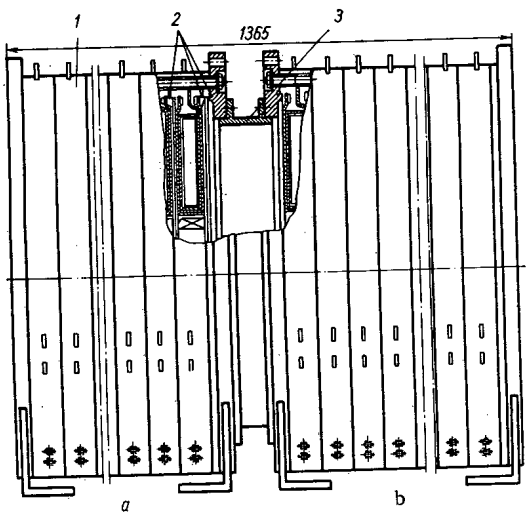

Fig. 3. Accelerator sections: 1) inductor; 2) vacuum sealing; 3) connecting tube.

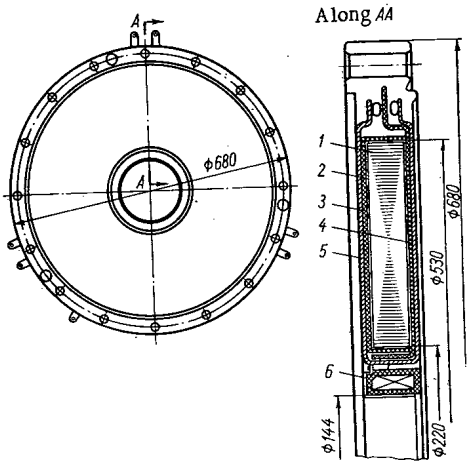

Fig. 4. Inductor: 1) core; 2) synthetic rubber; 3), 4) insulating washer; 5) exciting winding; 6) focusing coil.

is formed inside the section. This construction of the accelerator section eliminates the necessity of a special vacuum tube. The individual sections are connected in pairs by special tube systems. In the gaps between the units so formed are pumping systems and beam-detecting devices. As there was insufficient data regarding the reliability of operation of the sections over a long period of time when the accelerator was being developed, it was considered necessary to provide for the possibility of placing a vacuum tube (which clearly reduces the aperture of the accelerator) inside the sections.

The arrangement of the inductor is shown in Fig. 4. The core is made of 50NP alloy strip 0.02 mm thick. The core is wound on a special machine, in which an insulating layer of magnesium oxide is deposited by cataphoresis at the same time. After winding, the core is annealed in a vacuum furnace in accordance with a special program, with a maximum temperature of 1150 ± 20°C. The cores so prepared have the following characteristics:

space factor	68 to 70%
saturation induction	1.45 T
pulsed induction increment(with remagnetization)	1.8 T

After annealing, the core is placed in insulating washers made of glass-mica. Synthetic rubber is poured into the gap between the core and washers. The joints between the washers are stopped with an epoxy compound. The insulating washers and rubber layers ensure the necessary electrical insulation of the core from the exciting coil and also protect it from mechanical and thermal stresses, thus preserving the magnetic characteristics while the inductor is being manufactured, transported, and used.

The exciting winding is made in the form of a torus of rectangular cross section (in agreement with the shape of the core). This shape of winding ensures minimum leakage fields and a reasonably good outlet for the heat evolved in the core; it also enables the inductor to be made in the form of a vacuum-tight element.

All the components of the inductor are fixed with an epoxy compound, the composition of which is chosen so as to ensure minimum gas evolution from the surface of the inductor and minimum shrinkage on application.

The focusing system consists of several cylindrical coils, each of which is fixed on the inner side of the inductor. These coils create an axially-symmetric magnetic field which compensates the mutually-repulsive forces in the space charge of the beam. The value of the field is chosen so as to conform with Brillouin flow; in the case under consideration, with a beam diameter of about 3 cm, the field should equal 28,000 A/m.

3	4	68	72142
DATE			INVOICE NO.

PLEASE RETURN COPY OF INVOICE WITH PAYMENT.
RETURNS NOT ACCEPTED EXCEPT
BY WRITTEN PERMISSION. PLEASE ENCLOSE
ORIGINAL PACKING SLIP OR SHOW ABOVE
INVOICE NUMBER.
TERMS: NET

NO. OF SUBS	DESCRIPTION	VOL.	YR.	STOCK NO.
	FOR THE ENGLISH TRANSLATION OF THE U. S. S. R. JOURNAL			
1	SOV ATOMIC ENERGY 20 21		66	265
	JAE, 1966, vol. 20, #1-6, vol. 21, #1-6			

LABEL - PACKING LIST

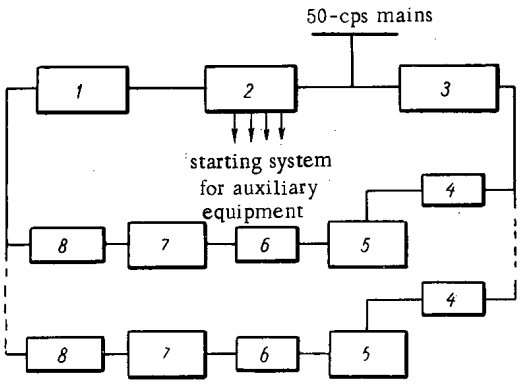

Fig. 5. Pulse supply system for the inductors: 1) amplifier; 2) synchronization unit; 3) demagnetizing unit; 4) pulse-limiting filter; 5) load (group of three inductors); 6) measuring pickups (Rogowski belt and voltage divider); 7) principal modulators; 8) sub-modulators.

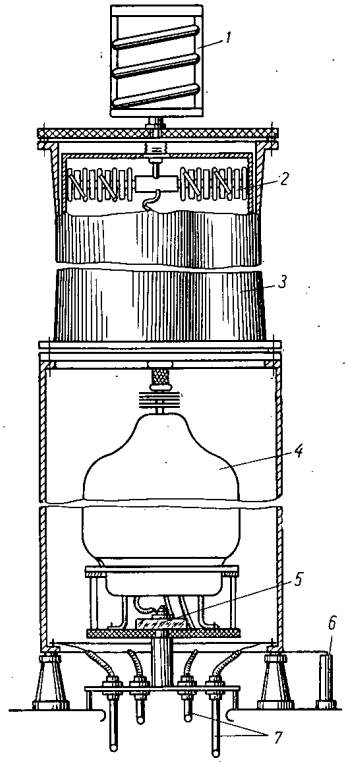

Fig. 6. Principal modulator: 1) charging resistance; 2) section of shaping line; 3) shaping line; 4) switching system (pulse thyratron); 5) Rogowski belt; 6) pulse voltage divider; 7) coaxial cables.

The vacuum system is the same as those normally used in accelerator technology; it enables a vacuum of 5 to $7 \cdot 10^{-7}$ mm Hg to be maintained in the electron-gun region and $5 \cdot 10^{-6}$ mm Hg in the accelerating sections.

The electron gun used comes from a standard klystron. On emerging from the gun, the electron beam has the following parameters: current 200 A, energy 300 keV, diameter 3 cm.

PULSE SUPPLY SYSTEM

The linear variation of magnetic flux in the inductor cores is effected by means of a high-voltage short-rectangular-pulse shaping system.

Bearing in mind the available switching devices and magnetically-soft materials, the following pulse parameters were chosen: pulse length 0.5 μsec, load voltage 15 kV.

The pulse supply system is illustrated schematically in Fig. 5. The principal modulator, of the coaxial type (Fig. 6), consists of a shaping line and hydrogen thyratron. This serves as a source of supply for three parallel inductors. The total number of modulators is 68. Owing to the nonlinear variation of load during the pulse, a hyperbolic shaping line [4] with links of identical capacity, ensuring a pulse of rectangular shape at the inductors, is employed. The shaping line consists of eight or nine links. Each link is assembled from 28 ceramic condensers, and the capacity of a link is about 5000 pF. The shaping lines are supplied from a 35-kV rectifier through charging resistances.

The electromagnetic energy is transferred from the modulator to each inductor by three coaxial cables connected at three points 120° apart. The power of the supply system is sufficient to operate a linear induction accelerator with a frequency up to 50 cps. The synchronization unit has five output channels for starting the principal modulators, injector, oscillograph, and other components of the apparatus. All the channels are electrically connected by means of a common input to a selected phase of the mains voltage supply. The pulses of the various channels may be arranged relative to one another by means of controlled delay lines. Demagnetization of the inductors is effected by means of a current of mains frequency. The demagnetizing circuit includes a high-voltage pulse-limiting filter. The current and voltage pulses are measured by a double-beam oscillograph, the signals for which come from the Rogowski belt and pulse voltage divider.

RESULTS OF TESTS ON AN ACCELERATING SECTION

The calculated data obtained during the development of the accelerator were verified with respect to the operation of the injection section (Fig. 7).

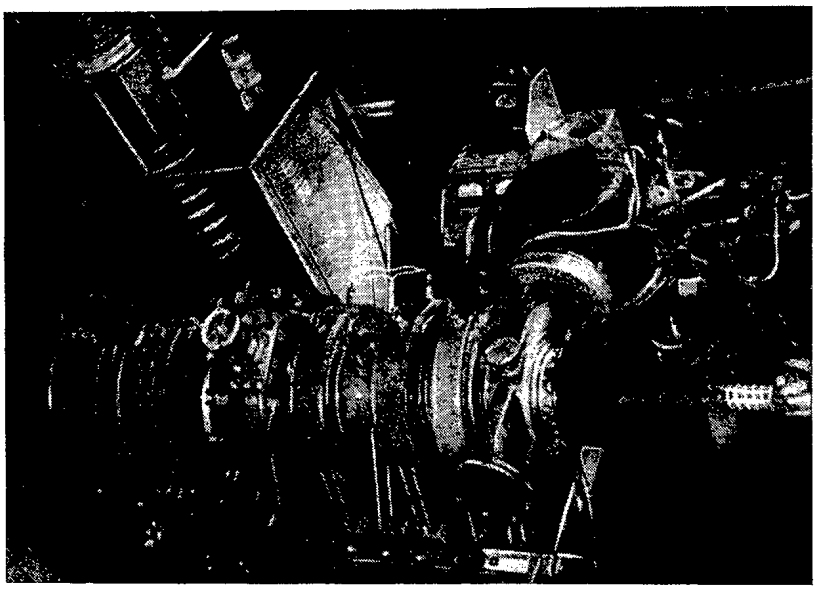

Fig. 7. Injector section.

Passing from right to left, the photograph shows: the electron gun in its insulated oil tank, the vacuum tube, four focusing lenses, and one acclerating section consisting of 12 inductor-

After adjusting the injector section, its efficiency was determined in a continuous 75-h run under rated conditions. The preliminary adjustment included vacuum-conditioning of the whole volume, production of the calculated value of beam current, selection of the current in the focusing system so as to obtain the best transmission of the beam, selection of the shaping-line components so as to obtain a rectangular voltage pulse, and synchronization of the modulators, electron gun, and measuring equipment. The section was tested in conjunction with the vacuum tube, and the vacuum parameters of the section were also tested without the accelerating tube.

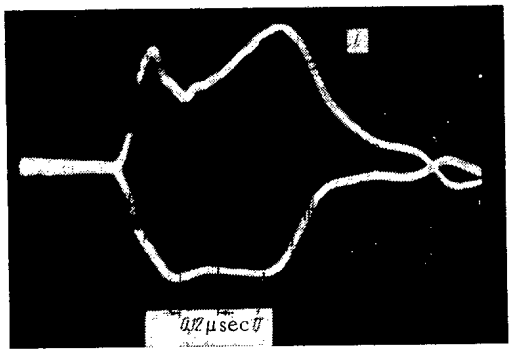

Fig. 8. Oscillogram of current (i) and voltage (U) pulses obtained for one group of inductors.

In order to make best use of the magnetic properties of the cores, attention was paid to ensuring that the groups of three inductors supplied from one modulator should have identical V/A pulse characteristics. In order to ensure that the nonuniformity of the flat part of the voltage pulse should not exceed 5%, it proved necessary to adjust the wave impedances of the sections of shaping line by varying their inductance. Figure 8 shows an oscillogram of the voltage U and current i of one group of inductors.

On average, the length of the leading edge of the pulse equals 0.18 μsec, that of the flat part 0.35 μsec, and the amplitude of the voltage 15·5 kV. Adjustment of the delay lines in the starting channels of each sub-modulator ensured simultaneous operation of all the modulators (to within 0.05 μsec).

Figure 9 shows the cathode emission current as a function of voltage U_a. Tests confirmed that the life of the cathode was considerably affected by the presence of oil vapor in the region surrounding it. We see from curves 3 and 4 that the transmittance of the beam through the system reaches 0.9. The optimum longitudinal focusing field equals 26,000 A/m, in good agreement with computed data. The field in the cathode region is also almost zero, and this corresponds to the conditions for the existance of Brillouin flow. The beam diameter at the collector equalled 15 to 20 mm (Fig. 10). The data presented were obtained by measuring the total emission current of the cathode with an oscillograph, the input signal for this being taken from a resistance in the secondary circuit of the gun pulse transformer. On

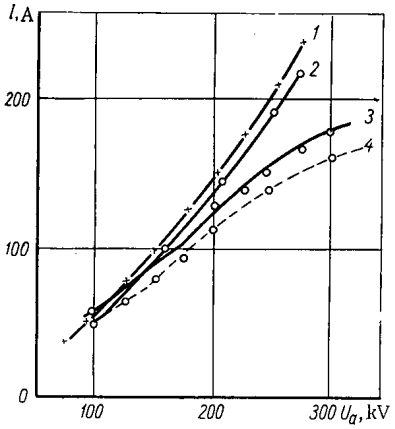

Fig. 9.

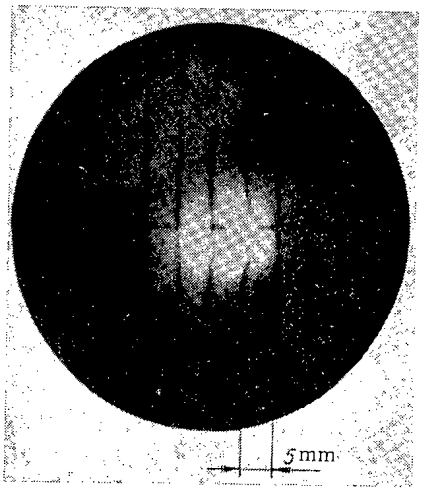

Fig. 10.

Fig. 9. Cathode-emission (1-3) and collector (4) currents: 1) calculated curve for perveance $P = 1.7 \cdot 10^{-6}$ A/V$^{3/2}$; 2) experimental curve obtained with a vacuum of 5 to $7 \cdot 10^{-7}$ mm Hg in the cathode region; 3) averaged experimental curve taken over five cathodes; 4) average collector current obtained for five experiments.

Fig. 10. Trace of the beam on a fluorescent screen beyond the collector.

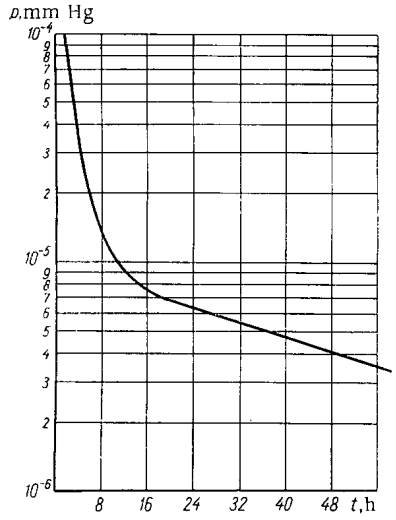

Fig. 11. Pressure inside the acceleration section (without the tube) as a function of pumping time.

emerging from the section, the beam fell on a collector; the current was similarly measured by means of an oscillograph and a resistance in the collector circuit. The shape and position of the beam were observed on a fluorescent screen lying behind the tantalum (collector) plate. The energy of the accelerated-electron beam was estimated from the sum of the inductor voltages and also from the collector-current increment due to the increase in electron velocity. The energy values measured by the two methods agreed closely.

Figure 11 shows the pressure/pumping-time curve of the section in the absence of a vacuum tube. The pressure was measured at the end of the section furthest from the vacuum pump.

The following data were obtained on testing the induction-accelerator section:

Maximum current of accelerated electrons	180 A
Maximum energy of injected electrons	300 keV
Energy of accelerated electrons	485 keV
Gun-current pulse length	2.2 μsec
Accelerating-voltage pulse length	0.35 μsec
Leading edge of accelerating-voltage pulse	0.18 μsec
Average accelerating-field gradient	310 kV/m
Diameter of accelerated beam (at exit)	2 cm

The following members of the staff of NIIÉFA took part in the tests on the first section, in addition to the authors of this article: P. A. Alekseev, L. M. Andrezen, A. V. Belyaeva, O. D. Volodin, M. A. Gashev, V. K. Gagen-Torn, N. K. D'yachenko, N. V. Toloknov, Yu. V. Lebedev, A. A. Markhel'. P. G. Moreev, A. V. Popokovich, A. N. Popov, S. V. Promyshlyaev, G. L. Saksaganskii, Ya. L. Mikhelis, and A. T. Chesnokov.

The authors are grateful to Academician V. I. Veksler and V. P. Sarantsev for interest and help in this work.

LITERATURE CITED

1. N. Christofilos, In the book "Transactions of the International Conference on High-Energy Accelerators" (Dubna, 1963) [Russian translation]. Moscow, Atomizdat, p. 1073 (1964).
2. V. I. Veksler, Atomnaya Énergiya, 2, 427 (1957).
3. A. Buwers, Elektrische Höchstspannungen, Berlin, § 15, S. 83 (1939).
4. O. N. Litvinenko and V. I. Soshnikov, Theory of Nonuniform Lines and Their Use in Radio Technology [in Russian]. Moscow, "Sovetskoe radio" (1964).

TIME STRUCTURE OF PARTICLE BEAMS OBTAINED FROM THE SYNCHROCYCLOTRON IN THE UNITED INSTITUTE OF NUCLEAR RESEARCH (OIYaI)

V. G. Zinov, S. V. Medved',
and E. B Ozerov

UDC 621.384.611.1

The form of the intensity-distribution curves (plotted against time) was determined for particle beams extracted from the United Institute of Nuclear Research synchrocyclotron. The time structure associated with the frequency of the accelerating voltage was measured for the same beams. There was no radio-frequency structure in beams of secondary particles under the slow extraction conditions realized in the synchrocyclotron.

A study of the time structure of an accelerator beam is of considerable interest. From one point of view, a knowledge of this structure aids our understanding of the characteristics of the accelerator and enables us to choose methods of improving its operation. From another point of view, a study of this structure enables us to make a more rigorous estimate of the possibility of carrying out physical experiments. In addition to this, the demands laid on the parameters of the recording apparatus are to a great extent determined by the time structure of the particle beams.

It is well known that the synchrocyclotron operates cyclically. The time structure of the extracted beams has a double periodicity, associated, first, with the repetition frequency of the acceleration cycles (macrostructure) and, secondly, with the frequency of the accelerating voltage (microstructure).

In this paper we shall study methods of examining the macro- and microstructures and shall also discuss experimental results.

MACROSTRUCTURE

Under ordinary conditions, the repetition frequency of acceleration cycles in the OIYaI synchrocyclotron equals 120 sec^{-1}. The acceleration time is 4.0 msec. The period of extracting the particles from the accelerator, however, depends to a considerable extent on how this is done.

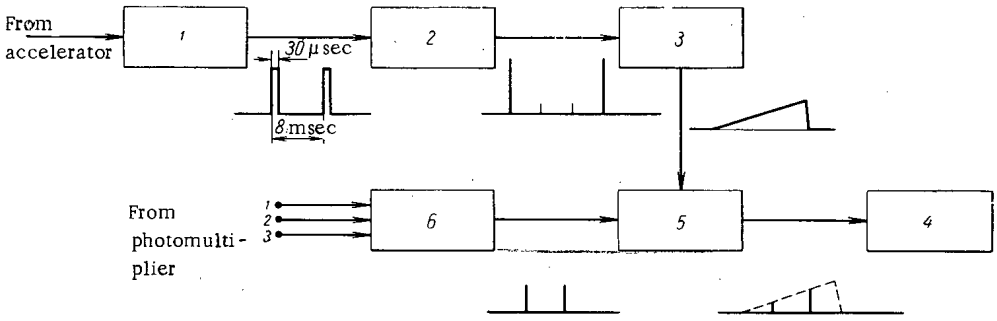

Fig. 1. Block diagram of apparatus for measuring the macrostructure of particle beams (voltage diagrams correspond to various points in the system); 1) frequency discriminator; 2) frequency divider; 3) saw-tooth voltage generator; 4) amplitude analyzer; 5) time selector; 6) coincidence circuit.

Translated from Atomnaya Énergiya, Vol.21, No.6, pp. 445-449, December, 1966. Original article submitted April 12, 1966.

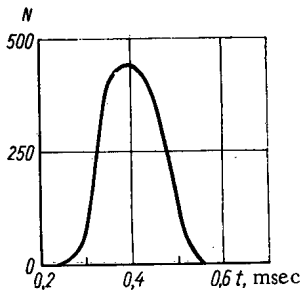

Fig.2. Macrostructure of extracted proton beam.

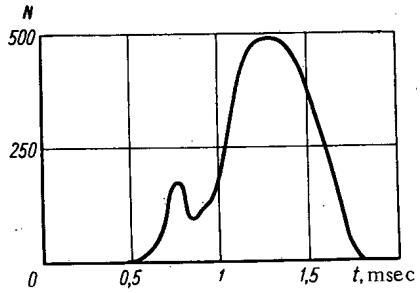

Fig.3. Macrostructure of extracted secondary-particle beam (muons with a momentum of 150 MeV/c).

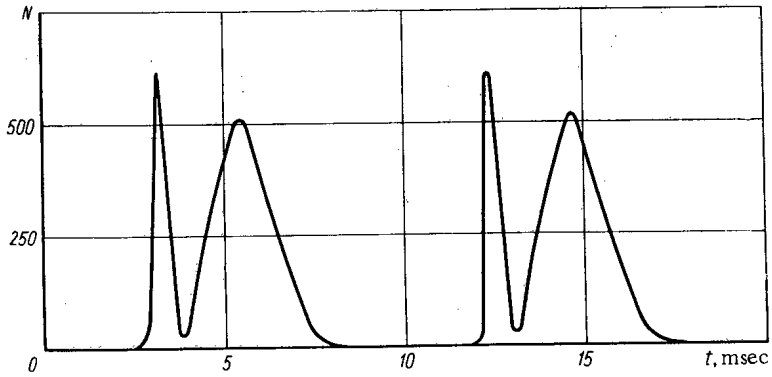

Fig.4. Macrostructure of a muon beam extracted from the accelerator by means of a slow-extraction system ("stretching" the beam).

The time macrostructure was studied by the same method for all beams. A block diagram of the apparatus is shown in Fig.1. The beam particles were recorded with a telescope consisting of three scintillation counters set for coincidence. Strict time connection to the acceleration cycle was established by means of a frequency discriminator. Adjustment of the discriminator circuit enabled us to control the moment of connection, which was taken close to the region with the greatest rate of frequency change. For each acceleration cycle, pulses 30 μ sec long were obtained at the output of the discriminator, and by way of a repetition-frequency divider these started a saw-tooth voltage generator. The signal from the coincidence circuit fell on the input of a time selector, and the saw-tooth voltage was applied to the other input. On arrival of a pulse from the coincidence circuit, the time selector produced a signal with an amplitude proportional to the instantaneous level of the saw-tooth voltage, and this secured a time-amplitude transformation. The spectrum of output pulses from the selector was recorded on a 256-channel amplitude analyzer [1]. The time scale of the analyzer was determined by the saw-tooth voltage rise time. In certain cases, several successive operating cycles of the accelerator had to be recorded instead of one. This condition was realized with the help of the pulse-repetition frequency divider and frequency discriminator.

Figure 2 show the measured intensity distribution of an emergent proton beam. Special extraction characteristics were responsible for the short extraction time (160 μsec).

Secondary particles are usually obtained on the inner target of the synchrocyclotron. The intensity-distribution curve of the extracted beam is principally determined by the velocity of the bunch of

accelerated protons approaching the target and by the spectrum of radial-oscillation amplitudes. These factors result in a long extraction time for the secondary particles. Figure 3 shows the measured intensity distribution of the extracted muon beam. The average extraction time was 620 μsec. The initial intensity peak was associated with electrostatic focusing in the center of the machine [2].

In carrying out experiments, it is desirable to increase the period of extracting particles from the accelerator as much as possible. This is important in order to reduce the loading of the apparatus (reduce the losses on account of dead time) and produce a lower density of background radiation. A novel means of slow beam extraction was introduced in the OIYaI accelerator in 1965 [3]. The essence of this is the additional forced radial oscillations of the proton bunch are excited in the final orbits of the accelerator by means of a time-varying magnetic field. This method enabled us to increase the meson extraction time to 2500 μsec, as may be seen in Fig.4. The duty factor attained is 25% for 70% of the beam intensity.

MICROSTRUCTURE

At the end of the acceleration cycle, the working frequency of the accelerator slowly changes from 14.2 to 14.0 Mc/sec. The average period of the beam microstructure is about 71 nsec.

A photographic measuring method was employed. Figure 5 shows the block diagram of the experiment. As before, rough synchronization of the apparatus with the accelerator was effected by means of a frequency discriminator. The repetition frequency of the pulses from the discriminator was reduced 15 times by means of a frequency divider. The division factor was determined with a high-speed photographic system. A shift univibrator selected the desired part of the particle-extraction process and a "gate"-width univibrator gave the duration of the part to be studied. The pulse from the second univibrator was applied to one of the inputs of the coincidence circuit, while pulses from 56AVP photomultipliers lying in the particle beam were applied to the other two. The signal from the output of the coincidence circuit started the time base of five-beam oscillograph [4]. The same pulse controlled the operation of the photographic system.

The hf voltage from the accelerator was applied to one pair of vertical-deflection plates of the oscillograph tube. The second and third plates received pulses from the photomultipliers through wide-band amplifiers of the UZ-5 (UR-4) type. The fourth and fifth beams were not used. The horizontal sweep of all the beams came from a single generator (sweep velocity about 10 nsec/cm).

One of the photographs obtained appears in Fig.6. In the course of preliminary inspection, we rejected all pictures recording more than one pulse in any beam. In the remaining pictures, we measured the distance from point A (the intersection of the rising branch of the sine wave with the second beam) to point B (the intersection of the tangent to the leading edge of the photomultiplier pulse with the continuation of the same beam). The period of the sine wave (section AC) was measured every 100 pictures. The ratio of sections AB and AC gave the relative phase of the instant of arrival of the particle. The absolute phase was not determined. The accuracy of the measurements (including inspection) was $\pm$ 0.8 nsec. In all, 10,000 photographs were analyzed.

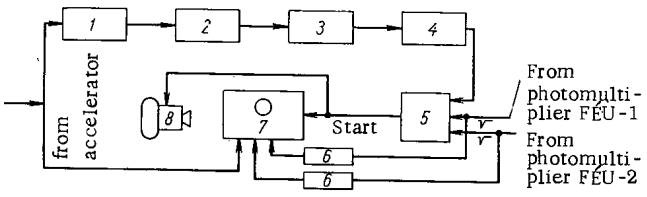

Fig.5. Block diagram of apparatus for studying the microstructure of extracted beams. 1) Frequency discriminator; 2) frequency divider; 3) shift univibrator; 4) "gate" univibrator; 5) coincidence circuit; 6) amplifiers; 7) five-beam oscillograph; 8) photographic system.

Microstructure measurements were made for proton, muon, and pion beams [5]. The structure of particle beams at the output of the μ-meson tract was also studied [6]. All the experiments were made with full intensity of the inner beam of the accelerator, at the

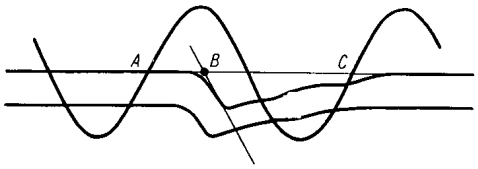

Fig.6. Photograph of an event obtained from the oscillograph screen.

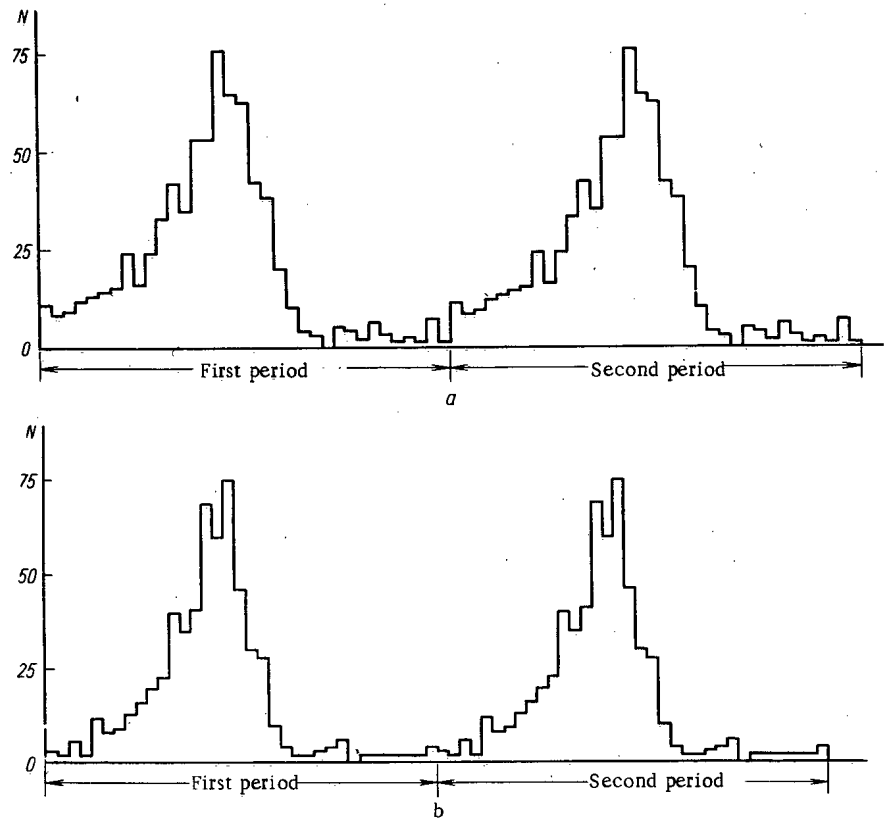

Fig.7. Microstructure of a pion beam at the output of the μ-meson tract: a) start of the extraction process; b) end of the extraction process.

beginning and end of the extraction process. Some results of the measurements are presented in Fig.7 a, b. For the sake of clarity, the histogram corresponding to one period is repeated for a second period.

The asymmetry of the resultant time distributions for the beams of secondary particles is very noticeable. This effect is due to the repeated passage of protons of the inner bunch through the target. The existing nonmonochromatic nature of the beams cannot seriously distort the form of these distributions. It is an interesting point that the average width of the distribution at the beginning of extraction is considerably greater than that at the end: 15.5 as compared with 12.5 nsec.

Figure 8 gives the time distribution of intensity in a micropulse of an extracted proton beam. Although the shape of the curve differs from that corresponding to the secondary particles, the average length of the micropulse is 15 nsec as before. The distribution may be closely approximated by a Gaussian curve with a mean-square spread of $\sigma = 5.5$ nsec.

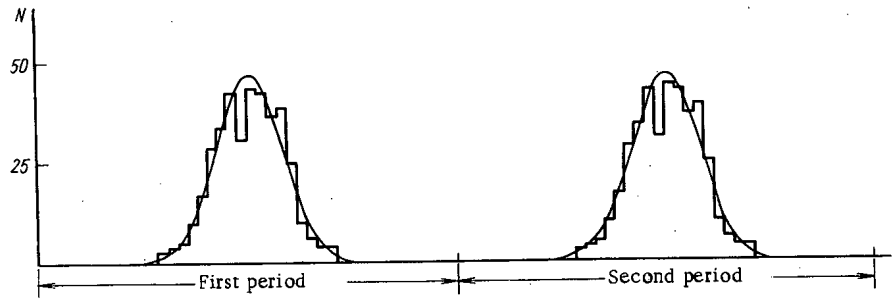

Fig.8. Microstructure of an extracted proton beam.

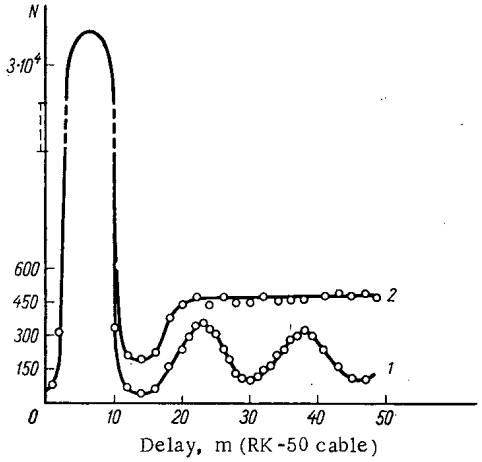

Fig.9. Curves of delayed coincidences for various parts of the macrostructure of a muon beam.

We also made some experiments on a "stretched" beam of secondary particles. The two intensity-distribution peaks in the macropulse shown in Fig.4 correspond to two different extraction mechanisms. The first, narrow peak corresponds to the drifting of a bunch of accelerated protons to the inner target in the presence of the hf voltage on the D of the accelerator. Then the voltage is taken off and a current pulse is fed into the special coils of the beam-stretching system. The second, wide peak corresponds to the drift of the proton bunch resulting from the perturbation introduced into the magnetic field of the accelerator by the coils [3].

When the hf on the D is removed, the bunch of protons inside the apparatus drifts apart very rapidly in azimuth as a result of their velocity spread, and the microstructure of the extracted beam vanishes. This was verified in experiments with a coincidence circuit lying in the beam of muons from a μ-meson tract. First, just the initial peak was separated out by means of the synchronization system. The ordinary curve of delayed coincidences (curve 1 in Fig.9) was determined for the separated-out part. The wings of the curve clearly revealed a periodic structure, due to the chance coincidences of particles from different micropulses. For analogous measurements with the wide peak (associated with magnetic extraction of the beam), no periodic structure occurred (curve 2 in Fig.9). The dip in the curves immediately after the principal peak of coincidences was due to the dead time of the input circuits of the coincidence system. The absence of microstructure in the "stretched" beam is the principal advantage of the stretching system employed.

The authors are happy to thank V. I. Danilov, E. I. Rosanov, and I. B. Enchevich for discussing the results and also N. R. Yushkevich for a great deal of work in inspecting the photographs.

LITERATURE CITED

1. V. A. Kazakov et al., Preprint No. 1943, OIYaI, Dubna [in Russian] (1965).
2. V. I. Danilov et al., Preprint No. R-1853, OIYaI, Dubna [in Russian] (1964).
3. V. I. Danilov et al., Atomnaya Énergiya, 19, 289 (1965).
4. A. F. Dunaitsev et al., Pribory i Tekhnika Éksperimenta, No.2, 114 (1964).
5. V. G. Zinov, S. V. Medved', and E. B. Ozerov, Preprint No. R-2657, OIYaI, Dubna [in Russian] (1966).
6. Yu. M. Grashin et al., Atomnaya Énergiya, 18, 384 (1965).

THE BN-350 AND THE BOR FAST REACTORS*

A. I. Leipunskii, I. I. Afrikantov, V. V. Stekol'nikov, O. D. Kazachkovskii, V. V. Orlov, M. S. Pinkhasik, Yu. E. Bagdasarov, R. P. Baklushin, I. V. Milovidov, A. A. Rineiskii, I. A. Kuznetsov, Yu. A. Zakharko, Yu. N. Koshkin, V. I. Shiryaev, S. M. Blagovolin, I. D. Dmitriev, I. S. Golovlin, and B. A. Tachkov

UDC 621.039.526

The reloading system and the construction of the safety control mechanisms of the BN-350 reactor are described and problems of emergency cooling and transient processes are discussed. The experimental BOR assembly is also discussed, a description is given of the reactor and engineering equipment, and the basic technical characteristics are cited.

In the USSR, on the shores of the Caspian Sea and in the region of the Mangyshlak Peninsula, a nuclear power station with the BN-350 fast reactor is being constructed. The reactor will provide an electrical output of 150 MW and an output of 120,000 tons of fresh water per day. For the initial period of operation, parameters have been chosen which have already been established experimentally. The reactor can operate in various cycles without modification of the core, using both U^{235} and plutonium as the nuclear fuel.

The basic technological details and the special structural features of the BN-350 reactor were presented in reports at the Third International Conference on the Peaceful Uses of Atomic Energy (Geneva, 1964) and at the Detroit Conference in 1965. At the present time, experiments to substantiate the design of the most important subassemblies of the reactor are being completed and the manufacture of the system and equipment is under way. The results of the testing of the individual systems and operating cycles of the BN-250 reactor are described below.

REACTOR REFUELING SYSTEM

The refueling system includes two rotating plugs, the refueling mechanism, two elevators, a refueling box with transfer mechanism and two conveyor drums (one for fresh and one for spent fuel assemblies). The fuel assembly reloading mechanism is located in the small rotatable plug, which in its turn is located eccentrically in the large rotating plug. By rotating the two plugs the refueling mechanism can be guided over any socket of the core and of the elevator. The elevators are lifts, in the carriages of which are sockets in which the fuel assemblies are inserted. The fuel assemblies are transferred from the refueling mechanism to the transfer mechanism, and vice versa, by the movement of the carriage along an inclined guide.

At the point where the elevator meets the transfer mechanism, the head of the fuel assembly is located above the level of the sodium, so that the pickup device of the transfer mechanism does not come into contact with the sodium. The fuel assembly transfer mechanism is located in the refueling box. Movement of the mechanism along the box directs the pickup device to the elevator sockets and the conveyor drum sockets. The mechanism picks up a fuel assembly, lifts it into the box and transfers it to the spent fuel drum. After this, the fuel assembly is dropped into one of the drum sockets. On the reverse route, the transfer mechanism picks up a fresh assembly from the other drum and transfers it to the elevator which drops the fuel assembly into the lowest position. Here, the fuel assembly is picked up by the refueling mechanism and transferred to the socket intended for inserting the fresh fuel assembly.

*Report presented by the USSR at the Conference on Fast Reactors in England (May 1966). Abridged version.

Translated from Atomnaya Énergiya, Vol. 21, No. 6, pp. 450-462, December, 1966. Original article submitted July 18, 1966.

The fuel assembly reloading cycle is repeated until all spent fuel assemblies are unloaded and the required number of fresh fuel assemblies are loaded into the reactor. The reloading cycle (about 40 fuel assemblies) lasts about 3 days, including the time of preparation for refueling and for starting up the reactor after refueling.

The refueling equipment consists of the rotating plugs (large and small), which at the same time serve as part of the upper biological shield of the reactor, and the refueling mechanism. The reactor is sealed (in the gaps between the plugs) by means of liquid seals of a Sn-Bi eutechtic mixture (mp 138°C), which is melted by means of electrical heaters mounted in the alloy tank. During operation of the reactor, the alloy is in the solid state. A secondary mechanical seal is provided, consisting of a rubber compression ring which is compressed against the sealing surfaces by bolts. During refueling the rubber gasket is raised slightly, thus freeing the plugs for rotation. The upper parts of the plugs are cooled by air pumped through special channels.

The refueling mechanism consists of the pickup device, with rods, the guide tubes with thrust flanges, a lifting and rotating device and their driving mechanisms. All the slave units are mounted in the housing of the mechanism. The pickup device engages the head of the fuel assembly, removes it from the socket, holds it during transfer, and places it in the elevator sockets. The entire complex of the refueling-system mechanisms is directed and controlled from a control desk according to a program which determines the sequence of operation of the mechanisms.

The refueling mechanisms enable reloading of the fuel assemblies into the core, the breeder blanket, and the safety control rods to be effected. Special devices are provided to control the pickup and release operations.

The spent fuel assemblies are transported from the reactor to the transfer drum in an atmosphere of argon. If the need arises, the fuel assemblies can be cooled during transfer by circulating argon by means of special blowers installed on the fuel assembly transfer mechanism.

All units of the refueling equipment have passed the appropriate tests. The leak-tightness of the liquid seals was tested with liquid and solid Sn-Bi alloy, for which a special rig was designed, simulating the sealing design of the rotating plugs.

As a result of the tests, the material for the parts of the liquid seal unit, directly in contact with the Sn-Bi alloy (Steel 20), was chosen, and the type of cladding was determined with the object of ensuring reliable wetting. In order to protect the Sn-Bi alloy from oxidation, a silicone vacuum grease is used; this grease meets the requirements of stability and compatability with the Sn-Bi alloy and with the structural materials of the liquid seal.

The purpose of testing the refueling mechanism was to determine the lifetime of operation of the mechanism under operating conditions. To simulate the core of the reactor on the rig, a group of fuel assemblies (7) was used; these were loaded by means of the mechanism. The fuel assembly was engaged by the mechanism, raised to a height of about 3600 mm, returned and reinserted into the socket and the mechanism was disengaged from the fuel assembly. The entire mechanism was operated for more than 6000 h.

Testing was carried out by positioning the fuel assembly and the pickup mechanism first coaxially, and then at a misalignment of up to 20 mm. In all cases, engagement of the pickup with the fuel assembly was reliable. The most suitable material for the pickup and friction pairs operating in the sodium was found to be stainless diffusion-chrome steel, type Kh18N9.

The elevator is a lifting mechanism, the carriage of which moves along a special track fixed at an angle of 17° relative to the vertical. In the carriage is a braced sleeve in which are inserted the fuel assemblies which are being reloaded. The carriage may be operated either by motor or manually. The carriage drive mechanism consists of a motor, reduction gear, chain transmission, and a rod. The fuel assembly transfer mechanism consists of the rack with pickup, reduction gear for the rack lift, the reduction gear frame, and a girder with the guides. The rack is made in the form of a tube with teeth cut along the generatrix. The frame with the reduction gear and the rack is moved horizontally along the box via the guides. The rack and chain of the pickup are driven by feed shafts and the fuel assembly transfer mechanism is moved by means of a guide screw.

In 1966, tests will be carried out on a standard model of the elevator, for which a sodium rig has

been constructed with the sodium circulating at a temperature of 500°C. During 1966-1967, a trial assembly of the reactor from standard units and subassemblies will be carried out on a special factory-produced rig.

THE SAFETY CONTROL ROD SYSTEM

The safety control system consists of the following mechanisms: a) measurement and control of the power and period of the reactor (including the subcritical cycle); b) automatic control; c) compensation for change of reactivity; d) reactor scram system. The basic technical data and a description of the design of the safety control mechanisms follow.

Slave Mechanism for Automatic Control

Number of mechanisms	2 pieces
Number of rods in each mechanism	1
Radius of distribution (from the center of the core)	98 mm
Efficiency of one rod	0.20%
Rod travel	750 mm
Maximum speed of movement	150 mm/sec

Compensator Slave Mechanism

Number of independent mechanisms	7 pieces
Number of fuel assemblies per slave mechanism	1
Total efficiency	2.1%
Weight of uranium in fuel assembly	18 kg
Fuel assembly travel	1060 mm
Speed of movement	10 mm/sec
Pitch of movement	20 mm

Slave Mechanism of the Scram System

Number of independent mechanisms	3 pieces
Total efficiency	3.5%
Rod travel	1260 mm
Time of operation	0.7 sec
Speed of movement, raising	5 mm/sec

The functional units of the safety control slave mechanisms are the absorber rods and the compensating assemblies. Each slave mechanism complex consists of a pedestal with rod, rack mechanism, servo-drives, absorber rod, and a compensating assembly. The pedestal with rod is a mounting unit riveted to the flange of the central reactor pedestal. The rack mechanism is riveted to the corresponding pedestal with studs. The servo-drive units of the slave mechanisms are fixed to a special plate and are connected to the appropriate rack mechanism by means of a leaktight drive. Rotation from the hermetically sealed electric motor is converted via the rack mechanism into translational movement of a rod, at the lower end of which is a nose piece with clamps, by means of which the absorber rod is engaged. Control by the clamps is carried out manually (by means of handles in the upper part of the mechanism). A control is provided here for engaging and disengaging the rod with the shank which is accomplished by means of a coupling rod, passing inside the rod.

The absorber rod mechanism of the automatic control comprises seven elements—each with a diameter of 9.6 mm — containing boron carbide enriched to 80% in B^{10}. There is a gas cavity in the upper part of the rod for collecting the helium formed as a result of burnup of the boron.

Change of reactivity is compensated by axial movement in the core of six assemblies with active material (burnup compensators) and one assembly with a boron absorber (temperature compensator). The burnup compensator contains an active section, consisting of fuel elements which are similar in design to the core elements. The temperature compensator is constructed from elements containing boron carbide.

The control rod mechanisms have been tested on the sodium rig at a circulating sodium temperature of 500°C and an oxide content of 5×10^{-3}%. The total time of stay of the mechanisms in the sodium was more than 8000 h. During this period, the automatic control mechanism had undergone 20,000 double operations, the scram mechanism 1600 tripouts and 400 double operations in the slow scram cycle, and the compensator mechanism — 2500 double operations.

During the entire period of the "endurance" tests, all mechanisms functioned efficiently and there was no case of withdrawal from the system or breakdown in operation.

EMERGENCY COOLING AND TRANSIENT CONDITIONS

A great deal of attention has been paid to the problems of residual heat removal from the reactor after operation of the scram system. The suitability of a particular cooling system was assessed from the point of view of preventing superheating of the fuel elements and preventing the development of dangerous nonsteady-state thermal stresses in the structural elements of the reactor. The procedure proposed allows us to calculate the temperature distribution in the reactor, in the intermediate heat exchanger, the steam generator, and in the liquid-metal circuits of the triple-circuit multi-loop nuclear installations. The relationship between power loss and time, due to delayed neutrons and β- and γ-decays of the fission fragments is determined from the physical calculation of the reactor. The nonsteady state coolant supply is calculated by taking into account the flow inertia, the "coasting" of the pump, and the natural circulation driving pressure.

There are no special cooling systems in the installation and the removal of residual heat in any emergency situation is accomplished by the primary cooling system.

The rapid operation of the scram system is permissible only in exceptional cases. The greater part of the signals is fed to the slow scram system, which reduces the power by a factor of 2.7 after 100 sec. This rate enables the cooling of the reactor to be continued with a nominal coolant supply without exceeding the permissible thermal stresses in the structural elements.

The total cessation of the electrical supply to the primary circulating pumps is the most dangerous situation, and therefore a great deal of attention was paid to ensuring natural circulation. This investigation allowed us to determine the direction of motion of the coolant in the reactor, and the location of the heat exchanger plant with respect to the height of the reactor; it also influenced the design of the intermediate heat exchanger and the nonreturn valve. In the absence of reverse flow, the straight-through section of the latter is never completely shut off. The driving pressure of the natural circulation creates a coolant flow through the reactor of the order of 5 to 6% of the nominal. This is insufficient for cooling the reactor in the initial period. Calculations show that if the residual heat is removed solely by means of the flow inertia and the natural circulation in the individual channels, the temperature of the sodium can rise to 800-900°C. Therefore, all available methods for establishing a force supply of coolant during the initial period (30-60 sec) after rapid shutdown of the reactor were examined. For example, the possibility of using the kinetic energy of the rotating masses of the turbogenerators for extending the operating time of the pumps was investigated.

By simultaneous coasting of the pumps with the turbogenerators, the supply of sodium through the reactor changes very slowly (approximately exponentially with a time constant of 50 sec). Despite the large volume of sodium above the core, the temperature of the coolant leaving the reactor tank changes sharply by this method; this gives rise to considerable thermal stresses. Figure 1 shows the time-variation of the nonsteady-state thermal stresses and coolant temperature at control points of the primary circuit. This operating cycle is undesirable and, therefore, the use of turbogenerators for emergency operation of the pumps was rejected.

Simultaneous solution of the equations for the dynamics of the flow and of the rotating parts of the pump unit showed that when the main electric supply is disconnected the sodium feed through the reactor changes exponentially with a time constant of 7 sec, during 15-20 sec. The results of calculations of the temperature cycle of the reactor in the case of residual heat removal by coasting of the pumps, with subsequent transition to natural circulation, is shown in Fig. 2. The thermal stresses in this case are insignificant and are not shown in the figure.

The large reserve of water in the steam generators and the considerable thermal capacity of the sodium circuits require that the electrical power supplies for the water pumps be switched on within a few tens of minutes after the emergency.

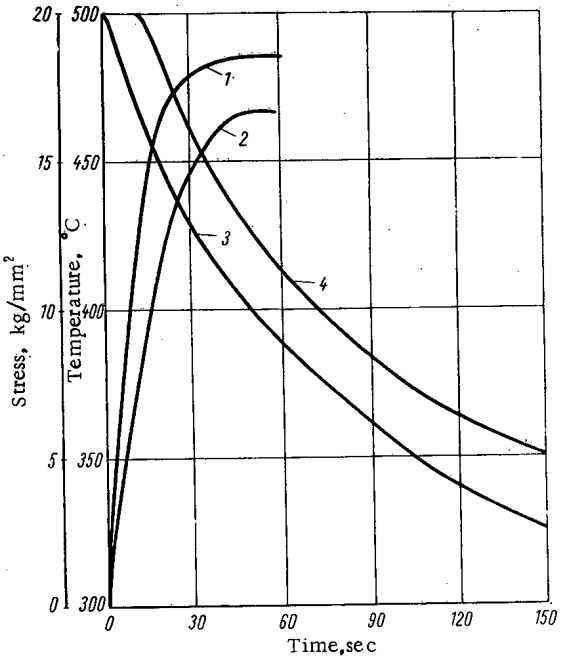

Fig. 1. Coolant temperature and thermal stresses as a result of cooling by utilizing the coasting energy of the turbogenerators. 1) Thermal stresses at the inlet nozzle of the primary circuit heat exchanger; 2) thermal stresses in the conduit at the outlet from the reactor; 3) sodium temperature at the outlet of the reactor; 4) sodium temperature at the inlet to the heat exchanger.

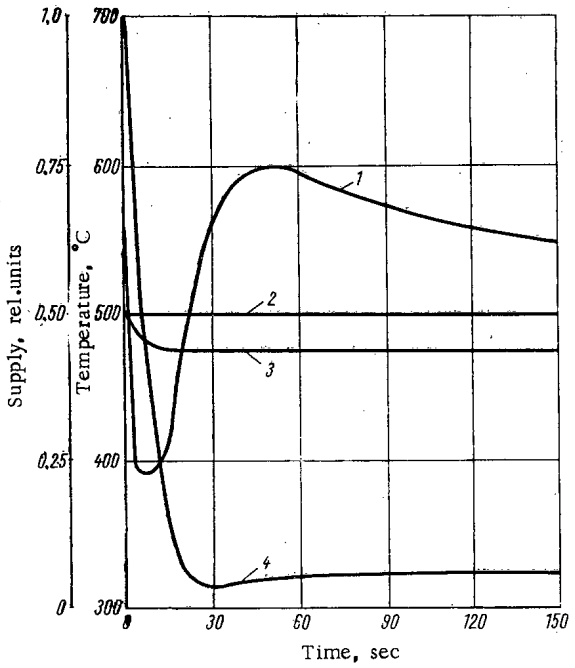

Fig. 2. Change of primary reactor parameters as a result of cooling by means of coasting of the pumps and natural circulation. 1) Sodium temperature at the exit from the most stressed fuel assembly of the core; 2) sodium temperature at the heat exchanger inlet (through the primary circuit); 3) sodium temperature at the outlet from the reactor; 4) sodium feed through the reactor.

In addition to the emergency conditions for the BN-350 reactor, conditions were studied in which a relatively small change of coolant flow takes place in the primary circuit. In practice, the principal instance of such a variation is after one sodium pump of the primary circuit is disconnected. The essential problem of this investigation is to determine the necessity for shutdown of the reactor.

If, after shutting down one pump, the reactor is to remain at the previous level, the temperature variation of all the reactor units will be stabilized after a certain time, having attained values which are determined by the resulting reduced supply of coolant through the reactor. This cycle of operation is not permissible. Therefore, after shutting down the pump it may be necessary to transfer the reactor earlier to a reduced power level which will ensure a nominal level with the new supply of coolant. This transition can be accomplished in different ways. Blocking can be introduced, by means of which the power controller will move to a new position on receipt of a signal indicating the cut-out of one pump. It is possible to carry out this operation also by means of the temperature regulator of the sodium at the outlet from the reactor, which maintains a specified temperature, acting on the power controller. The temperature probes of the regulator are located in the reactor tank in the region of the outlet nozzles. Thus, after cutting out one pump, the increase of temperature of the sodium in the reactor tanks sets the regulator in action and it transfers the power-controller to a position such that the sodium temperature is maintained at the former level.

The dependence of the supply of sodium through the reactor on the time was found, in the case of coasting of one pump switched in parallel with the others. It was assumed that the hydraulic resistance of all parts of the reactor and conduits is proportional to the square of the coolant flow through it; the pump delivery varies directly with the angular velocity of the driving wheel, and the pressure is proportional to the square of the angular velocity. The dependence of the kinetic energy of the coolant,

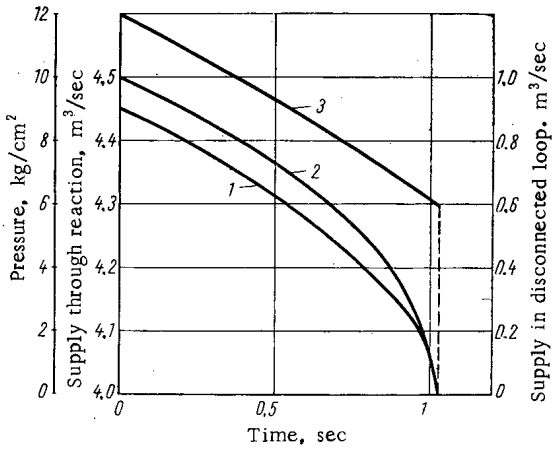

Fig. 3.

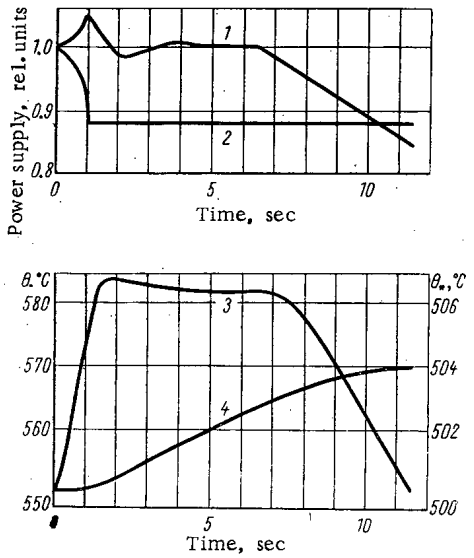

Fig. 4.

Fig. 3. Coasting of one pump of the primary circuit: 1) sodium supply in the disconnected loop; 2) sodium supply through the reactor; 3) pressure of coasting pump.

Fig. 4. Transient process in the core with one pump of the primary circuit shut down: 1) power $\bar{n} = n/n_0$; 2) coolant supply through the reactor, $\bar{G} = G/G_0$; 3) sodium temperature at the outlet from the core, θ; 4) probe temperatures in the reactor tank, θ_*.

the pump rotor, and the electric motor on the angular velocity were taken into account. The results of the calculation of the coasting of the pump are shown in Fig. 3. Because of the nonuniformity of the pressure in the gaps due to the nonuniform distribution of the coolant supply throughout the radius of the core, the radial flow of the sodium over the heads of the fuel assemblies, and other factors, the fuel assemblies are displaced relative to their initial position. Since the upper ends of the fuel assemblies are free, considerable movement can be expected when the sodium feed through the reactor is varied. Particularly dangerous situations arise when reduction of the gaps leads to movement of the fuel towards the center of the core.

In order to determine the displacement of the fuel assemblies, the sodium pressure field in the gaps between the fuel assemblies was plotted. The magnitude of these displacements under the action of the forces applied to a fuel assembly in a radial direction is determined by the elastic buckling of the fuel assembly and by rotation in the "seal." If rotation in the seal is not taken into account, a value of $\Delta k/k = -3 \cdot 10^{-4}$ is obtained for the hydrodynamic effects of the reactivity, corresponding to an increase of the sodium supply from zero to nominal. The problem concerning the leak-tightness of the fuel assembly seal has been studied insufficiently up to now; and an accurate study of this factor has not been possible at present. Therefore, in the subseqent calculation, a rougher approximation was used. It was assumed that in varying the sodium supply through the reactor from zero to a nominal value, the fuel assemblies swivel freely in the seal from the vertical position outwards to the most extreme position — as far as the gaps in the seal and between the fuel assemblies permit. By a corresponding reduction of the supply, the fuel assemblies are displaced towards the center by the same amount. The hydrodynamic effects of the reactivity, which correspond to this model of the sodium supply reduction from nominal to zero, give a value of $\Delta k/k = -32 \cdot 10^{-4}$. Buckling of the fuel assemblies was not taken into account in this case, because it is considerably less than the assumed displacements. It could be concluded from a more accurate calculation that all pressure variations in the gaps between the fuel elements and, consequently, their displacements, are proportional approximately to the square of the sodium supply. Therefore, in future for determining the hydrodynamic effects of reactivity corresponding to a variation of coolant supply from the nominal value G_0 to the value G, the formula

$$\left(\frac{\Delta k}{k}\right)_G = -\left(\frac{\Delta k}{k}\right)_0 \left(1 - \frac{G^2}{G_0^2}\right)$$

has been used. In the BN-350 reactor, by cutting out one of the five pumps in the primary circuit, the coolant supply is reduced by approximately 12%. This means that the injection of a reactivity of $7.2 \cdot 10^{-4}$ can be expected.

On the basis of the data obtained about the variation of the sodium supply and the hydrodynamic effects of reactivity, the temperature cycles of the reactor were investigated. Calculations were carried out by a semianalytical method. Factors were taken into account which were associated with the thermal lag of the reactor, the mixing chamber and the temperature probes. The results of the calculation, shown in Fig. 4, showed that the temperature regulator is completely capable of coping with transition of the plant to reduced power.

In the case when one pump of the primary circuit is shut down, the temperature field of the heat exchanger was also studied. If no special measures are taken, the temperature of the sodium at the outlet from the heat exchanger of the secondary circuit decreases rapidly after shutting down one pump of the primary circuit; this leads to the origination of large thermal stresses in the structural units. The magnitude of these stresses is estimated in the calculation. In order to reduce them, it was found necessary to shut down the corresponding pump of the secondary circuit, following shutdown of the pump in the primary circuit.

IMPROVEMENT OF THE OPERATING CONDITIONS OF THE FUEL ELEMENTS

The reactor installation will be modernized in accordance with the extent of the accumulated operating experience, and its efficiency characteristics will be improved.

Possibilities are being considered at present for improving the operating conditions of the BN-350 reactor fuel elements and also for further increasing the fuel burnup. For this purpose, the possibility of increasing the gas void in the fuel element is being studied, in the case of variation of the dimensions of the fuel assemblies because of the corresponding reduction in thickness of the end shield. In this case, the upper end reflector is combined with the core in a common cladding. Calculations showed that the reduction in thickness of the upper reflector to 200 mm by some reduction of the distance between the edge of the core and the edge of the end shield does not cause any significant improvement of the physical characteristics of the reactor.

The use of fuel elements with an increased gas cavity enables the fuel burnup to be increased, and at the same time, the maximum stresses of the axis of compression of the gases to be reduced, both by a factor of approximately two.

The union of the core with the upper end reflector leads to extension of the closely packed bundle of core cans and, consequently, to an increase of the pressure differential per fuel assembly. In order to reduce the pressure stresses, it is proposed to increase the radius of curvature of the corners of the hexagonal tubes and thereby to reduce the maximum stresses from the pressure at the wall of the fuel assembly by a factor of 1.2. The increase of the radius of curvature of the corners of the hexagonal tubes is accomplished by removing 6 (out of 169) corner fuel elements of the fuel assembly (cluster). The physical characteristics of the core and also its dimensions were changed insignificantly, as a result of this.

THE BOR EXPERIMENTAL FAST REACTOR

The BOR reactor — an experimental fast neutron reactor with a maximum power of 60 MW — is being installed on the site of the Nuclear Reactor Scientific Research Institute at Melekess. Design and research work were begun at the end of 1963. At present, the technological design has been completed and the working drawings for the primary equipment are being prepared. Construction of the building was started in May 1965, and start-up of the reactor is planned for 1968.

The BOR reactor is designed for fundamental and experimental verification of the basic parameters and units of high-temperature, high-performance sodium-cooled fast reactors for future nuclear power stations with an electrical capacity of 1000 MW and above. The parameters of the first nuclear power station with the BN-350 fast reactor have been selected with a certain amount of caution, to guarantee safe operation of the station, and the selection has been confirmed by experiments and operating experience with the BR-5 reactor. However, even now there are a number of obvious measures which must be taken for improving the physical and technical-economical characteristics of nuclear power stations

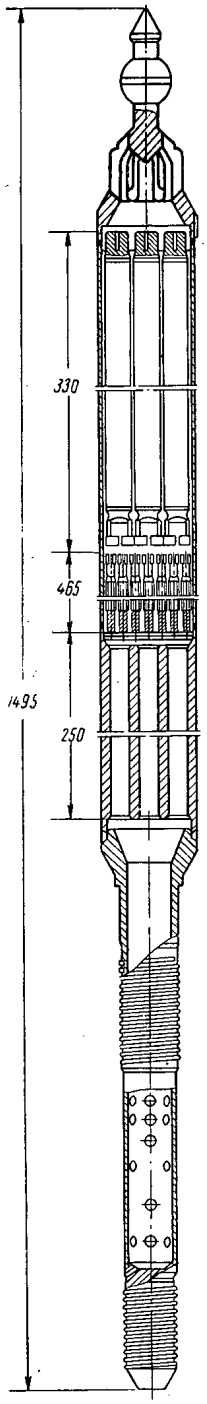

Fig. 5. Fuel element cluster with vented fuel elements. (dimensions in mm)

with fast neutron reactors. In the first place, it is necessary to increase: a) the burnup, b) the power density, c) the temperature of the coolant at the outlet from the reactor and, because of this, the efficiency of the steam turbine cycle, and d) the unit power of the station.

The most important measure is the creation and experimental production of fuel elements for the cores of high-performance reactors, which are essential for operating at high thermal flux densities and high temperatures. In order to solve this problem, the BOR reactor is being constructed first. Fuel elements of different composition and design will be used in it, including vented fuel elements.

THE CORE AND SHIELDS

The Core of the BOR reactor consists of hexagonal fuel assemblies with a gage of 44 mm below the "key" and a lattice pitch of 45 mm. The number of fuel assemblies varies, depending on the operating cycle, burnup and type of fuel. 70-80 fuel assemblies are necessary for the version with undepleted fuel of 90% enriched UO_2, which corresponds to a U^{235} loading of 150-160 kg. In the functional section of the assembly, 37 fuel elements with a diameter of 6.1 mm are arranged in a triangular lattice with a pitch of 6.7 mm. Enriched uranium or plutonium oxide, carbide, and other compositions can be used as the fissile material. The fissile material length of the fuel element is 400 mm. Tubes of stainless steel with a wall thickness of 0.4 mm for the hermetically sealed fuel elements and 0.25 mm for the vented elements is used for the cladding. In the sealed elements, cavities are provided for the collection of gaseous fission products; in the vented elements, special arrangements are provided for discharging the gaseous fission products into the coolant. One design of a fuel element cluster with vented fuel elements is shown in Fig. 5.

The fuel elements are braced by the lower stems to grids welded to the hexagonal tube. The upper ends are free and can be moved around the axis. The fuel elements are spaced by means of wire wound spirally on the cladding.

Above and below the active section of the fuel assembly are located the end shields. Their structural design depends on the design of the fuel elements in the active section of the cluster. The elements are sealed in a hexagonal cladding with a thickness of 1 mm. The assembly has an upper end plate with a cap which is gripped by the refueling machine, and a lower end plate designed for locating the fuel assembly in the baffle sleeve of the pressurized collector. The lower end plate has lateral openings for admitting the sodium; this prevents the fuel assembly from splitting under the action of the coolant flow. The upper ends of the fuel assemblies are not fixed and consequently they are capable of free thermal expansion along the axis of alignment; movement in a radial direction is possible only within the limits of the engineering tolerances.

Throttling of the sodium supply along the fuel assemblies according to the heat release in them is accomplished by means of slots in the baffle sleeves of the pressurized collector, covering a specified number of lateral holes in the stems of the fuel assemblies.

The Lateral Shield is assembled from fuel element clusters whose external diameter is similar to the core clusters. Each contains seven elements with a diameter of 14.5 mm and with a cladding thickness of 0.35 mm, arranged with a pitch of 15.2 mm in a triangular lattice. The elements contain pellets of enriched uranium dioxide, with a fissile material length of 900 mm. The average thickness of the shield is 150 mm. The clusters are located by the lower stems in the baffle sleeves of the pressurized collector and the upper ends are not fixed. The sodium enters the cluster from the low pressure collector through a throttling disc at the end of the lower stem. Throttling of the coolant supply through the clusters of the lateral shield is accomplished by varying the diameter of this disc. The total number of clusters in the core and in the shield is 259.

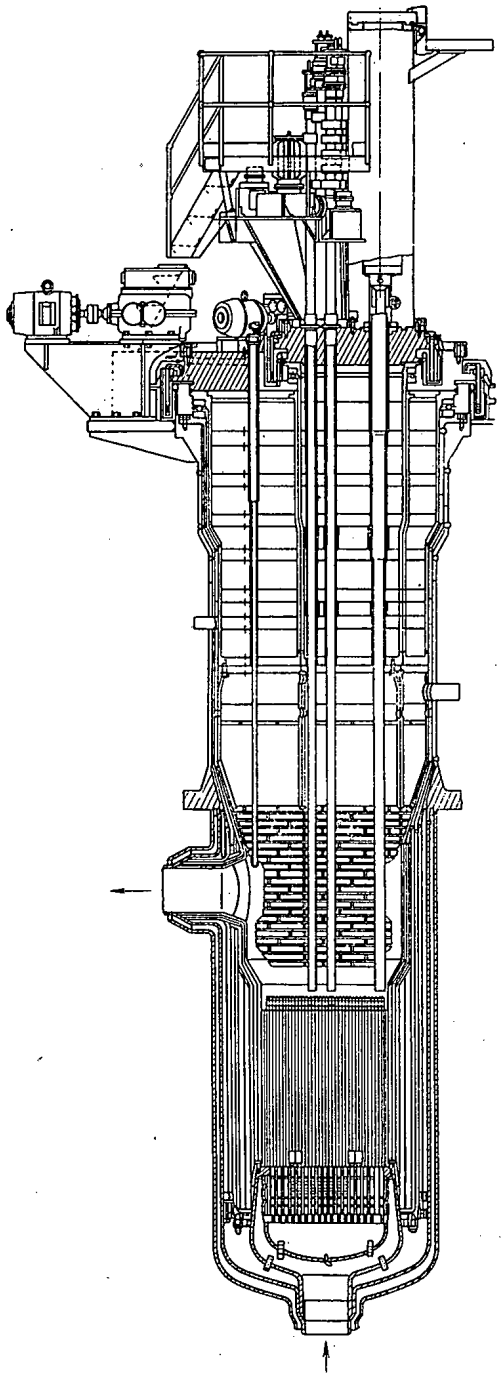

Fig. 6. Section through the BOR reactor.

The Reactor Vessel and the Intravessel Facilities (Fig. 6). The reactor vessel is cylindrical. The diameter at the core level is 1100 mm, and the maximum is 1500 mm. The height of the vessel is 6500 mm and the wall thickness is 16-20 mm. The middle and lower sections are enclosed in a leak-tight jacket, which prevents the reactor from emptying in the event of a leak. The jacket is also used for heating up the reactor with gas.

There is one inlet nozzle 300 mm in diameter, welded into the elliptical bottom and two outlet nozzles with the same diameter, located somewhat above the level of the cluster heads. At the top, the reactor is closed by two eccentrically positioned rotating plugs for aligning the refueling devices to a given cell of the core or shield. The plugs are constructed of alternate layers of steel and borated graphite and they provide the necessary biological shielding; in order to exclude leakage of gas, the plugs are sealed by means of freeze-seals of bismuth-tin alloy; this alloy is maintained in the frozen state (solid state) during operation of the reactor.

All the drive units of the safety control rods are mounted on the small rotating plug and also the transfer box for joining the reactor with the refueling machine.

Inside the reactor vessel are located the pressurized collector with the core and shields, the "basket," and the thermal shield. The pressurized collector is divided into a high-pressure zone for core clusters and a low-pressure zone for the shield elements.

The collector is suspended by the basket, which is a stepped cylinder and fastened to the upper section of the vessel. The basket with the collector can be replaced if necessary. A small portion of the primary sodium flow passes between the basket and the vessel for cooling the latter.

The steel ring reflectors of the thermal and neutron shields, with a total thickness of 240 mm, are located in the lower and central section of the basket. Their function is to reduce the incident neutron flux at the reactor vessel.

THE CONTROL AND SAFETY SYSTEM

The reactor control and safety system consists of three independent emergency (scram) systems, two compensators, one of which is a temperature compensator, and two automatic power regulators. The scram rods and the compensator rods are located in the core and the regulator (control) rods in the lateral shield. The functional units of all systems are identical in design and consist of a cluster of boron-containing rods. Each rod is clad in stainless steel filled with boron carbide (enriched in B^{10}). The efficiency of the control and safety system units and the magnitudes of the reactivity effects are given in the table:

Maximum thermal power	60 MW
Sodium temperature at the inlet	360-450°C
Average temperature at the outlet	600°C
Supply through reactor	750-1000 tons/h.
Core diameter (center section)	41 cm

Core height	40 cm
Average specific power	900 kW/l
Maximum thermal flux	2.65×10^6 kcal/m^2·h
Maximum sodium speed	10 m/sec
Maximum can temperature, taking into account possible overheating	800°C
Efficiency of three scram rods	3.3%
Efficiency of the temperature compensator	1.0%
Efficiency of burnup compensator	1.7%
Efficiency of two control rods	0.48%
Reactivity temperature coefficient	-4×10^{-5}, (°C)$^{-1}$
Reactivity power coefficient	-1.5×10^{-4}, (MW)$^{-1}$

The operating units are connected via a rod with clamps to the servodrives on the rotating plug. The drive mechanisms are disconnected by rotating the plug.

REFUELING SYSTEM

Fresh fuel clusters are loaded into the reactor and the spent clusters are withdrawn through a special channel in the small rotating plug. By rotating the large and the small plug, the channel is aligned on the selected socket of the core or the shield. The refueling machine is then driven up to it; this is a container with pickup devices, which is mounted on a gantry crane and can be moved along coordinate axes. The machine is connected and sealed to the channel in the small plug; the cluster selected for reloading is lifted by means of the pickup into the shielded container in an inert atmosphere, in which it is transferred to an external storage vault. In order to remove residual heat in the refueling machine, the design provides for a closed gas circuit with the corresponding equipment. This refueling machine also transports and inserts the fresh fuel clusters in the reactor; the fuel clusters are previously heated to approximately 300°C in an electric furnace.

TECHNOLOGICAL LAYOUT AND EQUIPMENT

The triple circuit layout: sodium - sodium - water - steam has been adapted for the BOR reactor. Heat is removed by two loops, each of which has been designed for 50% of the maximum power.

The primary circuit loop includes a centrifugal immersed pump, intermediate heat exchanger, nonreturn valve, and nonreturn armature.

In each loop of the secondary circuit, in addition to the heat exchanger and pump, a steam generator is installed. In addition, there is an air-cooled heat exchanger, designed on a thermal capacity of 30 MW, which can be connected with any loop of the secondary circuit instead of the corresponding steam generator. The supply of air through the heat exchanger is generated by fans (blowers). The steam, produced in the steam generators at a temperature of 540°C and a pressure of 100 atm, is used in a standard turbogenerator for generating electric power.

The layout of all three circuits is designed so that the required supplies of coolant are provided by natural circulation, thus ensuring reliable long-term heat removal from the reactor.

The Intermediate Heat Exchanger (Fig. 7) is a vertical cylindrical container in which there is a tubular cluster with a "floating" head. The sodium of the primary circuit flows into the intertube space from above downwards, and sodium from the secondary circuit flows through the tubes from below upwards. The heat exchanger is mounted on the upper cover of the primary circuit boxes and is structurally designed so that the tubular cluster together with the cover and the built-in upper shield can be removed without recourse to the conduits of the primary circuit and without entering compartments with high levels of radiation.

The Steam Generators installed in the various loops of the BOR reactor will have a different design. In one loop there will be a steam generator with natural circulation, and in another loop - a direct flow type. This is done so that different design versions can be developed under operating conditions that are as close as possible to those of future power generation systems. A special feature of both types of steam generators is the absence of free sodium levels in their housings, and the holding of these levels in special buffer tanks, installed at the sodium outlet. The feasibility of this solution is being verified experimentally at present.

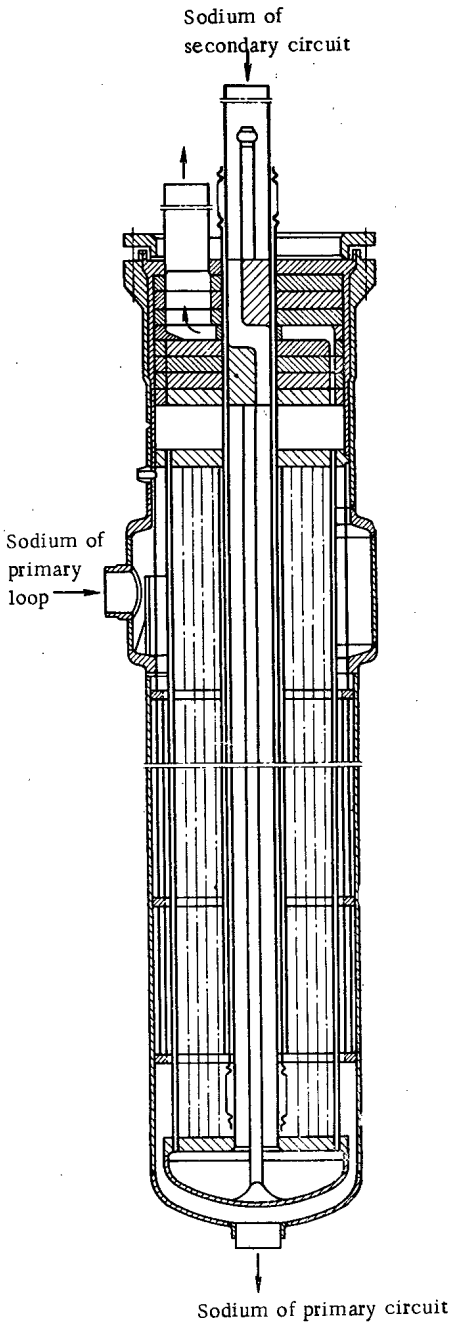

Fig. 7. Intermediate heat exchanger.

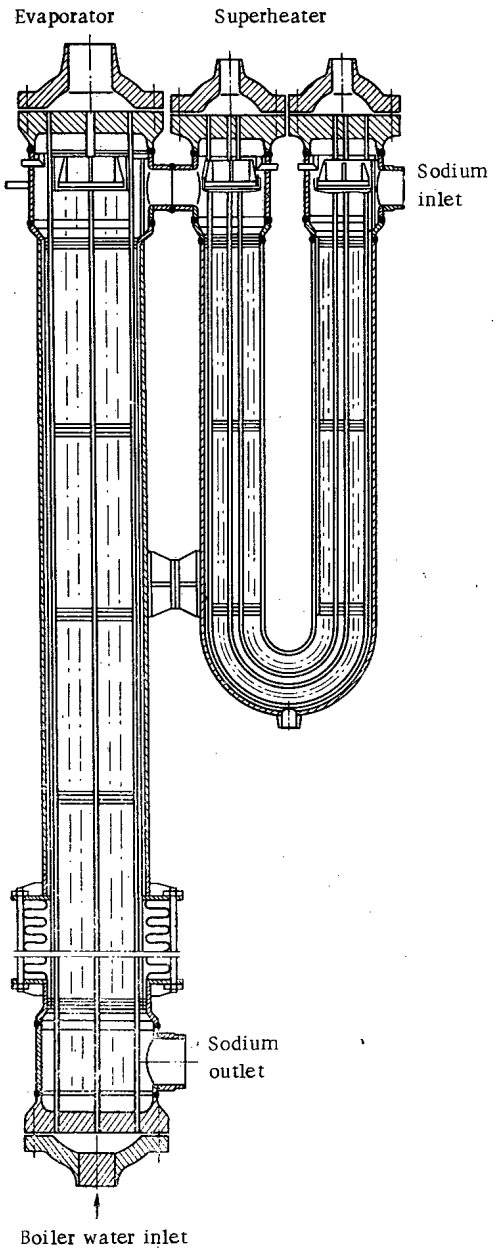

Fig. 8. Steam generator with natural circulation.

The steam generators with natural circulation (Fig. 8) has a straight-tube evaporator and a U-shaped superheater. Water and steam flow in the tubes and sodium flows in the intertube space. Water from the drum is fed to the lower distribution chamber of the evaporator and the steam-water mixture from the upper chamber is discharged into the drum. The sodium in the evaporator flows from top to bottom. In order to compensate for the different temperature expansions of the tubes and housing, lenticular compensators are installed in the latter. To prevent moisture from entering the steam superheater, appropriate separating units are provided inside the drum. The evaporator and the superheater are made from perlitic steel.

The Direct-Flow (Once-Through) Steam Generator (Fig. 9) consists of two cylindrical vessels with a diameter of ~1 m. The tubular cluster of the evaporator contains 60 coils and the superheater

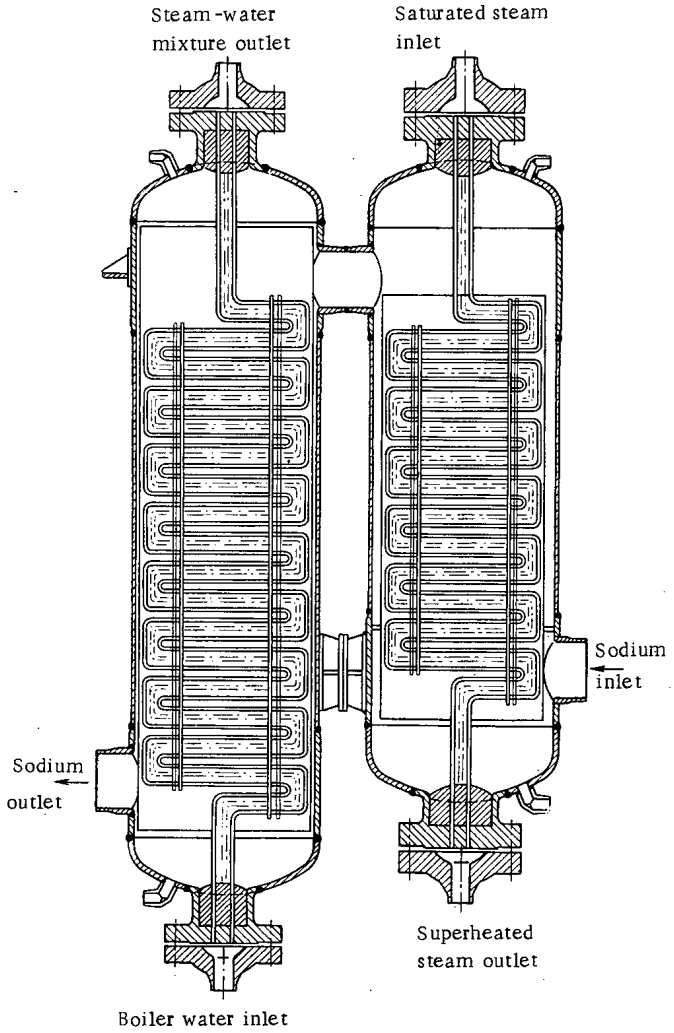

Fig. 9. Direct-flow (once-through) steam generator.

90 coils of 16 mm diameter tubing with a wall thickness of 2.5 mm. The tube plates in each vessel are positioned one at the top and the other at the bottom. The sodium flows in the steam generator from bottom to top, and in the evaporator - from top to bottom. This flow system of the sodium and water in the evaporator makes it possible to arrange natural circulation under certain emergency conditions. For this purpose, a special small condenser is provided, which is cooled by water from a nondetachable power supply source. The steam generator is made of perlitic steel.

The Circulating Pumps of the primary and secondary circuits are similar in design. Each pump has two bearings – a lower radial hydrostatic bearing, operating in the sodium and an upper – a static thrust oil bearing and also a gas-tight oil-sealed shaft. The metal enters the intake directly from the pump tank and the necessary supply through the intake lines is established because of the difference between the levels in the pump tank and the reactor. The pump speed is controlled by dc motors. The pump is fitted on the upper cover of the primary circuit boxes so that the motor is accessible for servicing during operation.

EXPERIMENTAL FACILITIES

Great opportunities are provided in the BOR reactor for carrying out experimental and research work on neutron physics, the behavior of fuel at high burnups, radiation stability of materials, the study of the discharge of fission products into the sodium coolant and the gas system of the reactor, and their distribution throughout the circuit. The latter are of special interest, since vented fuel elements will be tested and developed in the reactor. For studying the entire complex of problems, by-pass sections will be mounted on the installation and fitted with spectrometer recorders for monitoring the level of contamination of the coolant and of the surface of the coolant circuit during operation of the reactor; gas lines will be installed for spectrometric analysis of fission products in the gas cavities of the reactor and the pumps; delayed neutron detectors will be installed in the outlet conduit. For continuous monitoring by the level of gaseous activity, including specified short-lived products, provision is made for circulating the gas through the gas lines. A special channel located near the center of the core is of great interest; this is for studying the operating conditions of fuel elements, representing a fuel element cluster, identical with the others in external appearance but equipped with the appropriate probes. During discharging the fuel cluster is withdrawn from the core and is rotated together with the plugs.

In addition, provided for physical investigation are four horizontal beams and 10 vertical uncooled channels, including a channel with a diameter of 300 mm. A large number of fuel assemblies can be loaded into the core and the shield with the specimens (up to 30 fuel assemblies in the core).

EFFECT OF THE SURFACE MATERIAL OF THE CIRCUIT ON THE ACTIVITY OF CORROSION DEPOSITS

A. P. Veselkin and O. Ya. Shakh

UDC 621.039.538.7:621.039.58

Some questions of radiation safety associated with the corrosion and activation of construction materials are considered. It is shown that the effect of the surface material of the primary circuit on the formation of active surface deposits must be taken into account. The validity of the mathematical model used to describe the processes of washout, transfer, and deposition and that of some of the assumptions made are considered.

On comparing the computed results with experimental data, reasonably good agreement is obtained.

In order to improve the radiation situation when carrying out repair work, it is recommended that steels not containing elements giving long-lived isotopes should be used. Such steels include, for example, the chromium-manganese type, the induced activity of which has a fairly short half life (manganese) and a low γ-quantum yield per disintegration (chromium).

The rate of over-all corrosion (0.001 to 0.002 mm/year) typical of construction materials used in modern reactor building is completely safe from the point of view of the strength of structure. Even with such a low rate, however, several hundred grams of corrosion products per day may be formed in the primary circuit of modern water-cooled water-moderated reactors.

On the background of the intense radiation flux in a working reactor, the effect of the γ-radiation of activated corrosion products on the biological-shielding dose rate is usually insignificant.

However, since the neutron fluxes activating the reactor components reach 10^{13} neutrons/cm^2·sec, the contamination of the circuit surfaces with activated corrosion products and their effect on the level of activity after shutting the system down at present constitute the most serious of all problems associated with corrosion.

In determining the radiation activity, it is extremely important to remember even the most negligible (at first glance) impurities, especially those forming nuclei with long half-lives.

One of the most important of such elements is Co^{59}, which is usually present in steels as an element accompanying nickel in proportions up to 0.9% of the latter [1].

The effects of the parameters of the reactor system on the formation and transfer of active corrosion products vary and are not too well known. We can only say that the greatest influence on the processes of deposition, washout, and the transfer of activity is exerted by such parameters as the pH value, the oxygen and impurity content, and the hydrodynamics of the flow washing the surface of the circuit.

In an earlier paper [2], we made a number of simplifying assumptions and obtained a solution for a system of equations describing the development and build-up of the activity in the primary circuit associated with corrosion products. In order to describe these processes, we used a washout constant k_w and a deposition constant k_d.

The effect of the primary-circuit surface material on the activity of the corrosion deposits was studied by means of the mathematical model proposed in [2].

Translated from Atomnaya Énergiya, Vol.21, No.6, pp.462-465, December, 1966. Original article submitted March 9, 1966.

RESULTS OF CALCULATIONS

The mean change in weight of the corrosion deposits per unit surface of circuit, after a fairly long operating time T_o, may be put in the form (see [2])

$$\overline{N}_o = \frac{C_c}{k_d + k_w}\left(1 + \frac{k_d T_o}{2}\right) \quad (1)$$

for constant decontamination (scavenging) of the circuit $\lambda_\Phi = 0$ (sec^{-1}), and

$$\overline{N}_o = \frac{C_c(\lambda_\Phi + k_d)}{\lambda_\Phi k_w} \quad (2)$$

for $\lambda_\Phi \neq 0$*. The corrosion rate C_c (in $mg/m^2 \cdot sec$) is taken as

$$C_c = \frac{1}{T_c}\int_0^{T_o} C_c(t)\,dt.$$

If deposition may be neglected ($k_d' = 0$), we obtain from (1) and (2)

$$C_c = k_w \overline{N}_o. \quad (3)$$

We see from expression (3) that the washout constant k_w equals the corrosion-film growth constant and can easily be determined in the course of corrosion tests. It should be noted that this is only valid on condition that $k_d = 0$, which is reasonably true, for example, in autoclave corrosion tests on small samples.

The coarsest assumption in [2], namely, the condition $C_c = const$, was made in order to simplify the mathematical model. The effect of this assumption on the agreement between computed and experimental data was checked for the circuit described in [3]. For this purpose the corrosion rate was represented by an analytical expression of form

$$C_c(t) = at^{-b}. \quad (4)$$

The system of equations in [2] was solved numerically on an electronic computer, using a program devised by N. A. Gur'eva and A. V. Nikitin. Calculations were made with $k_w = 5 \cdot 10^{-8}$ sec^{-1}, $k_d = 3.0 \cdot 10^{-5}$ sec^{-1}, and $\lambda_\Phi = 2.5 \cdot 10^{-5}$ sec^{-1} [3].

Figure 1 shows the computed change in the quantity of corrosion products in the water of the circuit as a function of operating time. The experimental values were taken from [3]. The value of the concentration after 160 h was obtained by recalculating on the basis of the variation in corrosion rate given in [3].

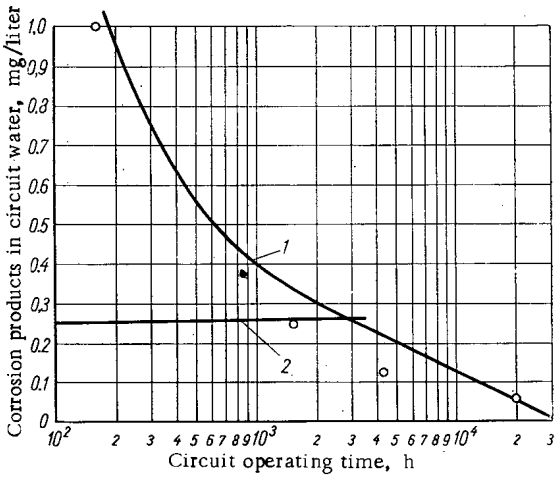

Fig.1. Variation in corrosion-product concentration in the circuit water with operating time: 1) $C_c = f(t)$; 2) $C_c = const$.; —)calculated; ○) experimental data.

* Remaining notation here and hereinafter taken from [2].

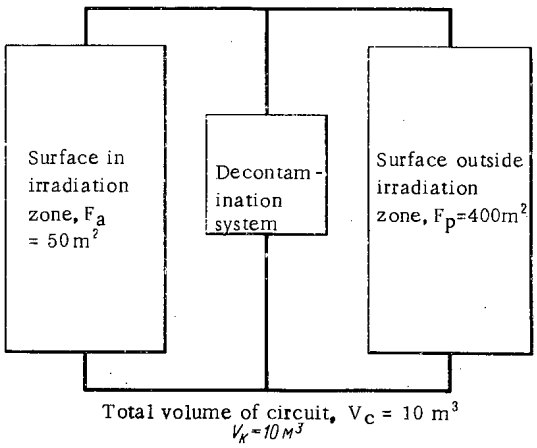

Fig.2. Arrangement of circuit for calculating the activity of the deposits.

In order to check the validity of the equilibrium relations of the (1) and (2) type obtained from the model chosen, we also calculated the corrosion rate of the circuit surface under steady conditions ($T_o \approx$ 15,000 to 20,000 h) [3] from the formula

$$C_c = \frac{\varepsilon_\Phi Q_\Phi}{F_c} \bar{N}_в. \quad (5)$$

The calculated value of $C_c = 0.55 mg/m^2 \cdot day$ is in good agreement with the experimental result (about 0.5 $mg/m^2 \cdot day$) [3].

The effect of the surface material on the activity of the corrosion deposits was studied for the circuit shown schematically in Fig.2. If was assumed in the calculations that the composition of the corrosion products (by elements) was the same as that of the main metal, and the amount of Co^{59} in the steels equalled 0.7% of the nickel content.

Figure 3 gives the calculated dose rates at the surface of equipment situated outside the active zone of the reactor and washed by the heat carrier. The calculations were made for different combinations of circuit surface materials. The cross sections for the activation of isotopes by thermal neutrons were averged with due allowance for the effective temperature of the neutron gas.

The following table gives the calculated contributions (in %) of various isotopes to the total activity of the deposits after 12,000 h operation of a circuit made entirely of stainless steel. For comparison we also give the experimental values obtained in the SM-1 reactor, the circuit of which is also entirely made of stainless steel:

	Co^{60}	Co^{58}	Fe^{59}	Cr^{51}	Mn^{54}
Experiment [1]	26	22.1	14.3	32.5	3.9
Calculation	37.4	37.8	2.6	17.2	4.9

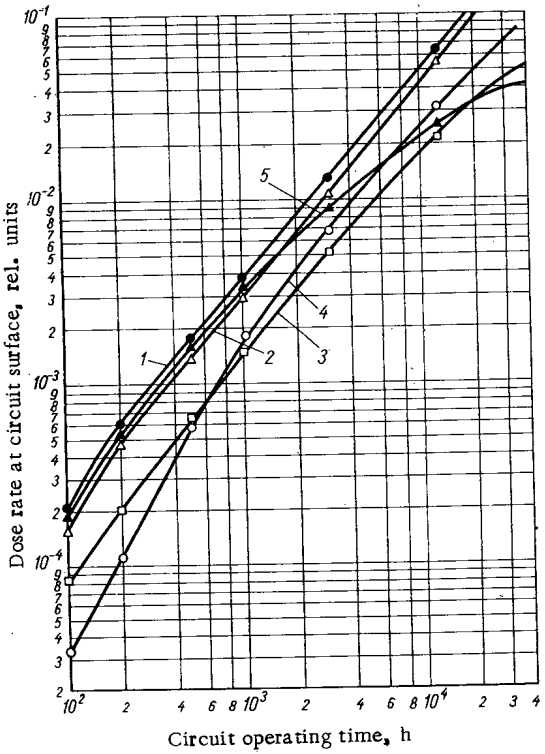

Fig.3. Dose rate at the surface of the circuit as a function of the reactor-operating time: 1) whole circuit made of stainless steel [3]; 2) surface of active zone made of stainless steel and the rest of the circuit of carbon steel; 3) surface of active zone made of zircalloy; rest of the circuit made of stainless steel; 4) same as 1) but for C_c = const.; 5) same as 1) but amount of cobalt in steel 14 times less.

DISCUSSION OF RESULTS

The results of the calculations show that the mathematical model taken and the washout and deposition constants used give a fairly good description of the build-up of the corrosion products in the water and on the surface of the reactor system. The assumption that the corrosion rate C_c = const leads to an underestimate of the concentration of inactive corrosion products in the water and on the surface of the circuit in the initial period of operation of the system, but the underestimate in the activity of the deposits is not too serious, not more than a factor of two (see curves 1 and 2 of Fig.1 and curves 1 and 4 of Fig.3).

The activity of the deposits for a fairly efficient scavenging system $\lambda_\Phi \gtrsim k_d$ is determined as might be expected, by the corrosion and washout from surfaces situated in the active zone. Curves 1 and 2 in Fig.3 show that the contribution to the activity of the deposits arising from surfaces outside the active zone is in this case no greater than 10%.

The activity ratio $Co^{60}/Co^{58} = 0.99$, calculated for a reactor system which has been operating for 12,000 h agrees closely with the value obtained experimentally [1], which is equal to 1.17.

The use of the same washout, deposit, and filter-efficiency constants for all the long-living elements is

not such a coarse approximation as might at first seem. Almost all these elements belong to the iron group and have fairly similar chemical properties. Possibly this is not entirely correct for zirconium, the calculated activity of which (based on the washout and deposition constants taken) may be a little overestimated.

From the point of view of subsequent servicing of the reactor system, the best construction materials to use are zirconium alloys (Zircaloy type) for surfaces in the active zone and carbon steel for surfaces outside this region (see curves 1 and 3 of Fig.3). After 12,000 h operation of the reactor system, the dose rate created by the deposits in a 0-to-30-day interval after reactor shutdown is some three to five times higher for variant 1 (see Fig.3) than for variant 3 (curve 3). This difference will increase with the period of operation of the system.

Curve 5 in Fig.3 characterizes the change in the activity of the deposits on the surface of the circuit for the case in which the Co^{59} content of the stainless steel is reduced to 0.05% of the nickel concentration. In this case, the activity of the deposits is mainly determined by the Co^{58} formed as a result of an (n, p) reaction with Ni^{58}. Hence, in order to improve the repair conditions of a reactor system with a water heat carrier, it is extremely desirable to use nickel-free (e.g., chromium-manganese) stainless steels as construction materials (naturally with the same corrosion resistance). After about 20,000 h (or 2 years) operation, systems made of this steel will be the most favorable for repair from the point of view of radiation safety.

The authors wish to thank L. I. Korzhenevskaya and E. M. Voronova for help in carrying out the numerical calculations.

LITERATURE CITED

1. F. J. Bratshy et al., In the collection "Corrosion of the Construction Materials of Water-Cooled Reactors" [Russian translation]. Edited by V. P. Pogodin. Moscow, Atomizdat, p.329 (1965).
2. A. P. Veselkin and O. Ya. Shakh, Atomnaya Énergiya, 21, 462 (1966).
3. A. N. Grigor'yants, Atomnaya Énergiya, 2, 109 (1957).

CHANGE IN THE ELECTRICAL RESISTANCE OF NICKEL, IRRADIATED BY α-PARTICLES, ON ANNEALING

I. Ya. Dekhtyar, V. S. Mikhalenkov, V. V. Pilipenko, and V. I. Silant'ev

UDC 539.12+621.039.553

The kinetic changes in the electrical resistance of nickel irradiated with 12.4-MeV α-particles on annealing at various temperatures were studied. At temperatures above 700°C, the kinetic curves first showed a rise and afterwards a fall in electrical resistance. This behavior corresponds to the usual laws governing the decomposition of supersaturated solid solutions and is associated with the development of helium-filled pores.

The resultant data agree with theoretical investigations relating to the mechanism and kinetics of pore formation in the decomposition of supersaturated metal — noble-gas solutions.

The results obtained were used to estimate the mean size of the gas pores evolved at various annealing temperatures. This was in fact about 140 A, varying little with annealing temperature.

The swelling of fissile and construction materials in a reactor is associated with the formation of pores in metals saturated with inert gases. It is well known that inert gases are extremely insoluble in metals; after they have been artificially introduced (producing a considerable supersaturation) and the temperature is raised, the supersaturated solid solution therefore rapidly decomposes, forming gas pores in the metal. The inert gases creating supersaturation may be introduced into the metals in several ways, especially by α-particle bombardment. A certain proportion of α-particles are retained in the metal as a result of absorption, and this leads to saturation with helium. We used this method in order to saturate nickel with this gas.

A 0.1-mm thick foil of 99.99%-pure nickel was first vacuum-annealed at 900°C for 2 h and irradiated with 12.4-MeV (mean energy) α-particles in a cyclotron at 30°C. The integral dose of irradiation was 10^{14} particles/cm^2. Samples about 2 mm wide were prepared from the irradiated (helium-saturated) foil.

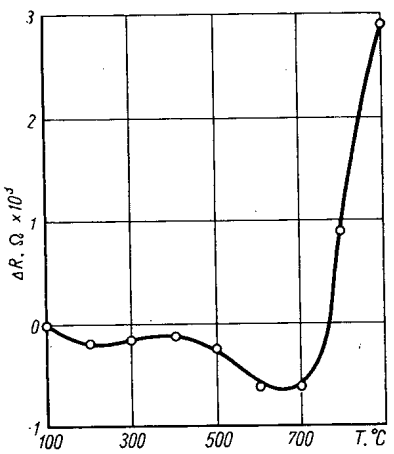

Fig. 1. Change in the electrical resistance (of nickel) for isochronous annealing.

The electrical resistance of the samples was measured by a potentiometer method to an accuracy of 0.05%, the samples being kept in an ultra thermostat at a constant temperature of 35 ± 0.05°C. The samples were vacuum-annealed at a residual pressure of $5 \cdot 10^{-4}$ mm Hg. The annealing temperature was measured and maintained to an accuracy of ± 5°C. The increment in the electrical resistance of the nickel after irradiation with the dose indicated was about 7.7%.

Figure 1 shows the change in the electrical resistance as a result of annealing for 1 h at various temperatures. The curve shows that, up to a temperature of about 700°C, the electrical resistance falls, clearly as a result of the healing (annealing) of defects arising during irradiation. At higher temperatures (> 700°C) there is a sharp rise in electrical resistance. This suggests that there is a high rate of pore formation at such temperatures.

Translated from Atomnaya Énergiya, Vol.21, No.6, pp.465-470, December, 1966. Original article submitted May 27, 1966.

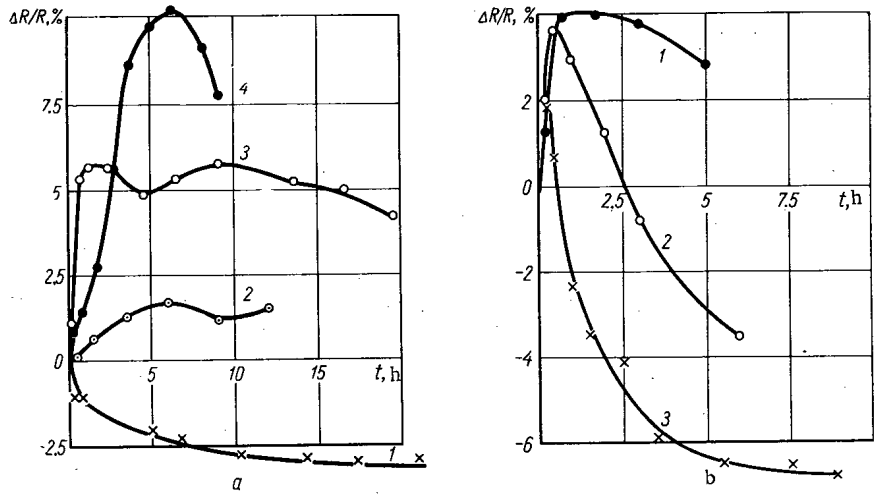

Fig.2. Kinetics of the change in electrical resistance (of nickel) after isothermal annealing at various temperatures, °C: a: 1) 700, 2) 750, 3) 800, 4) 850; b: 1) 900, 2) 950, 3) 1000.

The kinetic curves (Fig.2) indicate the complete recovery of the electrical resistance of irradiated nickel after annealing at 1000°C for 9 h, which demonstrates the insignificant influence of the geometrical factor on the specific electrical resistance, since this is the same for the original nickel and the nickel containing coalesced pores.

The electrical-resistance curves at high temperatures (850 to 1000°C) are typical of processes associated with the decomposition of a supersaturated solid solution, and are characterized by a sharp rise in electrical resistance, followed by a drop.

On the other hand, at 700°C (Fig.2 a), the electrical resistance first falls and then, after annealing for 10 h, reaches saturation. Annealing at 750 and 800°C is accompanied by a rise in electrical resistance, but without any fall, although this may appear after longer annealing periods.

The differences in the form of the kinetic curves in question are doubtless due to qualitative and quantitative differences in the processes taking place at different temperatures.

Since stresses, associated with the formation of various kinds of defects, arise on irradiating nickel with α-particles, the fall in the electrical resistance on annealing at 700°C is presumably due to a reduction in these stresses, resulting from the mobility of the defects under such conditions. Naturally this process should also take place in the initial stages of annealing at higher temperatures, at which the mobility of the defects increases rapidly. Nevertheless, since the conditions of irradiation are the same for all samples, the contribution of the mobile defects to the change in electrical resistance should be considered the same in all cases.

It is already known [1-5] that high-temperature annealing after low-temperature irradiation leads to the formation of a large number of pores, filled with inert gases, in the metal. Thus the change in the electrical resistance of a supersaturated solid solution of helium in nickel at the first stage of annealing should be due to the scattering of conductivity electrons at newly-generated and growing pores and also at crystal-lattice defects arising as a result of the α-particle irradiation.

This may be expressed in general form as follows:

$$\Delta\rho = \sum_i N_d^{(i)}\rho_d^{(i)} + N_v\rho_v(r_n), \qquad (1)$$

where $N_d^{(i)}$ is the density of crystal-lattice defects of type i, $\rho_d^{(i)}$ is the corresponding specific electrical resistance, N_V is the density of the pores, and $\rho_V(r_n)$ is the specific resistance of pore of size r_n(here r_n is the mean pore radius).

If we call $\Delta\rho_V$ the change in the specific resistance of the sample due to the presence of pores only, we may determine the number of pores from (1) by means of the formula

$$N_v = \frac{\Delta\rho_v}{\rho_v(r_n)}. \quad (2)$$

If the crystal-structure defects vanish as a result of high-temperature annealing, for which they have a high mobility, then the residual effect of the change in electrical resistance will be mainly determined by the scattering of electrons at the pore surfaces and by elastic strains arising around these. On the other hand, if the conditions fail to allow the rapid formation of a considerable number of large pores, the change in electrical resistance will be mainly determined by mobile defects.

The curve representing the change in the electrical resistance of nickel subjected to isochronous annealing after irradiation with α-particles (see Fig.1) shows that, at temperatures above 700°C, the change in electrical resistance is mainly due to the formation and growth of pores and their subsequent coalescence, so that the fall in electrical resistance after annealing at 700°C is due to the healing of mobile defects. Probably, under these conditions, the nuclei of the new phase (gas-filled pores), although present, are very small, and, since the diffusion processes are very slow (the diffusion coefficient of the gas in nickel at this temperature is of the order of 10^{-16} cm^2/sec), the pores cannot coalesce, so that they give a negligibly small contribution to the change in electrical resistance on annealing.

This fact is supported by data relating to the change in the electrical resistance of quenched aluminum [6]. It was shown that neither the increase in volume due to pore growth, nor the reduction in the effective cross section of the sample due to the presence of pores, could influence the change in electrical resistance. In other words, the role of the geometrical factor in the change of electrical resistance is negligible. In addition to this, it was found that the specific electrical resistance of the pores increased in proportion to the square of their size, this relation being valid not only for large pores (50 to 100 Å) but even for pores of sizes equal to those of atomic vacancies.

This latter circumstance shows that increasing the pore size 10 times should raise the electrical resistance 100 times. This means that at annealing temperatures of 700°C or less (for which the pores generated are still very small) the pore contribution to the change in electrical resistance is slight, so that the annealing kinetics are determined by changes in the number of mobile defects.

Annealing samples irradiated by α-particles at 750 to 1000°C is accompanied, in the initial stage (Fig.2), by a rise in electrical resistance, due to the intensive growth and coalescence of pores.

Figure 3 shows the form of the change in electrical resistance associated with annealing, including all the stages observed experimentally. The following treatment of the successive stages in annealing kinetics may be considered. We remember that we are considering the annealing of metal previously bombarded by α-particles. This state is taken as origin and indicated by point 0. At a fairly high temperature, mobile defects developing in the course of irradiation may in principal take part in the generation and partial growth of the gas-phase nuclei, although these vanish quite quickly. Hence in section OB the rise in electrical resistance is due to the formation and growth of pores. If at this stage the pores reach subcritical dimensions, at which an important part is played by the redissolution of the "new-phase grains", coalescence of the gas-filled pores begins. Apparently this process also takes part on section BC, after time τ_g. The slowing down of the rise in electrical resistance and its subsequent fall may be due to two competing sources: the continuing rise in pore size and the reduction in the number of pores.

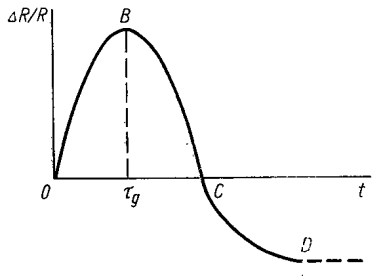

Fig.3. Schematic curve representing the change in the electrical resistance of irradiated samples subjected to isothermal annealing.

According to [6], the change in the electrical resistance associated with the increase in pore size is proportional to r^2, i.e., $\Delta\rho_V = Ar^2$. On the other hand, according to the theory of the coalescence of gas pores [4], we should have $r = B\tau$. On this basis we may suppose that $\Delta\rho = C\tau^2$. Here A, B, and C are constants depending on the number of pores, the parameters of the diffusion processes, the surface tension, and the elastic properties of the metal.

If the number of pores falls far more rapidly with time than their size increases [4, 5], then at the stage of intensive coalescence (BC in Fig.3) we may expect a fall in electrical resistance.

In addition to this, at stage BC there is a relaxation in the elastic stresses created by the pressure of the gas in the pores. This process continues further in section CD, and may clearly go on until the electrical resistance becomes equal to that of nonirradiated nickel.

Thus the mechanism proposed for the change in the electrical resistance of a metal subjected to annealing after preliminary irradiation with α-particles includes all the possible stages associated with the various processes taking place.

Since the coalescence of gas pores plays an important part in the mechanism governing the swelling of material, it is desirable to analyze the changes in electrical resistance associated with annealing in greater detail.

The theory of the phenomena associated with swelling was developed in [2, 4, 5, 7]. Of special interest are [4, 5], in which certain limiting cases of gas-containing pores were considered.

The following expression for the growth of pores was obtained in [4] (allowing for previous results in [1]):

$$\frac{dr_n}{dt} = \frac{D^V}{r}\left(\Delta + \alpha\frac{n^p}{4/3\pi r^3} - \frac{\beta}{r}\right). \tag{3}$$

Here Δ is the degree of saturation with vacancies, D^V is the diffusion coefficient of the vacancies, n^p is the amount of gas in a pore, $\alpha = C_0^V\omega_0$; $\beta = \frac{2\gamma C_0^V\omega_0}{kT}$, where C_0^V is the equilibrium concentration of vacancies in the crystal lattice, ω_0 is the volume associated with one vacancy, and γ is the surface tension of the metal.

An equation was also obtained for the change in the amount of gas in a pore:

$$\frac{dn^p}{dt} = 4\pi D^p r\left(C^p - \delta\frac{n^p}{4/3\pi r^3}\right), \tag{4}$$

where D^p is the diffusion coefficient of the gas atoms, C^p is the amount of gas per cm^3 of metal, and $\delta = \exp\left(\frac{-\varphi}{kT}\right)$.

The authors of [4] found asymptotic expressions for the two limiting cases of $\tau_g \ll 1$ and $\tau_g \gg 1$, where τ_g is the characteristic time for the change in pore size; for the annealing condition with $\Delta = 0$ this may be calculated from equation (3):

$$\tau_g \approx \frac{r^2}{D^a}\left(\frac{r^3}{\omega_0 n^p}\right). \tag{5}$$

Here $D^a = C_0^V D^V$ is the self-diffusion coefficient of the metal atoms, and τ_0 is the "characteristic time" for the change in the quantity of gas in the pore, which may be found from equation (4):

$$\tau_0 \approx \frac{r^2}{D^p\delta}. \tag{6}$$

The first limiting case is typical of the early stages of coalescence and the second applies to later stages.

In the case $\tau_g/\tau_g \ll 1$, the pores first grow to dimensions determined by the amount of gas in the pore; from the condition

$$\frac{dr_n}{dt} = \frac{D^a}{r}\left(\alpha\frac{n^p}{4/3\pi r^3} - \frac{\beta}{r}\right) = 0 \tag{3'}$$

and on the assumption that there is little change in n^p during the pore growth period, this gives (For $\Delta = 0$)

$$n^p = \frac{4}{3}\pi\frac{\beta}{\alpha}r_n^2 \tag{7}$$

in accordance with equation (3). From (5) and (7), remembering the values of α and β, we obtain

$$\tau_g \approx \frac{3kTr_n^3}{8\pi\gamma\omega_0}\cdot\frac{1}{D^a}. \tag{8}$$

We may consider that the characteristic time for the change in pore size τ_g on the electrical-resistance curve for isothermal annealing corresponds to the maximum change in electrical resistance.

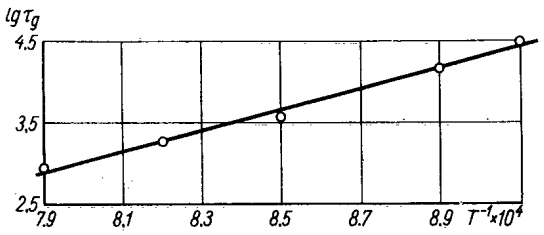

Fig.4. Temperature dependence of τ_g.

Dimensions of Gas Pores at Various Temperatures

T_{ann}, °K	D^a, cm²/sec	τ_g, sec	$\bar{r}_n$, Å
1073	$0.5\cdot10^{-14}$	$3.25\cdot10^{-4}$	120
1123	$0.16\cdot10^{-13}$	$2.16\cdot10^{-4}$	135
1173	$0.64\cdot10^{-13}$	$3.6\cdot10^{-3}$	135
1223	$0.16\cdot10^{-12}$	$1.8\cdot10^{-3}$	145
1273	$0.5\cdot10^{-12}$	$0.9\cdot10^{-3}$	168
		Mean	140±12

In fact, since at this stage the change in electrical resistance is proportional to the square of the pore size

$$\Delta R_v = cN_v r_n^2, \tag{9}$$

where c is a factor allowing for the geometry of the sample and N_V is the number of pores in unit volume with a mean radius of r_n, the condition for state B on the curve of Fig.3, $d\Delta R_V/dt = 0$ corresponds to condition (3'), from which we obtain expression (8) for the characteristic time τ_g.

In equation (8), the self-diffusion coefficient of the atoms may be replaced by the expression

$$D^a = D_0 e^{-Q/RT},$$

where Q is the activation energy of self-diffusion.
Then we obtain

$$\tau_g = \frac{3kTr_n^3}{8\pi\gamma\omega_0 D_0} e^{Q/RT} = \tau_{g0} e^{Q/RT}. \tag{9'}$$

A graph of $\lg \tau_g$ versus T^{-1} (T = annealing temperature) is shown in Fig.4, from which we see that τ_g closely obeys an exponential law with respect to the reciprocal of the temperature. The activation energy found was 70,000 cal/mole, in very good agreement with the activation energy of the self-diffusion of nickel measured by the radioactive-isotope method [8], which equalled 66,800 cal/mole. After determining the value of τ_{g0} from Fig.4, we may estimate the mean pore size from the formula

$$r_n^3 \approx \frac{8\pi\gamma\omega_0 D_0}{3kT} \tau_{g0}. \tag{10}$$

Using the corresponding values of $\gamma = 1600$ dyn/cm [9], $D_0 = 1.27$ cm²/sec [8], $\omega_0 = 0.8\cdot10^{-23}$ cm³, and $T_{av} = 1200$°K, and $\tau_{g0} \approx 5\cdot10^{-10}$ sec, we obtain $r_n \approx 150$ Å.

On the other hand, by using published data for the self-diffusion parameters of nickel [8], $D_0 = 1.27$ cm²/sec and Q = 66.8 kcal/mole, we can calculate the self-diffusion coefficient D^a and estimate the mean pore size from the measured values of characteristic time τ_g. The resultant data are shown in the table.

As we should expect, the resultant value of $\bar{r}_n$ differs little from that calculated by formula (10).

It should be noted that there is in fact a certain spread of pore sizes, and the mean value of $\bar{r}_n$ obtained characterizes the probable value of this quantity, which, according to our analysis and the tabulated data, depends very slightly on temperature.

LITERATURE CITED

1. I. M. Lifshits and V. V. Slezov, ZhÉTF, 35, 479 (1958).
2. V. M. Arganovich, É. Ya. Mikhlin, and L. P. Semenov, Atomnaya Énergiya, 15, 393 (1963).
3. G. Greenwood, A. Foreman, and O. Rimmer, J. Nucl. Materials, 1, 305 (1959).
4. Z. K. Saralidze and V. V. Slezov, Fizika Tverdogo Tela, 7, 1605 (1955).
5. L. P. Semenov, Atomnaya Énergiya, 15, 404 (1963).
6. S. Yoshida, M. Kiritami, and T. Yamagata, J. Phys. Soc. Japan, 20, 1662 (1965).
7. V. M. Arganovich and É. Ya. Mikhlin, Atomnaya Énergiya, 12, 385 (1962).

8. S. D. Gertsriken and I. Ya. Dekhtyar, Diffusion in Metals and Alloys in the Solid Phase [in Russian]. Moscow, Fizmatgiz, (1960).
9. V. K. Semenchenko, Surface Phenomena in Metals and Alloys [in Russian]. Moscow, Gostekhizdat, (1957).

EFFECT OF NEUTRON IRRADIATION ON THE STRUCTURE AND PROPERTIES OF LANTHANUM HEXABORIDE

M. S. Koval'chenko, V. V. Ogorodnikov, and A. G. Krainii

UDC 621.038.553:546.654

The effects of neutron irradiation at integral fluxes of 10^{18} and 10^{20} neutrons/cm^2 on lanthanum hexaboride were studied. Data relating to the radiation resistance, changes in lattice parameter, microhardness, microbrittleness, and color of LaB_6 were obtained. The effect of annealing on the recovery of the properties of the irradiated samples were studied. The microstructure of samples subjected to irradiation and subsequent annealing contained precipitates of a new phase, probably a double hexaboride of lanthanum and lithium with a microhardness of about 46 GN/m^2.

Compounds of rare-earth elements with boron, hitherto mainly used in electronics [1, 2], have in recent years come to be considered as promising materials for the control systems of nuclear reactors [3-6]. In addition to a large slow-neutron capture cross section, these compounds have high melting points and chemical resistance in many aggressive media [1, 7, 8,], which is of special importance in reactor development [9]. There is nevertheless very little information on the effects of nuclear radiations on the borides of rare-earth elements [10-12].

This paper is devoted to a study of radiation effects in lanthanum hexaboride (LaB_6). The samples for study were obtained by the hot pressing of LaB_6 powder (containing 31.3 wt.% boron, 0.1 wt. % carbon, and about 0.5 wt. % oxygen) in graphite molds. The samples had the form of cylinders 8 mm in diameter and up to 10 mm long. The residual porosity was about 10%. The lanthanum hexaboride was irradiated with integral thermal-neutron fluxes of 10^{18} and 10^{20} neutrons/cm^2 in the vertical water-cooled channel of a water-cooled water-moderated nuclear reactor (VVR-M) situated in the reflector zone. The irradiation temperature was no greater than 100°C. The ratio of fast to thermal neutrons was 1:10. The burn-up of isotope B^{10} in the surface layer of the sample was calculated from the formula [9]

$$\frac{N}{N_0} = 1 - \exp(-\sigma\Phi t),$$

where N is the number of burnt-up B^{10} atoms, N_0 is the original number of B^{10} atoms, σ is the microscopic capture cross section of B^{10}, equal to 4010 b [13], Φ is the thermal-neutron flux multiplied by F, the flux-perturbation factor at the surface (for absolutely absorbing samples, F = 0.6 [14]), and t is the irradiation time.

For a dose of 10^{18} neutrons/cm^2, allowing for the contribution of the fast neutrons, the burn-up of B^{10} is 0.1%, and for a dose of 10^{20} neutrons/cm^2 it equals 17%, which corresponds to a reduction of 0.02 and 2.9 at.% respectively in the total amount of boron in the surface layer of the LaB_6.

In view of the short free path of slow neutrons in lanthanum hexaboride [12], the burn-up of B^{10} nuclei should fall rapidly on approaching the center of the sample. The average burn-up over the whole volume of the sample may be calculated by the Lewis formula [14]

$$\varkappa = \frac{f\Phi V}{\lambda},$$

where $\varkappa$ is the rate of burn-up, f is the perturbation of the flux in the sample, Φ is the unperturbed flux, V is the sample volume, and λ is the absorption length. For a dose of 10^{18} neutrons/cm^2, the average burn-up is negligibly small. Increasing the dose by 100 times leads to a burn-up of about 1% of the B^{10}

Translated from Atomnaya Énergiya, Vol. 21, No. 6, pp. 470-476, December, 1966. Original article submitted April 19, 1966.

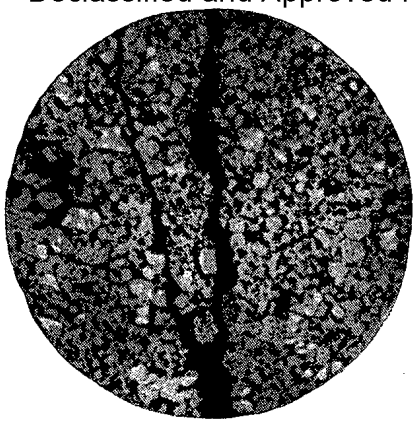

Fig. 1. Cracks in irradiated samples of lanthanum hexaboride.

nuclei. Actually the value of $(N/N_0)_{av}$ is rather higher, since irradiation breaks up the samples, leading to an increase in the irradiated surface. In addition to this, the absorption cross section of LaB_6 is only known for thermal neutrons (energy 0.025 eV), whereas boron has a considerable absorption cross section up to an energy of 10 to 15 eV. Hence the effective neutron flux absorbed in the sample is greater than that of the thermal neutrons.

Radiation Resistance. By the radiation resistance of components made of a particular material we mean primarily the ability to withstand changes in dimensions, the formation of macro- and microcracks, or the complete rupture of the components under the influence of nuclear radiations [9, 15]. Investigation showed that, after irradiation with an integral flux of 10^{20} neutrons/cm^2, the samples of lanthanum boride broke up and were converted into particles between one and several mm in size. Some of these continued to break up on carrying out subsequent operations (preparation of microsections for metallographic study and so forth) as a result of the existence of large cracks formed during irradiation (Fig. 1).

A dose of 10^{18} neutrons/cm^2 was insufficient to rupture the samples, change their shapes, or produce cracks.

Crystal Structure. Lanthanum hexaboride crystallizes the cubic system with a space group of O_h^1 - Pm3m, and a structure of the CaB_6 type. The cubic lattice points accommodate metal atoms enclosed in a strong octahedral framework of boron atoms [1]. Irradiation with neutrons leads to considerable damage of this framework or skeleton, as a result of the displacement of the metal and boron atoms (under the influence of the fast neutrons) and the burn-up of the B^{10} atoms.

The reaction products (lithium and helium) have high energies (0.5 and 1.5 MeV respectively) and produce considerable additional displacements of the lattice atoms. This weakens the bonds between the atoms and considerably increases the lattice spacings.

X-ray diffraction examination was carried out in the URS 50-IM diffractometer. Reflections from the {(431) (510)} and {(333) (511)} planes were recorded with a goniometer-rotation rate of 1/4 deg/min. The lattice spacing was calculated from the position of the integral center of the diffraction line dividing the area of the diffraction peak (determined with a planimeter) into two equal parts [16]. The results were averaged over three samples, the diffraction peak being recorded twice for each sample (in the forward and reverse directions).

The lattice spacing of nonirradiated lanthanum hexaboride was 4.1527± 0.0004 Å, in good agreement with published data (4.153 Å) [17]. Irradiation with an integral flux of 10^{20} neutrons/cm^2 increased the lattice spacing to 4.1642 ± 0.0004 Å, i.e., by 0.28%.

On estimating the stresses of the first kind [18] from the relation

$$\sigma = E\frac{\Delta d}{d}$$

(d = the interplanar spacing, E = Young's modulus, equal to 488 GN/m^2 for LaB_6 [17]), we obtained a value of about 1.37 GN/m^2. The elastic energy was determined [19] from

$$W = \frac{E\varepsilon^2}{3(1-\nu)},$$

where ν is Poisson's ratio and $\varepsilon = \Delta d/d$.

We may take $\nu = 1/3$ and so deduce W = 81.1 J/g-mole for LaB_6 irradiated with an integral flux of 10^{20} neutrons/cm^2 (i.e., 0.4 J/g).

Rough estimates of the same kind showed that the energy stored on developing stresses of the first kind in BeO constituted about 0.05%, and in graphite and diamond 6%, of the total stored energy found from calorimetric measurements [20, 21]. The total energy is predominantly associated with the

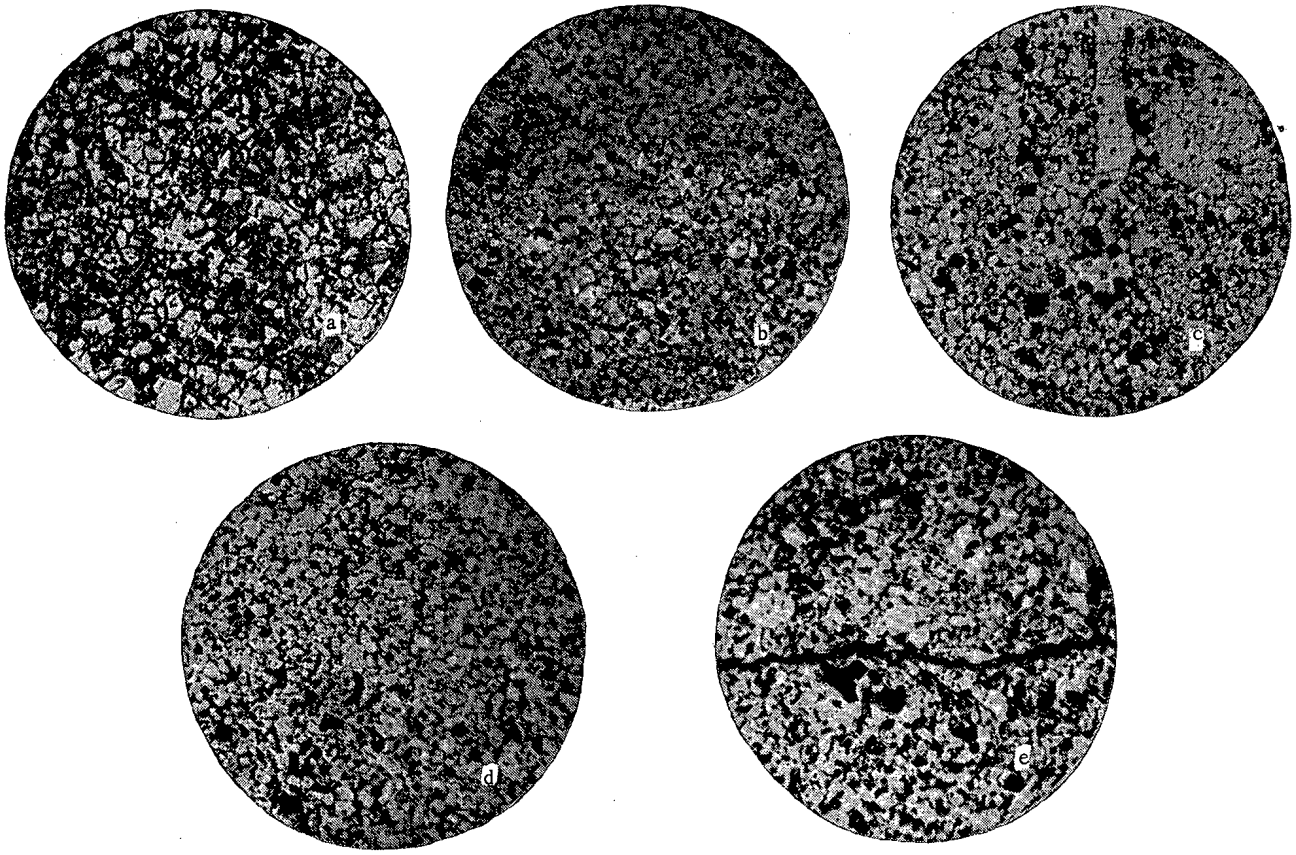

Fig. 2. Microstructure of LaB_6 (× 200): a) before irradiation; b) after irradiation with an integral flux of 10^{20} neutrons/cm^2;c) after irradiation and annealing at 400°C; d) after irradiation and annealing at 600°C; e) after irradiation and annealing at 800°C.

development of statistical displacements of the atoms, i.e., with stresses of the third kind, the energy of which may be determined [22] from the formula

$$U = \frac{1}{2} C_p \Delta T,$$

where C_p is the specific heat and ΔT the effective temperature. Calculation of the effective temperature from the change in lattice spacing ($a = 4.1642$ Å, $a_0 = 4.1527$ Å) and thermal-expansion coefficient $\alpha = 6.4 \cdot 10^{-6}$ deg^{-1} gives $\Delta T = 433$°C. Since the value of C_p for LaB_6 is 116.6 J/g-mole. deg [17], $U \approx 25{,}140$ J/g-mole, or 123.2 J/g, which corresponds to the values of stored energy found in metals [23].

Microstructure. Microsections of the samples, previously fixed with Wood's alloy in special holders, were prepared with the help of diamond pastes on an automatic grinding machine in a protective chamber of the 2KZ type. Then the structure of the samples was studied in a remote-control MIM-14-1 optical microscope.

At a small magnification, a few large cracks, broadening in the middle and narrowing at the ends, were visible (Fig. 1). Some cracks had branches.

On comparing grain sizes before and after radiation for samples etched in preheated 50% nitric acid, no marked changes were observed.

Samples of both irradiated and nonirradiated lanthanum hexaboride were characterized by the existence of intergrain and intragrain porosity; hence no micropores resulting from the build-up of helium atoms could be found (Fig. 2).

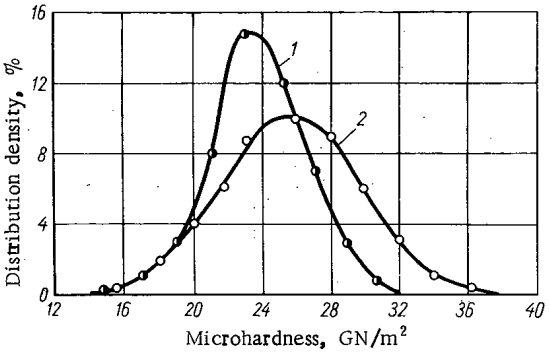

Fig. 3. Effect of neutron irradiation on the microhardness distribution-density curve of LaB_6: 1) before irradiation; 2) after irradiation with an integral flux of 10^{20} neutrons/cm^2.

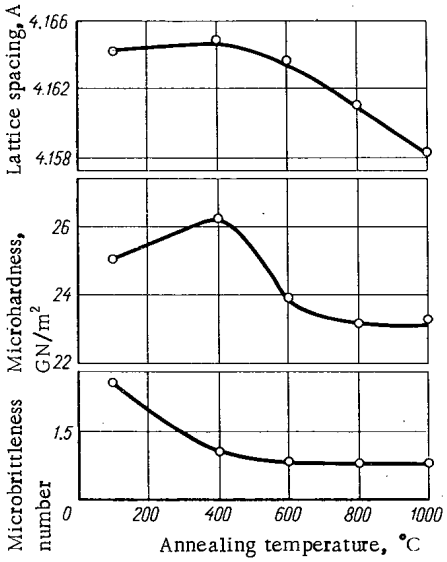

Fig. 4. Effect of annealing temperature on the changes in lattice spacing, microhardness, and microbrittleness of LaB_6 irradiated with a dose of 10^{20} neutrons/cm^2.

Optical Properties. Neutron irradiation with a dose of 10^{18} neutrons/cm^2 changes the color of lanthanum hexaboride from violet to violet-blue, and for a dose of 10^{20} neutrons/cm^2 to dark blue with a weak violet tinge.

Hence in addition to defects in the crystal lattice there are defects in the electron structure; these should differ from the color centers characteristic of ionic crystals owing to the presence of free electrons.

Microhardness. Measurements were made on a remote-control microhardness tester of the PMT-4 type with a load of 100 g. Three hundred measurements were made (100 on each sample) both before and after irradiation. The results are shown in Fig. 3., from which we see that neutron irradiation changes the form of the distribution-density curve, i. e., the irradiated material becomes more inhomogeneous. The average value of microhardness was determined by measuring the area under the curve with a planimeter. Irradiation with an integral flux of 10^{20} neutrons/cm^2 changed its value from 23.2 to 25.0 GN/m^2, or by 7.5%.

The displacement of the distribution-density curve and the shift in its maximum are due to the pinning of dislocations at radiation defects. The spread of the curve indicates the increased volume inhomogeneity of the structure due to the development of zones or regions of radiation damage. These regions or zones include large numbers of atoms situated in irregular positions. We may suppose that these regions correspond to thermal peaks or zones of displacement [21].

Microbrittleness. In measuring the microhardness, we noted the number of impressions with cracks and the number and character of the cracks at each impression; this gave us the total "brittleness number" in accordance with the formula

$$Z_p = 0n_0 + 1n_1 + 2n_2 + 3n_3 + 4n_4 + 5n_5,$$

where the indices 0 to 5 are the brittleness numbers [24] and n_i is the relative number of impressions with the corresponding brittleness number.

On irradiating with an integral flux of 10^{20} neutrons/cm^2 the value of Z_p rises sharply (from 0.5 to 2.2, i. e., by 4.4 times). It is known that the generation of damage centers takes place as a result of the localization of strain and the blocking of slip in a region of crystal-lattice imperfections [25]. The microbrittleness results obtained show that the radiation defects lead to the formation of cracks.

Thermal Recovery of Radiation Effects. Radiation defects are thermally unstable; at high temperatures the properties of the unirradiated materials are therefore restored. In lanthanum hexaboride not all the radiation effects are reversible, since impurity atoms of lithium and helium appear in the lattice.

In order to study thermal recovery, LaB_6 samples were annealed in an argon medium for 1 h at temperatures of 400, 600, 800, and 1000°C. In analyzing the results, data obtained from three parallel samples were averaged.

We see from Fig. 4 that annealing at 400°C led to a considerable recovery of microbrittleness and an increase in microhardness. At an annealing temperature of 600°C the microhardness and lattice spacing

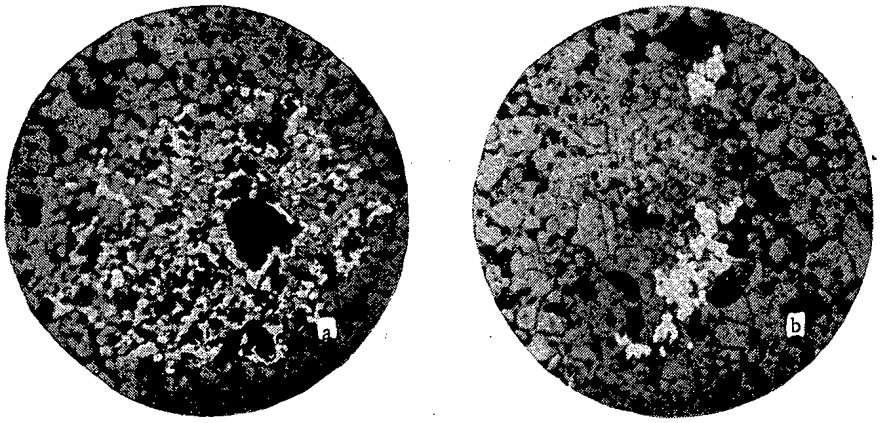

Fig. 5. Precipitates of a new phase (white regions) after annealing irradiated LaB_6 (× 400).

began recovering, although the over-all brittleness number remained 0.6 higher than the original. At 800°C the microhardness recovered completely and changed very little with further rise in temperature. The lattice spacing fell monotonically, but still remained 0.0055 Å high.

The rise in microhardness after annealing at 400°C was due to the interaction of impurity atoms (lithium and helium) with dislocations. The impurity atoms were attracted by the dislocations and parts of these dislocations were thus pinned. The pinning effect was associated with the fall in the energy of the system when an impurity atom penetrated into the stress field of the dislocations. Electrical (Coulomb) and chemical interaction may contribute to this process [23].

The pinning of the dislocations by impurity atoms may not entirely prevent their rearrangement into an energetically more favorable configuration. Raising the temperature to 400°C leads to the thermally-activated slipping of dislocations, as a result of which the dislocations occupy energetically more favorable positions. Hence the effectiveness of the incipient cracks formed by irradiation falls, and this appears in the considerably reduced microbrittleness.

Raising the temperature to 600°C produces a fall in microhardness and a reduction in the lattice spacing as a result of the healing of statistical distortions brought about by the diffusion mobility of the radiation defects. The acceleration of the self-diffusion process at temperatures above 600°C contributes to the further displacement and rearrangement of the dislocations on the basis of a creep mechanism. Annealing at 1000°C completely restores the violet color of LaB_6.

The annealed samples contained a new phase in the form of bright white inclusions, easily visible on the background of dull LaB_6 grains and black pores (Fig. 5). More careful analysis of the microstructure of the irradiated samples (before and after annealing) and of the nonirradiated samples showed that similar inclusions also occurred in the irradiated material; the number, and especially the size, of these inclusions, however, were much smaller than in the annealed samples. As regards the nonirradiated samples, in very rare cases we were able to see extremely fine glistening spots similar to the inclusions found in the irradiated material.

The new phase, the concentration of which rises considerably on subsequent annealing of the irradiated samples, is not unexpected, since, in view of the reaction B^{10} (n, α) Li^7, lithium impurity atoms appear in the crystal lattice. Borides of alkali metals are unknown, but, in the presence of rare-earth elements, double hexaborides, in which the amount of alkali metal does not exceed a certain limiting value [26], are formed. Hence the phase appearing after annealing is evidently a double hexaboride of lanthanum and lithium. The microhardness of this phase is about 46.0 GN/m^2, which is considerably higher than in the double hexaboride (La, Na)B_6 (22.0 to 32.0 GN/m^2). Such a difference between the microhardnesses of the analogous compounds is quite reasonable, since the interatomic bonds formed by the $2s^1$ electrons of lithium should be stronger than those arising from the $3s^1$ electrons of sodium, and an increase in bond strength should produce an increase in the Peierls-Nabarro forces and a corresponding reduction in ductility [27].

The formation of the new phase is observed primarily on the surface of grains bordering pores. Figure 5a clearly illustrates the initial stage in the formation of large precipitates similar to those in Fig. 5b.

Thus neutron irradiation of lanthanum hexaboride with an integral flux of 10^{20} neutrons/cm^2 leads to the formation of large cracks and the breaking of the samples into fractions between one and several mm in size.

The lattice spacing rises by 0.28% owing to the build-up of static distortions. The stored energy associated with the static distortions is about 25 kJ/g-mole, or 123.2 J/g, which corresponds to the stored energy in irradiated metals. The average microhardness rises by 7.5% and the degree of microbrittleness rises 4.4 times, the color of the LaB_6 changing from violet to dark blue.

Annealing at 400 to 1000°C affects the properties of irradiated lanthanum hexaboride as follows: There is a complete restoration of color and microhardness and a partial restoration of lattice spacing and degree of microbrittleness. The increase in the microhardness of irradiated lanthanum hexaboride after annealing at 400°C is due to the interaction of dislocations with impurity atoms of lithium and to the increase in the critical stress necessary for initiating the operation of Frank-Reed sources.

The healing of radiation defects becomes considerable at 800 and 1000°C, owing to the possibility of diffusion processes taking place.

The microstructure of samples subjected to irradiation and subsequent annealing contains precipitates of a new phase, probably a double hexaboride of lithium and lanthanum, with a microhardness of about 46.0 GN/m^2.

LITERATURE CITED

1. G. V. Samsonov and Yu. B. Paderno, Borides of Rare-Earth Metals [in Russian], Kiev, Izd. AN UkrSSR (1961).
2. J. Binder and R. Steinitz, Planseeber. Pulvermetallurgie, 7, 18 (1959).
3. J. Binder, J. Amer. Ceram. Soc. 43, 287 (1960).
4. K. Gschneider, Rare Earth Alloys. Amsterdam, D. Van Norstrand Co. (1961).
5. New Studies of Rare-Earth Metals. [Collection of Russian translations]. Edited by E. M. Savitskii. Moscow, "Mir", p. 212 (1964).
6. B. G. Arabei, In the collection: "Absorbing Materials for Controlling Nuclear Reactors" [in Russian] Moscow, Atomizdat, p. 421 (1965).
7. G. V. Samsonov et al, Boron, Its Compounds and Alloys [in Russian]. Kiev, Izd. AN UkrSSR, p. 57 (1960).
8. J. G. Westbrook, In the collection "High-Temperature Studies" [Russian translation]. Moscow, IL, p. 195 (1962).
9. I. S. Bairon, In the collection "Absorbing Materials for Controlling Nuclear Reactors" [in Russian]. Moscow, Atomizdat, p. 133.
10. A. Holden et al, Properties of Reactor Materials and the Effects Radiation Damage, London, p. 457 (1962).
11. I. D. Konozenko and V. S. Neshpor, "Poroshkovaya Metallurgiya", No. 1, 60 (1965).
12. M. S. Koval'chenko et al., Data Relating to the Effects of Neutron and Gamma Radiation on Refractory Compounds" [in Russian]. Kiev, Izd. AN UkrSSR (1963).
13. Physicochemical Properties of Elements [in Russian]. Edited by G. V. Samsonov. Kiev, "Naukova Dumka" (1965).
14. Wm. Lewis, Nucleonics, 13, 82 (1955).
15. B. Kopel'man, Materials for Nuclear Reactors [in Russian]. Moscow, Izd. AN SSSR (1962).
16. D. M. Kheiker and L. S. Zevin, X-Ray Diffractometry [in Russian]. Moscow, Fizmatgiz (1963).
17. G. V. Samsonov, Handbook "Refractory Compounds" [in Russian]. Moscow, Metallurgizdat (1963).
18. B. Ya. Pines, Lectures on Structural Analysis [in Russian]. Khar'kov, Izd. Khar'kovskogo gosudarstvennogo universiteta (1958).
19. L. D. Landau and E. M. Lifshits, Theory of Elasticity [in Russian]. Moscow, "Nauka" (1965).
20. R. Andre et al., Ekspress-informatsiya. "Atomnaya Énergiya", No. 21, 2 (1964).
21. G. J. Dienes and G. H. Vineyard, Radiation Effects in Solids, Wiley, N. Y. (1957).
22. G. S. Zhdanov, Solid-State Physics [in Russian]. Moscow, Izd. MGU, p. 447 (1961).

23. H. G. Van Bueren, Imperfections in Crystals, 2nd ed., Interscience (1961).
24. V. M. Glazov and V. N. Vigdorovich, Microhardness of Metals [in Russian]. Moscow, Metallurgizdat, p. 206 (1962).
25. B. I. Smirnov and V. D. Yaroshevich. In the collection "Physical Nature of the Brittle Failure of Metals" [in Russian]. Kiev, "Naukova Dumka". p. 6 (1965).
26. G. V. Samsonov et al. In the collection "Questions on the Theory and Use of Rare-Earth Metals" [in Russian]. Moscow, "Nauka", p. 180 (1964).
27. D.McLean, Mechanical Properties of Metals [Russian translation]. Moscow, Metallurgizdat, p. 33 (1965).

INTERACTION OF TETRAVALENT URANIUM WITH THE CHLORIDE-FLUORIDE MELT NaCl — KCl — NaF

M. V. Smirnov, A. P. Koryushin, and V. E. Komarov

UDC 541.138:661.879

The method of measuring the oxidation-reduction potential of U(III)/U(IV) was used to investigate the interaction of uranium tetrachloride with a chloride-fluoride melt. The measurements were performed in a molten equimolar mixture of sodium and potassium chlorides, containing 3% by weight U and 8.0-18.5% by weight NaF, within the interval 973-1123°K.

It was established that U^{+4} forms the fluoride complex UF^{-2} in a melt of the investigated composition. An expression was found for the temperature dependence of the instability constant of this complex in a NaCl — KCl — NaF melt:

$$\overline{\log} K = 0.95 - \frac{16\,200}{T} \pm 0.25.$$

One of the methods of producing metallic uranium is the electrolysis of chloride-fluoride melts containing tetravalent uranium [1, 2]. Moreover, solutions of this kind can be used to obtain crystalline uranium dioxide [3]. However, the absence of information on the thermodynamics of the interaction of tetravalent uranium with molten fluoride-chloride mixtures required a special study of this question.

We had earlier investigated the equilibrium between metallic uranium and a melt NaCl — KCl-NaF containing uranium ions [4]. It was established that chiefly trivalent uranium is in equilibrium with the metal; in the presence of excess fluoride ions, it forms the fluoride complexes UF_5^{-2}; moreover, the instability constant of this complex is described by the equation

$$\log K_1 = 0.84 - \frac{9800}{T} \pm 0.04. \quad (1)$$

Using these data and the results of a determination of the redox potential in the chloride melt NaCl — KCl [5], we can find the composition of the fluoride complex of tetravalent uranium and its instability constant in the melt NaCl — KCl — NaF. For this purpose it is necessary to measure the redox potential of the system U(III)/U(IV) in the indicated melt at various temperatures, fluoride ion concentrations, and a definite uranium content.

Actually, the Nernst formula for the redox potential of U(III)/U(IV) in the chloride salt melt NaCl — KCl takes the form

$$E = E^0_{U^{3+}/U^{4+}} + \frac{RT}{F} \ln \frac{[U^{4+}]}{[U^{3+}]}, \quad (2)$$

where

$$E^0_{U^{3+}/U^{4+}} = -1{,}906 + 4{,}87 \cdot 10^{-4} T; \quad (3)$$

$[U^{+4}]$, $[U^{+3}]$ are the molar fraction concentrations of tetra- and trivalent uranium.

If fluoride anions are introduced into the system, then we should expect the reaction of complex formation

$$U^{3+} + 5F^- \rightleftarrows UF_5^{2-}$$

and

$$U^{4+} + mF^- \rightleftarrows UF_m^{(m-4)-},$$

where m is the number of fluoride ions bonded in the fluoride complex with tetravalent uranium.

Translated from Atomnaya Énergiya, Vol. 21, No. 6, pp. 476-478, December, 1966. Original article submitted July 4, 1966.

The instability constants of the complexes formed are correspondingly equal to

$$K_1 = \frac{[U^{3+}]\,[F^-]^5}{[UF_5^{2-}]}; \tag{4}$$

$$K_2 = \frac{[U^{4+}]\,[F^-]^m}{[UF_m^{(m-4)-}]}, \tag{5}$$

where $[UF_5^{-2}]$, $[UF_m^{(m-4)-}]$ are the molar fraction concentrations of tri- and tetravalent uranium contained in the complex compounds; $[F^-]$ is the molar fraction concentration of the free fluoride ions, i.e., not bonded in complexes.

Substituting the concentrations of uranium not contained in complex compounds from (4) and (5) into (2), we obtain an expression for the redox potential in chloride-fluoride melts:

$$E = E^0_{U^{3+}/U^{4+}} + \frac{RT}{F}\ln\frac{K_2}{K_1} + \frac{RT}{F}\ln\frac{[UF_m^{(m-4)-}]}{[UF_5^{2-}]} - (m-5)\frac{RT}{F}\ln[F^-]. \tag{6}$$

From (6) it follows that at constant temperature and a definite uranium content with a fixed ratio of the oxidized form to the reduced form, the redox potential of the system will be determined only by the concentrations of free fluoride anions. Then let us write (6) in the form

$$E = \text{const} - (m-5)\frac{RT}{F}\ln[F^-], \tag{7}$$

moreover, we can obtain the value of m directly according to the value of the prelogarithmic coefficient. Knowing the number m and using functions (1) and (2), it is easy to find the temperature dependence for the instability constant of the fluoride complex of tetravalent uranium according to equation (6).

Below are presented the results of our measurements within the interval 973-1123°K for a molten eutectic mixture of sodium and potassium chlorides, containing 3% by weight U and 8.0-18.5% by weight NaF.

EXPERIMENTAL SECTION

In the experimental respect, the work was reduced chiefly to a measurement of the emf of the cell, of the type

$$\begin{array}{l}\text{Indicator electrode}\\ \text{(molybdenum)}\end{array} \Big| \text{molten } NaCl - KCl + xU^{3+} + (1-x)U^{4+} + y\text{NaF} \,\|\, \text{molten } NaCl - KCl \,|\, C,\ Cl_2.$$

Salt mixtures prepared according to the well-known procedure of [4] were used as the electrolyte. Uranium was introduced into the electrolyte by anodic dissolution of the metal at a current density of $\sim 0.1\ A/cm^2$. When the metal dissolved and trivalent uranium was subsequently oxidized, the role of the cathode was played by the chloride electrode. Before loading of uranium into the cell, its surface was cleaned by etching in hot nitric acid, after which it was washed in water, ethanol, ether, and dried. A boron nitride crucible was used as the container for a melt. The measuring and regulating apparatus was described earlier [4]. The redox potential was measured with a molybdenum indicator electrode. Before the experiment the cell was evacuated and filled with helium, purified of traces of water and oxygen by repeated passage over phosphoric anhydride and metallic calcium, and heated to 780°C. The residual oxygen in the helium was absorbed by a metallic uranium getter directly in the cell at 850°C.

RESULTS OF THE MEASUREMENTS

Table 1 presents the results of measurements of the emf at a definite composition of the electrolyte and different temperatures. From the table we can find the redox potential of U(III)/U(IV). It is equal to the difference of the emf and thermal emf between molybdenum and carbon current leads [6], taken with the opposite sign. Then the dependence of the redox potential of the system U(III)/U(IV) on the temperature at a definite composition of the electrolyte is written in the form of the following equations:*

$$E_1 = -3{,}010 + 4{,}87\cdot10^{-4}T \pm 0{,}005b \quad \left(\frac{[F]}{[U]} = 30;\ \frac{[U\,(IV)]}{[U\,(III)]} = 1\right);$$

$$E_2 = -3{,}107 + 5{,}92\cdot10^{-4}T \pm 0{,}006b, \left(\frac{[F]}{[U]} = 25;\ \frac{[U\,(IV)]}{[U\,(III)]} = 1\right);$$

* These and the following empirical equations were found from the experimental data by the method of least squares.

TABLE 1. emf Between Molybdenum and Chloride Reference Electrode (Uranium Concentration 3% by Weight)

[F]/[U]=30		[F]/[U]=25		[F]/[U]=20		[F]/[U]=19		[F]/[U]=15 *	
T, °K	emf	T, °K	emf	T, °K	emf	T, °K	emf	T, °K	emf
989	2.523	982	2.523	975	2.499	979	2.474	973	2.411
1005	2.504	1001	2.498	989	2.487	1003	2.449	996	2.391
1021	2.508	1029	2.491	1024	2.449	1022	2.455	1015	2.395
1051	2.487	1052	2.472	1044	2.454	1048	2.418	1047	2.369
1074	2.480	1080	2.458	1060	2.425	1068	2.427	1063	2.372
1085	2.470	1096	2.453	1078	2.428	1098	2.398	1083	2.354
1106	2.460	1123	2.429	1093	2.405	1118	2.390	1113	2.343

* In this case [U(IV)]/[U(III)] = 1.5; in all other cases this ratio is equal to 1.

TABLE 2. Instability Constant of the Fluoride Complex UF_6^{-2} in a Melt NaCl — KCl — NaF

T, °K	−log K	T, °K	−log K	T, °K	−log K
973	15.6	1022	14.9	1078	14.1
979	15.7	1024	14.8	1080	14.1
979	15.5	1029	14.8	1083	14.0
982	15.6	1044	14.6	1085	14.0
989	15.4	1047	14.5	1093	13.8
989	15.4	1048	14.4	1096	13.9
996	15.2	1051	14.4	1098	13.8
1001	15.2	1052	14.5	1106	13.8
1003	15.1	1060	14.3	1113	13.7
1005	15.1	1063	14.3	1118	13.6
1015	15.0	1068	14.3	1123	13.5
1021	14.9	1074	14.1		

$$E_3 = -3.219 + 7.32\cdot10^{-4}T \pm 0.009b, \left(\frac{[F]}{[U]} = 20;\ \frac{[U(IV)]}{[U(III)]} = 1\right);$$

$$E_4 = -3.040 + 5.73\cdot10^{-4}T \pm 0.008b, \left(\frac{[F]}{[U]} = 19;\ \frac{[U(IV)]}{[U(III)]} = 1\right);$$

$$E_5 = -2.860 + 4.55\cdot10^{-4}T \pm 0.006b, \left(\frac{[F]}{[U]} = 15;\ \frac{[U(IV)]}{[U(III)]} = 1{,}5\right).$$

The change in the redox potential as a function of the concentration of free fluoride ions in the melt at constant temperature and [U(IV)]/[U(III)] = 1 is characterized by the equations

$$E_6 = -2.717 - 0.23 \log [F^-] \quad (\text{for } 1000^\circ\text{K});$$
$$E_7 = -2\,646 - 0.22 \log [F^-] \quad (\text{for } 1100^\circ\text{K}).$$

The prelogarithmic factors in the equations obtained are close to the value of 2.3(m - 5)RT/F at the corresponding temperature and m = 6. Consequently, in the presence of excess fluoride anions, the tetravalent uranium ion interacts with the chloride-fluoride melt of the investigated composition, forming the complex UF_6^{-2}.

The expression for the temperature dependence of the instability constant K_2 in a molten mixture of NaCl — KCl — NaF, found according to the calculated values from Table 2, takes the form

$$\log K_2 = 0.95 - \frac{16\,200}{T} \pm 0.06$$

or considering the errors in the determination of log K_1 and $E^0_{U^{+3}/U^{+4}}$

$$\log K_2 = 0.95 - \frac{16\,200}{T} \pm 0.25. \qquad (8)$$

Thus, we may make the following summarizing statements:

1. The interaction of uranium tetrachloride with a melt of NaCl — KCl — NaF was studied by the method of measuring the redox potential.

2. It was established that in the investigated melt, tetravalent uranium forms the fluoride complex UF_6^{-2} in the presence of excess fluoride anions.

3. An expression for the temperature dependence of the instability constant of this complex in the molten mixture NaCl — KCl was found.

LITERATURE CITED

1. Ya. M. Sterlin, Uranium Metallurgy [In Russian]. Moscow, Gosatomizdat (1962).
2. G. E. Kaplan, G. F. Silina,and Yu. I. Ostroushko, Electrolysis in the Metallurgy of Rare Metals [In Russian], Moscow, Metallurgizdat (1963).
3. M. Schlechter et al. J. Nucl.Materials, 15, 3 (1965).
4. M. V. Smirnov, A. P. Koryushkin, and O. V. Skiba, In the book: Transactions of the Institute of Electrochemistry, Ural Affiliate of the Academy of Sciences of the USSR [In Russian], No. 8, Sverdlovsk, p. 47 (1966).
5. M. V. Smirnov, O. V. Skiba, Dokl. AN SSSR, 141, 5 (1961).
6. O. V. Skiba and M. V. Smirnov, In the book: Transactions of the Institute of Electrochemistry, Ural Affiliate of the Academy of Sciences of the USSR [In Russian], No. 2, Sverdlovsk, p. 3 (1961).

CONDITIONS OF THE DEPOSITION OF URANIUM FROM HYDROTHERMAL SOLUTIONS OF METAL DISULFIDES ACCORDING TO THE EXPERIMENTAL DATA

B. S. Osipov

UDC 550.41:553.21/24

On the basis of the experimental data it was shown that pyrite and molybdenite are effective reducing agents for hexavalent uranium from solutions of uranyl sulfate under conditions of increased temperatures. The reduction and deposition of uranium may occur from highly dilute solutions. The effectiveness of the process is greatly influenced by the temperature and pH of the medium. In addition, under the conditions of equilibrium with disulfides, substantial concentrations of hexavalent uranium, from the geochemical standpoint, may remain in the solutions.

It has been established that varied impurity elements, contained in pyrites from different deposits, have practically no effect upon the equilibrium concentrations of uranium in solution.

The results of experiments characterizing the temperature dependence of equilibrium concentrations of uranium in sulfate solutions in the presence of hydrogen sulfide [1], elementary sulfur [2], and some of the most important sulfides [3], were published earlier. In the last study it was shown that when the temperature is lowered from 360 to 200°C, the equilibrium concentrations of uranium in the presence of sulfide minerals increase.

In experiments with pyrite and molybdenite, the concentrations increase by almost four orders of magnitude and reach the first grams per liter at 200°C. These data were obtained for solutions with an initial uranium concentration of 10 g/liter. It may be assumed that the uranium content in natural hydrothermal solutions was substantially lower. Therefore, new experiments were conducted with pyrite, in which the uranium concentration in the original UO_2SO_4 solution was varied within broad limits. Moreover, we studied the dependence of the equilibrium concentration of uranium upon certain other factors.

All the experiments were conducted with natural samples of pyrite and molybdenite, preliminarily crushed and freed of inclusions of extraneous minerals in heavy liquids and under a binocular microscope. A microscopic study of the samples prepared showed that in pyrite from an unknown deposit, which was used in all the basic experiments, there are rare inclusions of fahlerz and galenite up to 0.04×0.01 mm in size, as well as individual inclusions of native gold and quartz. Rare inclusions of fluorite are noted in pyrite from the Kalangui deposit, and quartz in pyrite from the Central Deposit. Rare and fine crystals of beryll and inclusions of feldspar are encountered in molybdenite.

According to the data of spectral analyses, all the samples of pyrite contain arsenic (0.1-1%) and copper (0.0001-0.03%), while some contain Mn, Pb, Sn, Bi, Ag, and Sn. An especially high arsenic concentration (~1%) was noted in pyrite from Kalangui, while lead (0.1%) was found in pyrite from Shtribro. Molybdenite is characterized by increased concentrations of beryllium (0.1%), and impurities of Mn, Cu, Cr, Fe, and Ca. All the pyrite samples were analyzed by a chemical method.

In most of the experiments we used grains of the fraction -0.64+0.4 mm, and in certain methodological experiments, from the fractions -0.4+0 25 mm, -0.25+0.15 mm, and -0.15+0.064 mm. The amount of the mineral used in the experiments was measured by volume, which was 0.25 cm^3 in the basic experiments. As a result, the summary surface of the grains remained more or less constant and had no effect upon the rate of the reaction between the liquid and solid phases.

Translated from Atomnaya Énergiya, Vol.21, No.6, pp. 479-483, December, 1966. Original article submitted May 31, 1966.

All the experiments were conducted in quartz ampules, into which the sulfide and a solution of UO_2SO_4 of set concentration were introduced. The experimental procedure was described in more detail earlier [3]. The uranium concentrations were determined by a luminescent method according to the method of additives (without preliminary purification of the samples) [4, 5], considering certain corrections established in [6]. The iron concentrations were determined according to the degree of extinction of the luminescence of NaF fluxes [7]. The relative error in the determination of uranium does not exceed ±10%, that of iron ± (10-15)%.

Part of the determinations of uranium and iron were subjected to internal and external monitoring. External monitoring of the determination of uranium was conducted by a luminescent method after preliminary chemical purification of the investigated samples. The determination of the iron concentrations was monitored by a colorimetric method using sulfosalicylic acid. The relative error in the determinations did not exceed ± 10%.

EXPERIMENTAL RESULTS

The time needed to achieve equilibrium in the system was determined by special experiments with pyrite [3]. It was established that in the presence of pyrite, equilibrium in the system at 360° is reached in less than 3 h, and at 200°C in less than 25 h. The achievement of equilibrium was confirmed by a measurement of the amount of metal in the ampule, as well as of its grain size. On the basis of the results of preliminary experiments, the exposure time at the set temperature in the subsequent experiments was assumed equal to 120, 116, 78, and 54 h at 200, 250, 300, and 360°C, respectively.

The equilibrium reached at the experimental temperature may be displaced during cooling and filtration. Inasmuch as the equilibrium uranium concentrations in solution increase with decreasing temperature, they may increase upon cooling. The influence of the time of quenching was studied in experiments with molybdenite heated at 360°C for 48 h in solutions with initial uranium concentration 10 g/liter. Subsequent exposure of the ampules at room temperature for 24, 72, and 240 h has practically no effect upon the uranium concentration. Thus, the dissolution of uranium-containing solid phases, formed at the experimental temperature, proceeds rather slowly as the temperature is lowered, which agrees with the data obtained earlier for the system UO_2SO_4 — S — H_2O [2].

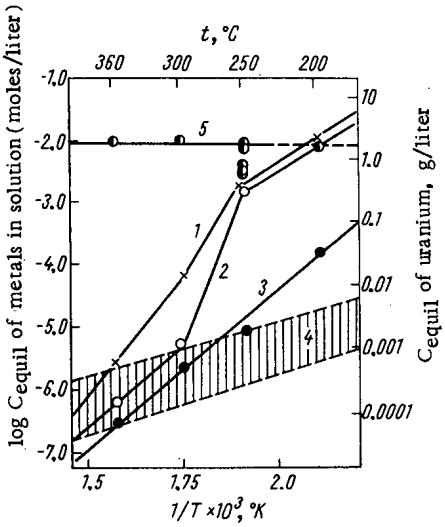

Fig.1. Dependence of log C_{equil} of metals in solution in the presence of pyrite and molybdenite upon 1/T °K: 1, 2) uranium concentrations in the presence of MoS_2 and FeS_2, respectively (initial uranium concentration 10 g/liter); 3) in the presence of FeS_2 (0.1 g/liter); 4) in the presence of simple sulfides: PbS, ZnS, $CuFeS_2$ (10 g/liter) [3]; 5) iron concentration in the presence of FeS_2 (initial uranium concentration 10 g/liter).

The results of an experimental study of the temperature dependence of the equilibrium concentration C_{equil} of uranium in the presence of pyrite and molybdenite are presented in Fig.1 (curves 1-3). The points on the graph represent average values of the concentrations, derived from the data of two to 24 experiments and converted to the volume of the solution at the temperature of the experiment. In the conversion it was assumed that at increased temperatures, the density of the solution is equal to the density of water, which comprises 0.865, 0.799, 0.712, and 0.525 g/cm³ at 200, 250, 300, and 360° C, respectively [8].

The data cited in Fig.1 show that at an initial uranium concentration in solution of 10 g/liter, the temperature dependence of the equilibrium concentrations in the presence of pyrite (2) and molybdenite (1) are close. At 200°C, the equilibrium concentrations of uranium are equal to 1.68-2.18 g/liter; at 360°C, they are 0.00015-0.00059 g/liter. Thus, with increasing temperature the uranium concentrations decrease (this is especially sharply manifested within the interval 250-300°C) by approximately 100-fold in the presence of pyrite.

The temperature dependence of the equilibrium concentrations of uranium at an initial concentration of 0.1 g/liter

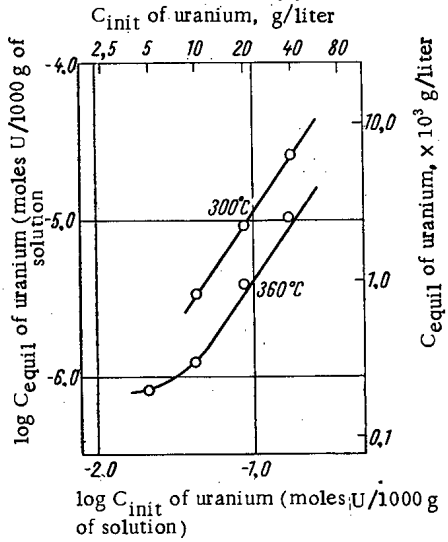

Fig.2. Dependence of log C_{equil} of uranium on C_{init} in solution in the presence of pyrite.

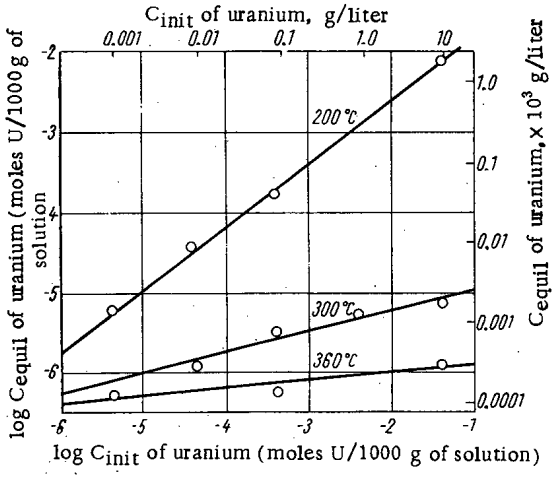

Fig.3. Dependence of log C_{equil} of uranium on C_{init} in solution in the presence of pyrite.

was studied in experiments with pyrite. To prevent the precipitation of hexavalent uranium as a result of hydrolysis, the solution was acidified to pH 1.6 with sulfuric acid. The results of these experiments show that the dependence of the logarithm of the equilibrium concentration on the reciprocal of the absolute temperature is expressed by a straight line (3 in Fig.1). The treatment of the experimental data by the method of least squares shows that this dependence is described by the equation

$$\log C_{equil} = \frac{4956,8}{T} - 14,400.$$

It should be mentioned that the graphs of the temperature dependences of the equilibrium concentrations of uranium in the presence of pyrite (2 and 3) and molybdenite (1) differ sharply in slope and partially in shape from the curves characterizing the analogous dependences in the presence of simple sulfides — galenite, sphalerite, and chalcopyrite (shaded region in Fig.1).

The dependence of the equilibrium concentration C_{equil} of uranium upon its initial concentration C_{init} in solution was studied in the presence of pyrite within the interval 40-0.001 g/liter U. The results of experiments conducted at relatively high initial uranium concentrations in solution (as a result of which the solution was not acidified with sulfuric acid) are cited in Fig.2.

With increasing initial uranium concentration from 10 to 40 g/liter, the equilibrium concentrations increase by almost an order of magnitude; moreover, from 300 to 360°C the dependences are expressed by parallel straight lines. However, the results of experiments conducted at an initial uranium concentration of 5 g/liter (360°C) permit us to assume that in the region of lower initial uranium concentrations, the graphs characterizing the dependence under consideration gradually become more sloping and almost parallel to the x axis.

The initial solutions of uranyl sulfate of low concentrations were acidified to pH 1.6; an exception was the solution with a concentration 10 g/liter. From the graphs of Fig.3 it follows that the equilibrium concentrations of uranium depend substantially upon the initial concentrations; moreover, this dependence is more pronounced, the lower the temperature.

In addition to the experiments described, we conducted a series of experiments with pyrite at 360°C, in which the initial solution, with uranium concentration 0.1 g/liter, was acidified with sulfuric acid to various pH values. The results of the experiments cited in Fig.4 show that pH in the region from 3 to 1.5 has practically no effect upon the equilibrium uranium concentration in solution. At pH values less than 1.5, the equilibrium uranium concentrations rapidly increase.

In the experiments we used natural samples of pyrite and molybdenite, containing impurities of various elements. To determine the influence of impurities on the equilibrium concentrations of uranium,

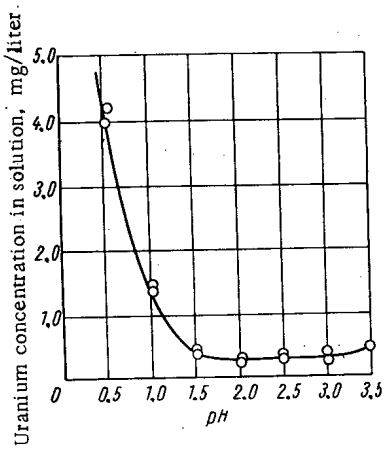

Fig. 4. Dependence of the uranium concentration in the presence of pyrite on the pH of the initial solution (t = 360°C; initial uranium concentration in solution 0.1 g/liter).

we conducted three experiments each with samples of pyrite taken from five different deposits at t = 300°C and uranium concentration in the initial UO_2SO_4 solution of 10 g/liter. From the results cited in the table it is evident that the equilibrium concentrations of uranium are practically the same in the presence of any of the samples.

DISCUSSION OF RESULTS

The experimental results show that the curves expressing the temperature dependence of the equilibrium uranium concentrations in the presence of pyrite and molybdenite are close in character but differ greatly from the analogous curves obtained for the simple sulfides — galenite, sphalerite, and chalcopyrite. A similar curve is also observed with respect to the absolute values of the uranium concentrations in solution. Pyrite belongs to the group of disulfides, i.e., minerals containing the complex anion S_2^{2-} [9]. The viewpoint exists that sulfur is also present in molybdenite in the form of the anion S_2^{2-} [9, 10]. In our opinion, the combination of experimental results is evidence in favor of a monotypic character of the anionic portion of pyrite and molybdenite. According to the data of [11], the coefficient of strength of the bond in disulfides is one-and-a-half to two times as high as in simple monosulfides, which contain sulfur in the form of the ion S^{2-}. The different strength of the crystal lattices of monosulfides and disulfides most likely also is the explanation for the anomalous behavior of the latter in their interaction with solutions.

In the presence of pyrite and molybdenite, a sharp drop in the equilibrium uranium concentrations is observed — from tenths to a few hundredths and even thousandths of a gram per liter — when the temperature is increased from 250 to 300°C. It may be assumed that such a sharp change in the uranium concentrations is due to an increase in the content of sulfide sulfur in solution, which is due to an abrupt change in the strength of the bonds in the disulfides in the indicated temperature interval.

As a result of oxidation-reduction reactions that occur between pyrite and the uranyl sulfate solution, on the one hand, there is a reduction of tetravalent uranium, and on the other an oxidation of divalent iron and sulfide sulfur. The presence of appreciable amounts of trivalent iron in solution after the experiment is confirmed by its intensive reaction with ammonium thiocyanate. In other cases, when the pH of the solution exceeded 2, iron oxides were observed in the form of a brownish-red deposit. Under the conditions under which the experiments were conducted, sulfur may be present in the form of the following ions (or nondissociated molecules): $S^{2-}(HS^-, H_2S)$, S^0, $SO_3^{2-}(HSO_3^-, H_2SO_3, SO_2)$, $SO_4^{2-}(HSO_4^-, H_2SO_4, SO_3)$.

When the ampules with pyrite were opened, especially after heating at 300 and 360°C, a strong odor of sulfur dioxide was noted. The deposition of elementary sulfur in the solid phase practically was not observed. Thus, it may be assumed that in the oxidation of sulfide sulfur, sulfur dioxide and the sulfate ion may be formed in appreciable amounts. The summary reactions of uranyl sulfate with pyrite

Equilibrium Concentrations of Uranium in Solution in the Presence of Pyrites from Different Deposits

	Deposit				
	Shtribro	Unknown	Central	Kalangui	Akchatau
Uranium concentration in solution, mg/liter	1.46 1.79 1.52	1.31 1.84 1.45	1.85 1.56 1.80	1.50 1.93 1.83	1.71 1.66 1.75

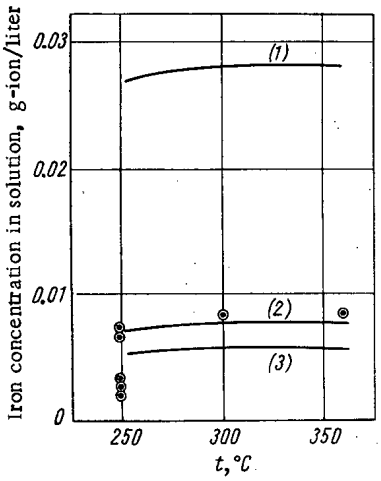

Fig. 5. Concentrations of iron determined experimentally (points) and calculated according to Eq. (1)-(3). Initial uranium concentration in solution 10 g/liter.

may be schematically represented by the following equations:

$$3UO_2SO_4 + 2FeS_2 = 3UO_2 + Fe_2(SO_4)_3 + 4S; \quad (1)$$

$$\| UO_2SO_4 + 2FeS_2 + 8H_2O = \| UO_2 + Fe_2(SO_4)_3 + 8H_2SO_4 + 4SO_2; \quad (2)$$

$$15UO_2SO_4 + 2FeS_2 + 16H_2O = 15UO_2 + Fe_2(SO_4)_3 + 16H_2SO_4. \quad (3)$$

Figure 5 shows a change in the iron concentrations in solutions in experiments with pyrite, calculated from Eqs. (1)-(3) under the condition that all the uranium originally present in solution is consumed in the reaction. The coincidence of the experimentally found iron concentrations with those calculated according to equation (2) indicates that at the temperatures 300 and 360° C the reaction proceeds according to an equation close to (2).

In experiments with pyrite at initial uranium concentrations from 10 to 40 g/liter, the ratio of the number of moles of the reaction products to the number of moles of the initial components (slope of the straight lines in Fig.2) was equal to 1.4. According to equation (2), this ratio should be equal to 1.2. It may be that the basic reaction is accompanied by side reactions, which do not influence the equilibrium concentrations of iron in solution.

The parallelism of the straight lines (Fig.2) expressing the dependence of the logarithm of the equilibrium uranium concentration on the logarithm of the initial concentration at 300 and 360°C confirms the fact that in this interval of temperatures and concentrations the same reaction (or reactions) occurs.

The absence of a linear dependence of the logarithm of the equilibrium uranium concentration in solution upon 1/T°K in the temperature region 200-360°C, as well as the sharp drop in this concentration within the interval 250-300°C, permit us to assume that at an initial uranium concentration in solution of 10 g/liter, the oxidation-reduction reactions of uranium with pyrite at 200-250°C and 300-360°C proceed according to different equations. This same fact is confirmed by the results of experiments with no initial uranium concentrations; the 200°C isotherm (Fig 3) differs sharply in slope from the 300 and 360° C isotherms.

It should be mentioned that the equilibrium concentrations of uranium in the presence of pyrite at the temperatures 300 and 360°C are equal to or very close to the equilibrium concentrations of uranium in the presence of simple sulfide minerals and comprise $n \times 10^{-4}$ to $n \times 10^{-5}$ g/liter. In [2, 3] it was shown that these concentrations are determined chiefly by the presence of uranium in solution in hexavalent form.

The author would like to thank R. P. Rafal'skii for his considerable aid and advice in the work.

LITERATURE CITED

1. R. P. Rafal'skii, In the book: Transactions of the Second International Conference on the Peaceful Uses of Atomic Energy (Geneva, 1958). Reports of the Soviet Scientist [in Russian]. Vol. 3, p. 33, Moscow, Atomizdat (1959).
2. R. P. Rafal'skii, A. D. Vlasov, and I. V. Nikol'skaya, Dokl. AN SSSR, 151, No.2 (1963).
3. B. S. Osipov and R. P. Rafal'skii, Atomnaya Énergiya, 18, 189 (1965).
4. G. Price, R. Ferretti, and S. Schwartz, Analyt. Chem., 25, 2 (1953).
5. V. F. Grigor'ev, V. F. Luk'yanov, and E. A. Duderova, Zh. Analit. Khim., XV, 184 (1960).
6. B. S. Osipov, Zh. Analit. Khim., XXI, 70 (1966).
7. B. S. Osipov, Izv. Vyssh. Uchebn. Zavedenii. Ser. Geol. i Razvedki, No.1, 48 (1966).
8. É. P. Vukalovich, Thermodynamic Properties of Water and Water Vapor [in Russian]. Moscow, Mashgiz (1955).
9. N. V. Belov, In the collection: Problems of Petrography and Mineralogy [in Russian]. Moscow, Izd. AN SSSR, p.7 (1953).

10. N. V. Belov, Mineralogical Collection of L'vov Geological Society at the University [in Russian], No. 9, 3 (1955).
11. A. S. Povarennykh, Hardness of Minerals [in Russian]. Kiev, Izd. AN USSR (1963).

All abbreviations of periodicals in the above bibliography are letter-by-letter transliterations of the abbreviations as given in the original Russian journal. *Some or all of this periodical literature may well be available in English translation.* A complete list of the cover-to-cover English translations appears at the back of the first issue of this year.

THERMODYNAMIC DATA ON THE STABILITIES OF URANINITES OF VARIABLE COMPOSITION IN SUPERGENE CONDITIONS

A. A. Drozdovskaya and Yu. P. Mel'nik

UDC 550.4:553.495

The authors give results of thermodynamic calculations of the stability fields of uraninites with different oxygen coefficients in pure water at 25°C and atmospheric pressure. They have also calculated the ionic solubilities of uraninites in aqueous solutions in the absence of complexing anions at different pH. They discuss the forms in which uranium is present in solutions, and the stabilities of anhydrous and hydrated uranium oxides. Finally, they draw conclusions regarding migration and deposition of uranium from natural aqueous solutions in the supergenesis zone.

Many problems of supergene ore formation and of changes in ore deposits in the weathering crust can be solved by thermodynamic methods. These methods were developed by Pourbaix [1] and Garrels [2, 3] and have proved very useful for various purposes, e.g., elucidating the conditions of stable existence of minerals, determining the ionic equilibrium ratios in solutions, and determining the conditions in which ore elements are deposited from natural solutions and exogenic deposits formed. Thermodynamic methods can also be used for determining the solubility of a mineral.

We plotted the stabilities of uranium oxides in water at 25°C and atmospheric pressure versus pH and Eh, and in some cases P_{CO_2} or ΣCO_2 [2, 4]. From an analysis of these we can draw important conclusions regarding the formation conditions of supergene uranium deposits particularly the uranium and uranium-vanadium deposits of the Colorado Plateau. However, published reports examine only equilibria of UO_2 as an anhydrous solid phase, and of $UO_2(OH)_2 \times H_2O(UO_3 \cdot 2H_2O)$ as a hydrated phase with simple or complex uranium ions in a solution, although natural uraninites never contain only U(IV) and have the general formula UO_x, where x (the oxygen coefficient) varies from 2.17 to 2.92 [5].

It is assumed that the uranium-oxygen system contains up to 22 different solid phases, at least 13 of which actually exist and some of which are found in nature [6].

A natural uraninite is probably not a continuous series of solid solutions of UO_2-UO_3 but (from the thermodynamic viewpoint, at least) a stable compound with a fixed x or a value of x varying within certain limits. A uraninite of intermediate composition may be a mixture of such stable compounds; in the pitchblende group some investigators distinguish a subgroup with composition varying from $UO_{2.30}$ to $UO_{2.67}$, containing mixed crystals of solid solutions of U_3O_8 in UO_2, and of UO_2 in U_3O_8 [6].

Reliable thermodynamic data have been obtained [7] for the following six compounds: U, UO_2, $UO_{2.25}$, $UO_{2.33}$, $UO_{2.67}$, UO_3 [7]. Regular changes in the thermodynamic values (enthalpy, free energy of formation and entropy) as we go from UO_2 to UO_3 must be reflected in changes of the boundaries of the solid-phase stability fields, the solubilities and other physicochemical properties of uraninites. In particular, Rozhkova and Serebryakova [8] have established experimentally a relation between pitchblende solubility and the UO_3/UO_2 ratio; this enables us to reveal the presence and distribution pattern of pitchblende varieties by the imprint method (phase analysis).

The new thermodynamic constants obtained for compounds intermediate between UO_2 and UO_3 have greatly extended the Garrels stability field diagrams and improved their accuracy [2-4]. Furthermore, we have calculated the solubilities of uraninites with different UO_3/UO_2 ratios in a wide range of pH. In all cases the analysis was limited to the stabilities of uranium oxides and ions in pure water in total absence of anions (HCO_3^-, CO_3^{2-}, SO_4^{2-}, etc.) which form complexes with uranium in solution.

Translated from Atomnaya Énergiya, Vol. 21, No. 6, pp. 483-492, December, 1966. Original article submitted May 31, 1966.

TABLE 1. Thermodynamic Parameters for Uranium Compounds

Compound	ΔZ^0, kcal/mole	Reference
UO_2	−246.9	[7]
$UO_{2,25}$	−256.0	[7]
$UO_{2,33}$	−258.0	[7]
$UO_{2,67}$	−268.5	[7]
UO_3	−275.5	[7]
$U(OH)_4$	−359.7	[10]
$UO_3 \cdot H_2O$	−339.5	Calculated by the authors
$UO_3 \cdot 2H_2O$	−398.8	[4]
$UO_3 \cdot 3H_2O$	−455.5	Calculated by the authors
U^{4+}	−138.5	[11]
UOH^{3+}	−193.5	[12]
UO_2^+	−237.9	[13]
UO_2^{2+}	−236.4	[12]
UO_2OH^+	−287.6	[10]
HUO_4^-	−317.6	[4]
OH^-	−37.6	[14]
H^+	0.0	[14]
H_2O_1	−56,7	[14]

INITIAL THERMODYNAMIC QUANTITIES AND STABILITIES OF THE SOLID PHASES

The selection of the thermodynamic quantities (Table 1) was governed by the accuracy and the method of the determination. We used mainly values obtained from experimental thermochemical determinations (principally for anhydrous uranium oxides); the thermodynamic values of ions in aqueous solutions are less reliable. The thermodynamic parameters obtained for the uranium hydroxides are the least accurate; some of these, particularly in the case of $UO_3 \cdot H_2O$ $UO_2(OH)_2$, were recalculated — we employed Brusilovskii's data [9] on the solubility of the hydroxide (the solubiltiy products SP are given in mole/liter)

$$UO_2(OH)_2 \rightleftarrows UO_2OH^+ + OH^-, \quad SP_1 = 1{,}35 \cdot 10^{-12}; \tag{1}$$

$$UO_2(OH)_2 \rightleftarrows UO_2^{2+} + 2OH^-, \quad SP_2 = 6 \cdot 10^{-18} \tag{2}$$

together with parameters for ions from recent reports (cf. Table 1).

The calculations may be illustrated by the example of (1):

$$K_{P_1} = [UO_2OH^+][OH^-] = SP_1 = 1.35 \cdot 10^{-12};$$

$$\log K_{P_1} = -\frac{(\Delta Z^0_{OH^-} + \Delta Z_{UO_2OH^+} - \Delta Z^0_{UO_2(OH)_2}}{1.364} = -11.87,$$

whence the free energy of formation $\Delta Z^0_{UO_2(OH)_2} = -341.3$ kcal/mole.

The value of $Z^0_{UO_2(OH)_2}$ thus calculated from SP_2 is −337.8 kcal/mole. The mean of these two values is taken as $-339 \cdot 5 \pm 1.8$ kcal/mole.

In calculating the value of $\Delta Z^0_{UO_3 \cdot 3H_2O}$ we assumed that this compound coexists stably with $UO_3 \cdot 2H_2O$, so ΔZ of the reaction

$$UO_3 \cdot 2H_2O + H_2O_1 \rightleftarrows UO_3 \cdot 3H_2O \tag{3}$$

under standard conditions is equal to zero; hence $\Delta Z^0_{UO_3 \cdot 3H_2O} = -455.5$ kcal/mole.

If we assume (as in [2]) that ΔZ is also equal to zero for the reaction

$$UO_3 \cdot H_2O + 2H_2O_1 \rightleftarrows UO_3 \cdot 3H_2O, \tag{4}$$

then $\Delta Z^0_{UO_3 \cdot 3H_2O} = -452.9$ kcal/mole (Garrels' value of ΔZ_{sp} for this hydrate, −376.4 kcal/mole, is incorrect).

The accuracies of these indirectly obtained free energies of uranium hydroxide formation are low and the errors may reach ± 5 kcal/mole.

The experimentally prepared hydrates of uranium trioxide correspond to the formula $UO_3 \cdot 2H_2O$. The monohydrate $UO_3 \cdot H_2O$ is usually formed when UO_3 is hydrated in air at 25°C. When the dihydrate is heated, mixed crystals of the dihydrate and monohydrate are obtained [15].

Various hydroxides with different moisture contents, e.g., schoepite $UO_3 \cdot 9/4H_2O$ and becquerelite $UO_3 \cdot 5/3H_2O$, are found in nature; "uranium blacks" (uranium oxide minerals) also contain a small amount of water. Uranium hydroxides are easily dehydrated. According to the authors of [16], even at low temperatures schoepite undergoes spontaneous dehydration with formation of hydroxides with the formula $UO_3(2 - x) \cdot H_2O$, where x varies from 0 to 1.

To calculate the stability fields of minerals we used the values of $\Delta Z^0_{UO_3 \cdot 3H_2O}$. However, bearing in mind the similarity of the thermodynamic values for uranium hydroxides with different moisture contents (and that the ΔZ of the transition of one hydroxide to another is close to zero) the stability field of $UO_3 \cdot 2H_2O$ can be replaced without appreciable error by that of the hydroxide with variable composition $UO_3 \cdot xH_2O$, where x varies from 1 to 3.

TABLE 2. Reaction and Equations Reflecting Stabilities of Solid Uranium Oxides

Reactions	Reaction equation	ΔZ_{298}, kcal/mole	Equation Eh = f (pH)	Reaction No.
Decomposition of variable-composition uranium oxides (anhydrous conditions)	$U_4O_9 = 3UO_2 + UO_3$	+7.8	—	(5)
	$2U_4O_9 = 5UO_2 + U_3O_8$	+8.0	—	(6)
	$U_3O_7 = 2UO_2 + UO_3$	+4.7	—	(7)
	$5U_3O_7 = 3U_4O_9 + U_3O_8$	−7.5	—	(8)
	$U_3O_8 = UO_2 + 2UO_3$	+7.6	—	(9)
	$3U_3O_8 = U_4O_9 + 5UO_3$	+15.0	—	(10)
Hydration and decomposition of variable-composition uranium oxides during reaction with liquid water	$UO_2 + 2H_2O = U(OH)_4$	+0.6	—	(11)
	$U_4O_9 + 2H_2O = 3UO_2 + UO_3 \cdot 2H_2O$	−2.1	—	(12)
	$U_3O_7 + 2H_2O = 2UO_2 + UO_3 \cdot 2H_2O$	−5.2	—	(13)
	$U_3O_8 + 4H_2O = UO_2 + 2UO_3 \cdot 2H_2O$	−12.2	—	(14)
	$UO_3 + 2H_2O = UO_3 \cdot 2H_2O$	−9.9	—	(15)
	$UO_3 + H_2O = UO_3H_2O$	−7.3	—	(16)
	$UO_3 + 3H_2O = UO_3 \cdot 3H_2O$	−9.9	—	(17)
Redox reactions involving total hydration of variable-composition uranium oxides	$UO_2 + 3H_2O \rightleftarrows UO_3 \cdot 2H_2O + 2H^+ + 2e^-$	+18.2	Eh = +0.39 − 0.06 pH	(18)
	$U_4O_9 + 11H_2O \rightleftarrows 4UO_3 \cdot 2H_2O + 6H^+ + 6e^-$	+52.4	Eh = +0.38 − 0.06 pH	(19)
	$U_3O_7 + 8H_2O \rightleftarrows 3UO_3 \cdot 2H_2O + 4H^+ + 4e^-$	+31.1	Eh = +0.34 − 0.06 pH	(20)
	$U_3O_8 + 7H_2O \rightleftarrows 3UO_3 \cdot 2H_2O + 2H^+ + 2e^-$	+5.9	Eh = +0.13 − 0.06 pH	(21)

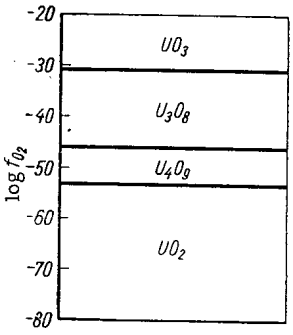

Fig. 1. Anhydrous uranium oxide stability versus log f_{O_2}

An analysis of the thermodynamic stabilities of the anhydrous uranium oxides used for the calculation showed that, with the exception of U_3O_7, all the anhydrous solid phases are stable (Table 2, reactions (5) - (10). This oxide is unstable and at given values of T and p must be converted to a mixture of the stable oxides U_4O_9 and U_3O_8 (for (8) the value of ΔZ is negative), like the thermodynamically unstable FeO, which decomposes at <650°C into Fe + Fe_3O_4 [17]. The metastable oxide U_3O_7 can probably exist for indefinite periods at supergenesis zone temperatures because the rates of solid-phase reactions under these conditions are very low; the ΔZ of (8) is also small and markedly less then the activation energies of such reactions in absence of a liquid phase. Thus the thermodynamically stable anhydrous solid phases in the system uranium-oxygen at 25°C and atmospheric pressure will be U, UO_2, U_4O_9, U_3O_8; the metastable but possibly kinetically stable phase will be U_3O_7.

The stabilities of anhydrous uranium oxides in absence of water are governed only by the volatility of oxygen, which is easily calculated for a redox reaction of the type

$$UO_n + \frac{m}{2} O_2 \rightleftarrows UO_{n+m} \qquad (22)$$

from the equation relating ΔZ to the equilibrium constant. In the converted form this equation for (5) is written as:

$$\log f_{O_2} = \frac{1.466}{m} \Delta Z_{\text{reaction}}.$$

Figure 1 plots anhydrous uranium oxide stability versus log f_{O_2}.

On the Earth's surface in contact with atmospheric oxygen, metallic uranium and all oxides containing U(IV) are unstable and will be oxidized to UO_3. Under supergene conditions the relative oxidation resistances of the different uranium oxides of variable composition are determined not by thermodynamic factors, but kinetic factors.

If we consider water as an oxidizing agent, in the presence of liquid water at 25°C all these compounds (with the exception of metallic uranium) are stable, i.e., oxidation of UO_2 by pure water to U_4O_9 and other higher oxides is thermodynamically improbable. On the other hand, in the presence of liquid water anhydrous uranium oxides may undergo hydration. It follows from the thermodynamic data that in liquid water in absence of redox reactions anhydrous UO_2 (cf. Table 2, reaction (11)) and $UO_3 \cdot 2H_2O$, or in the general case $UO_3 \cdot xH_2O$ [reactions (15) - (17)], are stable; uranium oxides of variable

composition U_4O_9 - U_3O_8 are unstable in water at 25° and will be converted to thermodynamically stable mixtures of anhydrous UO_2 and the hydrate $UO_3 \cdot 2H_2O$ [reactions (12) - (14)].

Such conversions are not likely to occur in natural conditions because hydration in the supergenesis zone is usually accompanied by oxidation of U^{4+} to U^{6+} by atmospheric oxygen or other oxidizing agents [18-20]. If hydration is not accompanied by oxidation, solid-phase disproportionation of the oxides U_4O_9 - U_3O_8 to a mixture of UO_2 and $UO_3 \cdot xH_2O$ is probably so slow at low temperatures that metastable uraninites of variable composition are retained in the weathering crust for fairly long periods.

In some cases experimental investigations established a marked difference between the manner in which U^{4+} and U^{6+} go into solution when natural uraninites and ore concentrates are dissolved in sulfuric acid (0.14-1.84 N) the difference increasing with the degree of oxidation of the uraninite [21]. Berman [22] assumes that when a uraninite with degree of oxidation > $UO_{2.32}$ dissolves in 0.4 N H_2SO_4 it undergoes disproportionation to a phase with a cubic structure, poorly soluble in acids, and an amorphous phase with a considerable amount of U^{6+}, easily soluble even in dilute acids. Owing to the marked increase in reaction velocity in a strongly acid medium, reaction of types (12) - (14) may take place in these experiments. However, we assume that in natural conditions such processes cannot take place with appreciable velocity in neutral, weakly acid or weakly alkaline solutions, and that uraninites with the composition U_4O_9 - U_3O_8 must be considered as metastable compounds which can exist for virtually indefinite periods in supergene conditions.

However, if hydration and oxidation take place simultaneously, uraninites of variable composition change fairly rapidly. In any case, mineralogical data enable us to draw the indirect conclusion that the reaction rates of simultaneous oxidation and hydration [cf. Table 2, reactions (18) - (21)] are considerably greater than the corresponding disproportionation and hydration reactions [(12) - (14)].

This conclusion forms a theoretical basis for studying the interrelations between thermodynamically stable hydroxides $UO_3 \cdot xH_2O$ and metastable anhydrous oxides U_4O_9, U_3O_7, and U_3O_8 in liquid water, and for constructing stability field diagrams.

EQUILIBRIUM OF VARIABLE-COMPOSITION URANIUM OXIDES, AND STABILITY FIELD DIAGRAMS

In an aqueous solution uranium may be present in four valence states: 3^+, 4^+, 5^+, and 6^+. Compounds of tri- or pentavalent uranium are unstable in solution: trivalent compounds are oxidized to tetravalent compounds by water, while pentavalent compounds decompose as follows:

$$2UO_2^+ + 4H_3O^+ \rightarrow U^{4+} + UO_2^{2+} + 6H_2O. \qquad (23)$$

Under natural conditions, tetravalent and hexavalent compounds must predominate in low-temperature solutions.

Compounds of Tetravalent Uranium in aqueous solutions form two stable ions U^{4+} and UOH^{3+}, the equilibrium between which is governed by reaction (24) of Table 3. It follows from (24) that the form in which U(IV) appears in solution is governed only by the pH.

TABLE 3. Reactions and Equations Reflecting Uranium Ion Ratios in Equilibrium Conditions

Reactions	Reaction equation	ΔZ_{298}, kcal/mole	Equation for Eh versus pH or equilibrium value of pH	Reaction No.
Between U^{4+} ions	$U^{4+} + H_2O \rightleftarrows UOH^{3+} + H^+$	+1.7	pH=1.2	(24)
Between U^{6+} ions	$UO_2OH^+ + H^+ \rightleftarrows UO_2^{2+} + H_2O$	—5.5	pH=4.0	(25)
	$HUO_4^- + 3H^+ \rightleftarrows UO_2^{2+} + 2H_2O$	—32.2	pH=7.9	(26)
	$HUO_4^- + 2H^+ \rightleftarrows UO_2OH^+ + H_2O$	—26.7	pH=9.8	(27)
Between U^{4+} ions and U^{6+} ions	$U^{4+} + 2H_2O \rightleftarrows UO_2^{2+} + 4H^+ + 2\bar{e}$	+15.5	Eh=+0.34—0.12 pH	(28)
	$UOH^{3+} + H_2O \rightleftarrows UO_2^{2+} + 3H^+ + 2\bar{e}$	+13.8	Eh=+0.30—0.08 pH	(29)
	$UOH^{3+} + 2H_2O \rightleftarrows UO_2OH + 4H^+ + 2\bar{e}$	+19.3	Eh=+0.42—0.12 pH	(30)

TABLE 4. Reactions and Equations Reflecting the Relations Between the Activities of Uranium Ions and Oxides

Oxide	Reaction equation	ΔZ_{298}, kcal/mole	Eq. for Eh versus ([C], pH) or for pH versus [C]	Reaction No.
UO_2	$UO_2 \rightleftarrows UO_2^{2+} + 2\bar{e}$	+10.5	$Eh = +0.23 + 0.03 \lg [UO_2^{2+}]$	(31)
	$UO_2 + H_2O \rightleftarrows UO_2OH^+ + H^+ + 2\bar{e}$	+16.0	$Eh = +0.35 + 0.03 \lg [UO_2OH^+] - 0.03$ pH	(32)
	$UO_2 + 2H_2O \rightleftarrows HUO_4^- + 3H^+ + 2\bar{e}$	+42.7	$Eh = +0.93 + 0.03 \lg [HUO_4^-] - 0.09$ pH	(33)
	$UO_2 + 3H^+ \rightleftarrows UOH^{3+} + H_2O$	−3.3	$pH = +0.8 + 0.33 \lg [UOH^{3+}]$	(34)
U_4O_9	$U_4O_9 + 2H^+ \rightleftarrows 4UO_2^{2+} + H_2O + 6\bar{e}$	+21.7	$Eh = +0.16 + 0.04 \lg [UO_2^{2+}] - 0.02$ pH	(35)
	$U_4O_9 + 3H_2O \rightleftarrows 4UO_2OH^+ + 2H^+ + 6\bar{e}$	+43.7	$Eh = +0.32 + 0.04 \lg [UO_2OH^+] - 0.02$ pH	(36)
	$U_4O_9 + 7H_2O \rightleftarrows 4HUO_4^- + 10H^+ + 6\bar{e}$	+150.4	$Eh = +1.09 + 0.04 \lg [HUO_4^-] - 0.1$ pH	(37)
	$U_4O_9 + 14H^+ + 2\bar{e} \rightleftarrows 4UOH^{3+} + 5H_2O$	−33.4	$Eh = +0.72 - 0.12 \lg [UOH^{3+}] - 0.41$ pH	(38)
U_3O_7	$U_3O_7 + 2H^+ \rightleftarrows 3UO_2^{2+} + H_2O + 4\bar{e}$	+8.1	$Eh = +0.09 + 0.04 \lg [UO_2^{2+}] + 0.03$ pH	(39)
	$U_3O_7 + 2H_2O \rightleftarrows 3UO_2OH^+ + H^+ + 4\bar{e}$	+24.6	$Eh = +0.27 + 0.04 \lg [UO_2OH^+] - 0.01$ pH	(40)
	$U_3O_7 + 5H_2O \rightleftarrows 3HUO_4^- + 7H^+ + 4\bar{e}$	+104.6	$Eh = +1.13 + 0.04 \lg [HUO_4^-] - 0.1$ pH	(41)
	$U_3O_7 + 11H^+ + 2\bar{e} \rightleftarrows 3UOH^{3+} + 4H_2O$	−33.3	$Eh = +0.72 - 0.09 \lg [UOH^{3+}] - 0.32$ pH	(42)
U_3O_8	$U_3O_8 + 4H^+ \rightleftarrows 3UO_2^{2+} + 2H_2O + 2\bar{e}$	−17.1	$Eh = -0.37 + 0.09 \lg [UO_2^{2+}] + 0.12$ pH	(43)
	$U_3O_8 + H_2O + H^+ \rightleftarrows 3UO_2OH^+ + 2\bar{e}$	−0.6	$Eh = -0.01 + 0.09 \lg [UO_2OH^+] + 0.03$ pH	(44)
	$U_3O_8 + 4H_2O \rightleftarrows 3HUO_4^- + 5H^+ + 2\bar{e}$	+79.5	$Eh = +1.71 + 0.09 \lg [HUO_4^-] - 0.15$ pH	(45)
	$U_3O_8 + 13H^+ + 4\bar{e} \rightleftarrows 3UOH^{3+} + 5H_2O$	−58.4	$Eh = +0.64 - 0.04 \lg [UOH^{3+}] - 0.19$ pH	(46)
$UO_3 \cdot 2H_2O$	$UO_3 \cdot 2H_2O + 2H^+ \rightleftarrows UO_2^{2+} + 3H_2O$	−7.7	$pH = +2.81 - 0.5 \lg [UO_2^{2+}]$	(47)
	$UO_3 \cdot 2H_2O + H^+ \rightleftarrows UO_2OH^+ + 2H_2O$	−2.2	$pH = +1.6 - \lg [UO_2OH^+]$	(48)
	$UO_3 \cdot 2H_2O \rightleftarrows HUO_4^- + H_2O + H^+$	+24.5	$pH = +17.9 + \lg [HUO_4^-]$	(49)

Compounds of Hexavalent Uranium in aqueous solutions form three stable ions UO_2^{2+}, UO_2OH^+, and HUO_4^-; equilibrium between any pair of these ions is governed by reactions (25) - (27) of Table 3. The form in which U(VI) is present in solution is again governed only by pH (in strongly acid solutions the UO_2^{2+} ion is stable, in weakly acid or neutral solutions the UO_2OH^+ ion, in alkaline solutions the HUO_4^- ion).

The boundaries between the U(IV) and U(VI) ionic stability fields are governed by redox reactions (28) - (30) (Table 3) and depend on both pH and Eh.

In the general case, in acid solutions with pH< 4 uranium is present as UO_2^{2+}, UOH^{3+}, and U^{4+}, the two latter ions being stable only at fairly low Eh. In markedly alkaline media uranium is present in solutions as HUO_4^-, in neutral, weakly acid or weakly alkaline media primarily as UO_2OH^+, UOH^{3+}, and in a few cases as UO_2^{2+}.

The relationship between uranium oxides and ions is established from thermodynamic studies of the corresponding redox reactions. Table 4 gives the results of calculations, together with equations relating Eh with pH and ionic activity. Figure 2 gives diagrams of the relations between thermodynamically stable uranium ions present in equilibrium with $UO_3 \cdot xH_2O$ and other uranium oxides at a given overall ionic activity of the uranium in solution. Garrels [3] gives a detailed examination of the method used for constructing the diagrams: The difference between our diagrams and the conventional one is that in Fig. 2 several diagrams for each uranium oxide are combined in the same plane; in addition to the stability diagram of stable UO_2, this figure gives diagrams reflecting the interelations between variable-composition uranium oxides metastable in water, on the one hand, and stable $UO_3 \cdot xH_2O$ and ions, on the other.

On the diagrams the boundaries between the stability fields of ions with like charges remain unchanged, but the boundaries between the stability fields of ions with different charges and those of oxides and ions vary with the degree of oxidation of the uraninite. The stability field of the hydroxide $UO_3 \cdot xH_2O$ also varies regularly with the UO_3/UO_2 ratio in the anhydrous oxide present in association with the hydroxide.

On the boundaries between the stability fields of any two ions, their activities are equal. Within the stability field of an ion its activity increases with a corresponding decrease in the activities of the

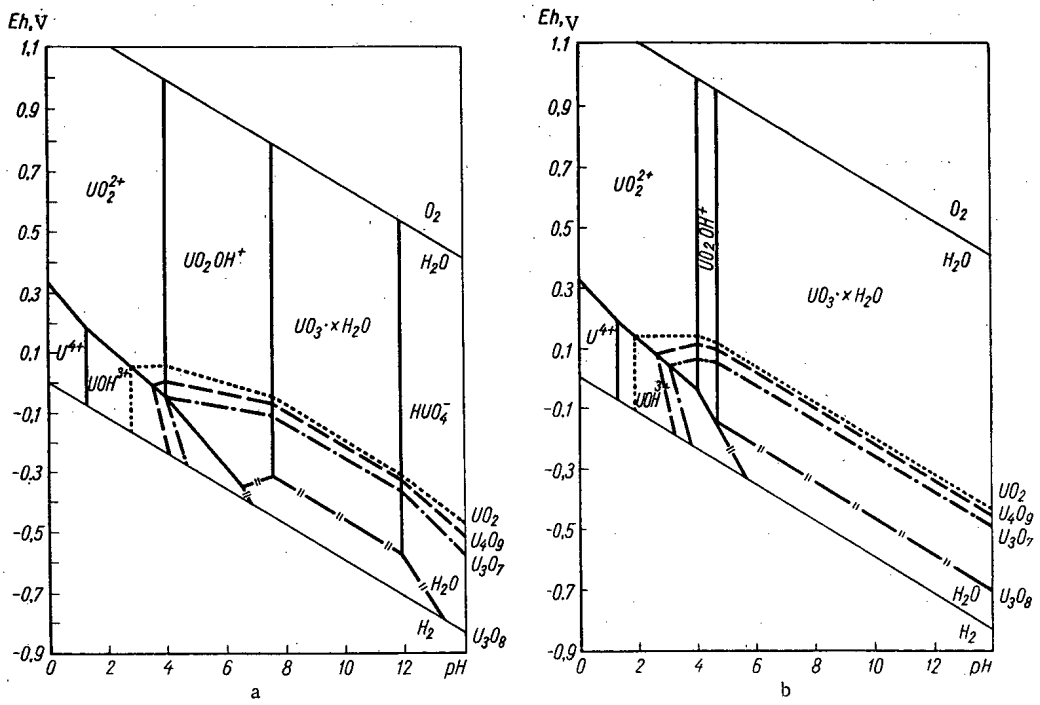

Fig. 2. Stability of uranium compounds in water versus pH and Eh; (a) total ionic activity of uranium 10^{-6}; t = 25°C; P = 1 atm; (b) total ionic activity of uranium 10^{-3}, t = 25°C; P = 1 atm.

neighboring ions, but the overall ionic activity remains constant ($\Sigma U = 10^{-6}$ g·ion/liter and $\Sigma U = 10^{-3}$ g·ion/liter in Fig. 2a, 2b). Within the stability fields of the solid phases the overall ionic activity decreases.

From these diagrams we can assess the conditions of coexistence of uraninites, oxidized to varying degrees, with hydroxides of the $UO_3 \cdot xH_2O$ type and ions. The stability fields of anhydrous uranium oxides decrease regularly with increasing oxygen coefficient. Therefore, the higher the degree of oxidation of uraninite, the more stable will it be in the supergenesis zone and the more readily will it go into solution or be replaced by hydroxides of the type $UO_3 \cdot xH_2O$.

SOLUBILITIES OF URANINITES OF VARIABLE COMPOSITON

In calculating the solubilities of anhydrous uranium oxides we started from the assumption that theoretically uranium oxide with a given UO_3/UO_2 ratio may be in equilibrium with all the thermodynamically stable ions in the solution. By constructing a system of equations of reactions between the solid phase and ions and of reactions between individual ions, we can determine the concentration (equal, to a first approximation, to the activity) of each ion in the solution, and then find the overall ionic solubility by adding these up. In this connection a necessary limiting condition is the absence of redox reactions during the process of solution, i.e. the U^{4+}/U^{6+} ratio in the solid phase and in the solution must remain constant.

The calculations can be demonstrated by determining the solubility of U_4O_9. We construct a system of equations including the reaction of the oxide with one of the ions and the interionic reactions in the solution; we then calculate from thermodynamic data the equilibrium constants of the reactions and find the equations relating the ionic activities (concentrations) and pH:

$$U_4O_9 + 10H^+ \rightleftarrows UO_2OH^+ + 3UOH^{3+} + 3H_2O, \Delta Z = -14.2,\ \lg K_p = 10.4,\ 3\lg[UOH^{3+}] + \lg[UO_2OH^+] = 10.4 - 10\,\mathrm{pH};$$

$$UO_2^{2+} + H_2O \rightleftarrows UO_2OH^+ + H^+,\ \Delta Z = +5.5,\ \lg K_p = -4.0,\ \lg[UO_2OH^+] - \lg[UO_2^{2+}] = -4 + \mathrm{pH};$$

$$U^{4+} + H_2O \rightleftarrows UOH^{3+} + H^+, \Delta Z = +1.7,\ \lg K_p = -1.24,\ \lg[UOH^{3+}] - \lg[U^{4+}] = -1.24 + \mathrm{pH};$$

$$UO_2OH^+ + H_2O \rightleftarrows HUO_4^- + 2H^+, \Delta Z = +26.1,\ \lg K_p = -19.57,\ \lg[HUO_4^-] - \lg[UO_2OH^+] = -19.57 + 2\,\mathrm{pH}.$$

To solve this system of equations with five unknowns we derive an additional equation starting from the assumption that the ratio of the overall U(IV) ionic concentration to the overall U(VI) ionic concentration in the solution is equal to the UO_2/UO_3 ratio in the initial oxide. For U_4O_9

$$\frac{[U^{4+}]+[UOH^{3+}]}{[UO_2^{2+}]+[UO_2OH^+]+[HUO_4^-]}=3.$$

Solving the system of five equations by substitution at a given pH, we find the concentrations (in g·ion/liter) of all ions in equilibrium with U_4O_9 in the aqueous solution at pH 2: $[U^{4+}]=2{,}77\cdot10^{-3}$; $[UOH^{3+}]=1.59\cdot10^{-2}$; $[UO_2^{2+}]=5.18\cdot10^{-3}$; $[UO_2OH^+]=5.18\cdot10^{-5}$; $[HUO_4^-]=1.67\cdot10^{-20}$. From these data we can easily calculate the equilibrium concentration of uranium at pH 2 ($2.4\cdot10^{-2}$ g·ion/liter).

By a similar procedure we calculate the concentrations of the individual ions and the overall uranium concentration in the solution at other pH values. Figure 3 gives the concentrations of all stable ions in equilibrium with U_4O_9.

Figure 4 plots the ionic solubilites of uranium oxides of varying degrees of oxidation versus solution pH. For solutions with pH<4 the solubility curves are approximate and illustrate only the overall pattern; they cannot be used for a quantitative estimate of the solubility because the errors of the thermodynamic method of calculation at dissolved uranium concentrations $> 10^{-2} - 10^{-3}$ g·ion/liter are too great.

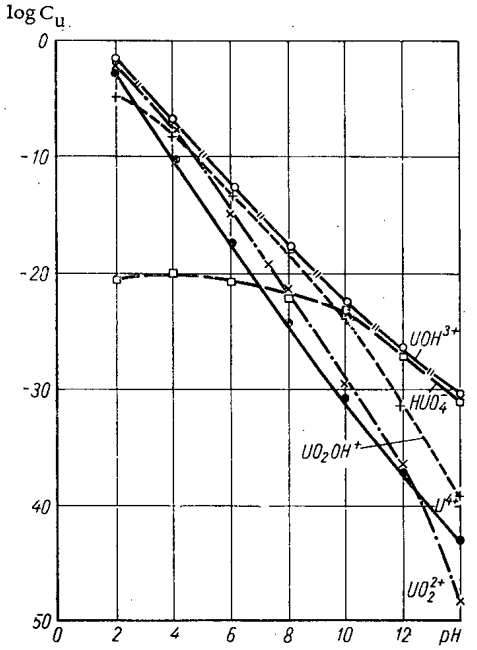

Fig. 3. Ionic solubility of U_4O_9 in water at different pH.

From these graphs it is clearly seen that uraninite solubility increases with the degree of oxidation. In this connection the relation between the solubility of UO_2, U_4O_9, and U_3O_7 and pH is almost linear, and the solubility falls markedly with decreasing acidity (from $10^{-2}-10^{-4}$ at pH 2 to $10^{-24}-10^{-40}$ at pH 14). The solubilities of oxides with higher oxygen coefficients decrease far less with increasing pH. Thus the solubility of U_3O_8 decreases from 10^{-2} at pH 4 to 10^{-13} at pH 14, while with increasing pH the solubility of $UO_3\cdot xH_2O$ first decreases by approximately eight orders of magnitude and then increases by four orders of magnitude in alkaline solutions.

For natural supergene water, with medium pH values, the graph plotting uraninite solubility (at fixed pH) versus UO_3/UO_2 ratio is virtually linear (Fig. 5).

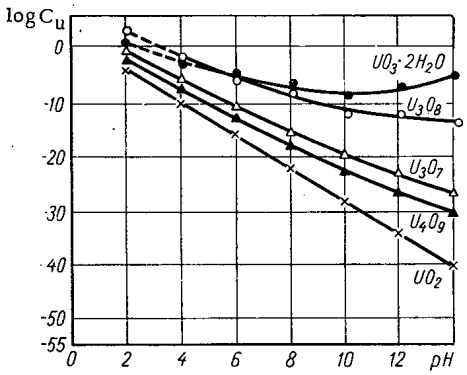

Fig. 4. Ionic solubilities of uranium oxides versus pH of aqueous solutions.

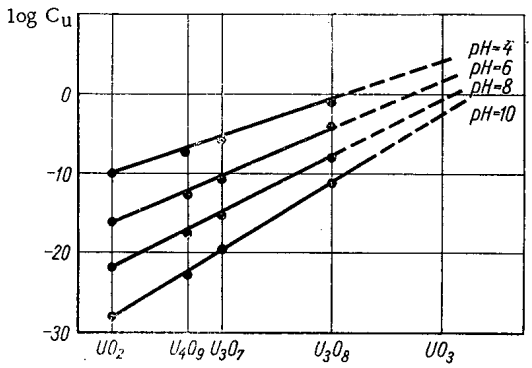

Fig. 5. Ionic solubilites of uranium oxides versus degree of oxidation at fixed pH.

SUMMARY

1. The authors have determined from thermodynamic data the relation between the stabilities of anhydrous uranium oxides of variable composition and the volatility of oxygen (f_{O_2}) at 25°C.

2. It has been found that uranium oxides of variable composition (U_4O_9—U_3O_8) are unstable in liquid water in absence of redox reactions, and may undergo disproportionation to $UO_2 + UO_3 \cdot xH_2O$. According to a hypothesis suggested by the authors, this process is very slow under supergene conditions, and metastable uraninites are kinetically stable.

3. A relation has been established between the stabilities of metastable uranium oxides and the UO_3/UO_2 ratio in supergene conditions: oxide stability decreases with increasing oxygen coefficient. In natural conditions oxidized uraninites must be converted to more stable hydroxides of the $UO_3 \cdot xH_2O$ type.

4. In natural supergene water, of which the pH is in the range 4-8, in absence of complex-formers uranium is present primarily as UOH^{3+} and UO_2OH^+; U^{4+} and UO_2^{2+} play lesser roles in the transfer of uranium.

5. The solubilities of uranium oxides increase with the oxygen coefficient. The relation between solubility and pH differs for the different compounds: the solubilities of oxides with low oxygen coefficients decrease markedly with increasing pH; at high degrees of oxidation this fall is less sharp; in the case of $UO_3 \cdot xH_2O$ the solubility first decreases (minimum solubility is reached at pH 10) and then increases with a further increase in alkalinity.

LITERATURE CITED

1. M. Pourbaix, Thermodynamics of Dilute Solutions. Edward Arnold and Co. London (1949).
2. R. Garrels, Amer. Mineralogist, 40, 11-12, 1004 (1955).
3. R. Garrels, Mineral Equilibria at Low Temperature and Pressure. Moscow, IL [Russian translation] (1962).
4. P. Hostetler, and R. Garrels, Econ. Geol., 57, 2, 157 (1962).
5. M. V. Soboleva and I. A. Pudovkina, Uranium Minerals. Reference Book. Moscow, Gosgeoltekhizdat (1957).
6. Minerals, Reference Book (edited by F. V. Chukhrov and E. M. Bonshtedt-Kupletskaya. Vol. 2, No. 2. Moscow, "Nauka" (1965).
7. E. Westrum, JR. and F. Gronvold, Thermodynamics of Nuclear Materials. Proceedings of the symposium in Vienna (1962). Vienna, IAEA, p. 3 (1962).
8. E. V. Rozhkova and M. B. Serebryakova, Byulleten' nauchno-tekhn. inf., VIMS, ONTI, No. 3, Moscow, Gosgeoltekhizdat, p. 69 (1958).
9. S. A. Brusilovskii, Trudy Inst. geol. rudn. mestor., petr., miner. i geokhimii AN SSSR. No. 42, 58 (1960).
10. V. V. Shcherbina and G. B. Naumov, Moscow, Izd. AN SSSR, p. 5 (1963).
11. G. A. Krestov, Radiokhimiya, 5, 258 (1963).
12. F. Rossini et al., Nat. Bur. Standards Circ., 500, 1 (1952).
13. G. Seaborg and D. Katz, Chemistry of the Actinide Elements [Russian translation], Moscow, Atomizdat (1960).
14. W. Latimer, The Oxidation States of the Elements and their Potentials in Aqueous Solutions. N. Y. — Hall. Inc. (1952).
15. V. M. Vdovenko, Chemistry of Uranium and the Transuranium Elements, Moscow-Leningrad. Izd. AN SSSR (1960).
16. C. Christ and J. Claric, Amer. Mineralogist, 45, 1026 (1960).
17. L. Darken and R. Gurry, J. Amer. Chem. Soc., 67, 1398 (1945).
18. L. S. Evseeva and A. I. Perel'man, The Geochemistry of Uranium in the Supergenesis Zone. Moscow, Atomizdat (1962).
19. A. I. Germanov, In: Principal Features of the Geochemistry of Uranium. Moscow, Izd. AN SSSR, p. 290 (1963).
20. V. V. Shcherbina, In: Principal Features of the Geochemistry of Uranium, Moscow, Izd. AN SSSR, p. 220 (1963).
21. G. Phair, and H. Levine, Econ. Geol., 48, 358 (1953).
22. R. Berman, Amer. Mineralogist, 42, 705 (1957).
23. F. Nelson and K. Kraus, J. Amer. Chem. Soc., 73, 2157 (1951).

RADIATION AND RADIATION SAFETY PICTURE AT THE SITE OF THE NOVO-VORONEZH NUCLEAR POWER PLANT

A. M. Petros'yants

UDC 621.039.583

Nuclear electric power generating plants are in operation in 12 countries throughout the world (USSR, USA, Britain, France, Italy, Japan, East Germany, et al.). Data as of January 1, 1966 indicate the total power generated by these nuclear plants to be 5.9 million kW worldwide, a figure including 1.1 million kW in the USSR. As of January 1, 1967, the total installed electric power capacity of nuclear electric power generating plants will appproach 9.5 million kW, i. e., an increase of 61% in the course of one single year. Predictions for 1970, published in several countries, place the total nuclear power plant output at 24 – 25 million kW by that time, surpassing the January 1, 1966 level by over four times.

This rapid growth in the number of nuclear power plants in regular power production has caused some alarm in certain sectors of the population, because of the hazards associated with radioactive materials formed in the operation of large-scale nuclear reactors.

It is well known that radioactive gases and aerosols are vented through stacks to the atmosphere after undergoing special decontamination procedures, while liquid and solid process wastes contaminated by radioactive pollutants are shunted off to special burial pits for long-term storage.

The radiation safety picture of nuclear powerplants, as it affects the local population, vegetation, soil, and watersheds, is clearly seen in the example of long-term operation of the large industrial-scale Novo-Voronezh nuclear electric power plant (NVNEPP is what follows) in the Central Chernozem zone of the European USSR. The Novo-Voronezh nuclear power plant has a rated capacity of 210 thousand kW, and is based on a single water-cooled water-moderated reactor which was commissioned on September 30, 1964. By September 25, 1966, this plant had fed 2 billion 165 million kWh power into the national power grid (the date refers to the second reloading shutdown). NVNEPP has been brought up to design power by December 1964, and the power output had been pushed to 240 thousand kW by January 1966.

Disposal of effluent water contaminated by radioactive pollutants into open reservoirs, the Don river in particular, was completely rejected as an alternative in the plant drawn up for NVNEPP. Special clean-up installations were built on the power station site and repeated use of decontaminated waters for power plant production needs was planned for. Air in the ventilation system is specially purified to remove radioactive materials, and is vented to the atmosphere through a stack 120 m high. The system designed to trap radioactive vapors and aerosols includes gasholders for hold-up and decay of short-lived radioisotopes.

Hydraulically insulated burial pits for disposal of radioactive waste solids and liquids have been built which keep radioactive materials out of the ground water in the area. Several inspection holes have been drilled around the burial grounds, to detect any leakthroughs and to aid in measures to cope with them.

A specially organized radiation safety division at NVNEPP monitors radiation safety in the power station, and readings of all dosimetric and radiometric instruments, sensors for which are positioned in various monitored rooms and locations around the plant, are entered in a special log book twice each working shift.

The radiation level of the ventilated air stream laden with radioactive contaminants is continuously monitored at the station. A portion of the air is continuously pumped from the base of the stack through a DZ-20 chamber hooked up to a Kaktus instrument for this purpose at a rate of 60 liters/min. Results of the measurements are recorded in the division's special log book. Samples are taken at six points

Translated from Atomnaya Énergiya, Vol. 21, No. 6, pp. 492-496, December, 1966. Original article submitted September 7, 1966.

TABLE 1. Radioactive Fallout Density (10^{-3} Ci/km^2. day) Based on Sedimentation Methods

Date	Distance from NVNEPP stack, km				
	0.5	2	4-6	6-12	40
1964					
January	0.15	-	-	-	-
February	0.5	-	-	-	-
March	1.4	-	-	-	-
April	3.0	-	-	-	-
May	5.0	-	-	-	-
June	1.4	-	-	-	-
July	5.1	3.5	-	-	-
August	1.4	1.1	-	-	-
September*	1.0	0.7	-	-	-
October	0.5	0.4	-	-	-
November	0.5	0.4	0.33	0.36	0.28
December	0.2	0.3	0.30	0.29	0.26
1965					
January	0.04	0.04	0.05	0.05	0.07
February	0.04	0.07	0.05	0.04	0.11
March	0.09	0.07	0.08	0.10	0.15
April	0.16	0.17	0.20	0.21	0.21
May	0.21	0.10	0.20	0.19	0.21
June	0.85	0.60	0.60	0.58	0.60
July	0.19	0.20	0.30	0.26	0.17
August	0.29	0.13	0.16	0.19	0.08
September	0.08	0.07	0.06	0.05	0.03
October	0.04	0.03	0.03	0.03	0.11
November	0.08	0.03	0.02	0.02	0.07
December	0.08	0.06	0.06	0.05	0.06
1966					
January	0.06	0.04	0.07	0.05	0.07
February	0.03	0.03	0.03	0.03	0.04
March	0.05	0.05	0.04	0.06	0.02
April	0.07	0.03	0.05	0.05	0.05
September	0.04	0.04	0.03	0.03	0.04
October	0.05	0.03	0.02	0.03	0.06

*The Novo-Voronezh power station went on the line on September 30, 1964.

from the ventilation duct (exhaust lines) to determine the daily outflow of long-lived aerosols. Fifty cubic meters of air are pumped daily through FP fabric filters. The total β-activity of the samples is determined on a B-2 arrangement using a SI-2B counter, which is housed in a lead castle with walls 5 cm thick. After β-activity has been measured, the sample is subjected to γ-ray spectrometric analysis to ascertain the isotope makeup of the aerosols; a NaI (Tl) crystal 70 mm by 70 mm and a AI-100 (Raduga [Rainbow]) analyzer are used in this work.

The staff of NVNEPP now includes a special external dosimetry service whose main assignment is persistent monitoring of the radiation safety situation over an area 40 km in radius around the power station. (With the future large-scale building of nuclear power stations, such services will apparently become combined into a single state agency empowered to inspect and monitor the radiation environment in the nation as a whole.) Plant workers assigned to this service measure the fallout density from the air (by sedimentation techniques), the concentration of radioactive aerosols in atmospheric air (by aspiration techniques) the content of radioactive materials in the soil and in vegetation, in bottom deposits and in seaweed, in the water of the Don river (which is used at NVNEPP to cool the secondary-loop equipment), and in the water of open reservoirs. They also monitor γ-radiation over the locality.

Thirty-three permanent dosimetric posts for sampling, equipped with six pump rigs and 25 planchet-cuvette stands, are located at points on the NVNEPP site and surrounding areas within a 40-km radius, as aids in solving these problems.

The positioning of these posts relative to the NVNEPP stack is as follows. One pump rig surrounded by eight planchet-cuvette stands is placed 500 m from the stack. Eight planchet-cuvette stands are placed peripherally 2 km from the stack. Three pump rigs and eight planchet-cuvette stands are placed peripherally 4 to 6 km from the stack. One pump rig and eight planchet-cuvette stands are placed 6 to 12 km from the stack peripherally. One pump rig with a planchet-cuvette stand is situated 40 km from the stack. The external dosimetry service takes samples of soil and vegetation from all planchet-cuvette locations around the plant.

Water samples are taken at the following four points on the Don downstream from the plant: 100 m upstream of the main water intake header, at the discharge header, and at points 100 m and 6 km downstream of the discharge header.

Tiss type instruments with ÉPPV-60 automatic recorders are located at points where aspiration devices are set up, to aid in constant logging of γ-radiation on the terrain. The activity of samples taken is measured, after proper processing, in a special radiometric laboratory located outside the NVNEPP premises and equipped with a low-background device (UMF type), an AI-100 analyzer, and other instruments. The external dosimetry service uses a truck-mounted radiometric laboratory to take samples and analyze them at any other points in the region to be covered.

The industrial public health laboratory serving a public health epidemiological station under the medical and public health section of the Ministry of Public Health of the USSR also conducts sampling and monitoring analyses to check the status of objects in the external environment of the NVNEPP power station. Below we cite data on the radiation situation in the NVNEPP district as obtained and processed by the staff of this station. All radiation measurements were begun 9 months prior to the commissioning of the NVNEPP reactor, in order to provide an objective assessment of the possible effect of NVNEPP on the external environment.

Table 1 presents data on radioactive fallout density measured by sedimentation techniques. The table shows that concentrations of radioactive fallout at the remotest control point (40 km from the vent stack) did not differ from concentrations measured at all other points in the zone monitored, within the limits of accuracy of the measurements. Comparison of 1964 data prior to full-power operation of NVNEPP and 1965-1966 data, with the station delivering 210 – 240 MW to the grid, shows that radioactive fallout density did not increase in the latter period, remaining at the level of radioactive fallout existing beforehand. Radioactive fallout from atmospheric air which is at all points monitored in the environs of the NVNEPP site is therefore due solely to global fallout.

TABLE 2. Concentration of Radioactive Aerosols (10^{-16} Ci/liter) in the NVNEPP District, Measured by Aspiration Techniques

Date	Distance from NVNEPP stack, km		
	0.5	5	40
1964			
Prior to start of power station	-	0.35-2.16	-
IV quarter	2.1	0.86-2.08	1.6
1965			
I quarter	1.3	1.5	1.0
II quarter	3.0	3.5	2.2
III quarter	1.5	1.6	1.5
IV quarter	0.5	0.5	0.4
1966			
January	0.61	0.51	0.18
February	0.55	0.35	0.61
March	0.80	0.53	0.34
April	1.13	0.84	0.34
May	1.14	0.88	0.78
October	1.40	0.30	0.47

TABLE 3. Content of Radioactive Pollutants in Soil (10^{-8} Ci/kg dry weight soil) in NVEPP Region

Date	Distance from NVNEPP stack, km				
	0.5	2	4–6	6–12	40
1964	2.5	3.6	3.0	3.7	5.7
1965	2.2	2.4	2.3	3.2	2.7
1966 (May)	1.6	2.1	1.6	1.9	2.0
1966 (July)	1.8	1.0	1.1	1.8	0.6

TABLE 4. Content of Radioactive Pollutants in Vegetation (10^{-8} Ci/kg Weight of Vegetation) in NVNEPP Region

Date	Distance from NVNEPP stack, km				
	0.5	2	4–6	6–12	40
1964	3.1	2.5	2.7	2.8	5.7
1965	1.8	1.5	1.7	1.8	1.9
1966 (April)	1.2	0.6	0.8	0.7	0.9
1966 (August)	1.0	1.8	0.9	1.3	1.1

The power station in operation consequently exerts no harmful effect of any kind on the surrounding locality as far as radiation environmental factors are concerned.

Table 2 presents data on concentrations of radioactive aerosols in the NVNEPP district, as measured by aspiration techniques.

The tabulated data show that concentration of radioactive aerosols in atmospheric air remain at the background level and are due solely to global fallout. The 1964-1966 concentrations of radioactive aerosols in the atmospheric air over a 40-km radius around NVNEPP remain practically constant, with no increase in amount over the previous period when no power station was in operation. Similar inferences can be drawn from Tables 3 and 4, where data on the content of radioactive materials in soil and vegetation in the NVNEPP site and surroundings are tabulated.

In 1965, the industrial public health laboratory of the public health and epidemiological station of the USSR Ministry of Public Health conducted monitoring tests on the content of radioactive pollutants in agricultural crop plants raised in the zone of the NVNEPP site area protected by public health measures. It was found that the total β-activity of radioactive materials amounted to anywhere from $9.9 \cdot 10^{-10}$ to $1.7 \cdot 10^{-8}$ Ci/kg (weight before drying). Comparison of 1964, 1965, and 1966 data shows that the content of radioactive pollutants both in soil and in vegetation in the NVNEPP area and surroundings did not increase over the period prior to commissioning of the power station, and are even found to be on the level of background values.

Data on the content of radioactive pollutants in the waters of the Don river are of particular interest (Table 5). Here the results of monitoring analysis of samples of water taken from the cut-off of Don river and measured by the industrial public health laboratory of the public health and epidemiological station of the USSR Ministry of Public Health indicate that the 1965 content of radioactive contaminants fluctuated between $1.75 \cdot 10^{-12}$ and $0.91 \cdot 10^{-11}$ Ci/liter, while the 1966 content fluctuated between $7.45 \cdot 10^{-12}$ and $1.52 \cdot 10^{-11}$ Ci/liter. Measurements conducted by the Institute of Biophysics of the USSR Ministry of Public Health put the 1961 concentration of β-active substances in the waters of the Don river at $9.0 \cdot 10^{-12}$ Ci/liter. Analysis of these data reveals that the content of radioactive pollutants in the Don waters in the vicinity of the NVNEPP site did not increase over the prereactor period, and are on the same level as background. The same inference can be drawn from measurements of the amount of β-active substances present in Don bottom sediments (Table 6).

TABLE 5. Content of Radioactive Contaminants in Waters of the Don River (10^{-12} Ci/liter Water)

Date	Sampling point			
	upstream of main intake header	at discharge header	downstream of discharge header	6 km downstream of discharge header, in Don river
1964 (before power station went on line)	8.0	8.7	14.0	8.0
1964 (December)	5.8	4.8	7.3	13.0
1965 (first half year)	7.5	10.0	20.0	8.0
1965 (second half year) . .	9.0	10.4	6.4	8.0
1966 (May)	9.5	10.0	8.0	8.1
1966 (October)	5.6	20.0	6.4	3.4

TABLE 6. Amount of β-Active Pollutants in Bottom Deposits of the River Don (10^{-8} Ci/kg)

Sampling point	1964*		1965		1966, 1st half year
	1st half year	July-September	1st half year	2nd half year	
100 m upstream of discharge conduit	3.7	1.2	2.3	1.4	2.2
At discharge conduit	Not monitored, since NVNEPP was not operative at that time		3.1	2.2	2.3
100 m downstream of discharge conduit	3.7	1.4	1.5	1.2	1.05
Lake at the town of Novo-Voronezh	Not monitored, for same reason as above		1.0	0.8	0.6

*Institute of Biophysics 1961 data indicate the amount of β-active materials present in the Don river came to $3.5 \cdot 10^{-8}$ Ci/kg.

The results of all these measurements provide incontrovertible evidence that the concentration of radioactive pollutants in the air, water soil, vegetation, and other objects of the external environment remained at completely safe background levels through the period of operation of the Novo-Voronezh neclear power station (1964 – 1966).

These facts and figures are convincing evidence that nuclear electric power generating stations are no more of a hazard to the public and environment that any other industrial installation, when the proper radiation safety measures that have been carefully worked out are observed. The extended experience of the Soviet nuclear industry and power industry, exemplified in particular by the operating experience at NVNEPP, shows that when these rules and regulations are duly observed, the use of nuclear reactors at electric power stations to generate electric power is perfectly safe with respect to radiation, at any points where the station may be sited, and even on such major waterways of the country as the Don river.

ABSTRACTS

ANGULAR DISTRIBUTION OF MULTIPLY SCATTERED BETA-RADIATION

L. M. Boyarshinov

UDC 539.124:539.121.72:543.52

The angular distribution of multiply reflected radiation generated when the source is placed laterally in the spacing between two slabs aligned parallel (Fig. 1) was studied at different distances p between slabs. A BFL-25 end-window counter was used in the measurements.

When the distance between slabs is small, the angular distribution of multiply reflected radiation peaks twice at angles α of 120° and 90° to the surfaces of the reflectors. When the spacing between slabs is greater than 3.0 cm, there is only one peak, at α=90° (Fig. 2). An explanation is given.

It is proved that when an annular source is employed at any spacing between slabs, radiation emerging normal to the surface of the second reflector is recorded preferentially. This conclusion must be taken into account in the design of instruments for radiometric analysis of mixtures and compounds by measuring the intensity of multiply reflected radiation.

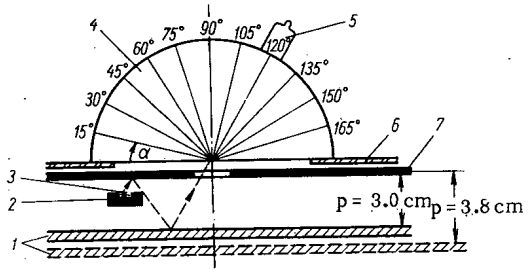

Fig. 1. Experimental arrangement: 1) bottom lead slab; 2) source case; 3) Tl^{204} source; 4) lead hemisphere; 5) BFL-25 end-window counter; 6) shelf supporting lead hemisphere; 7) top lead slab (broken line indicates possible trajectory of electron recorded).

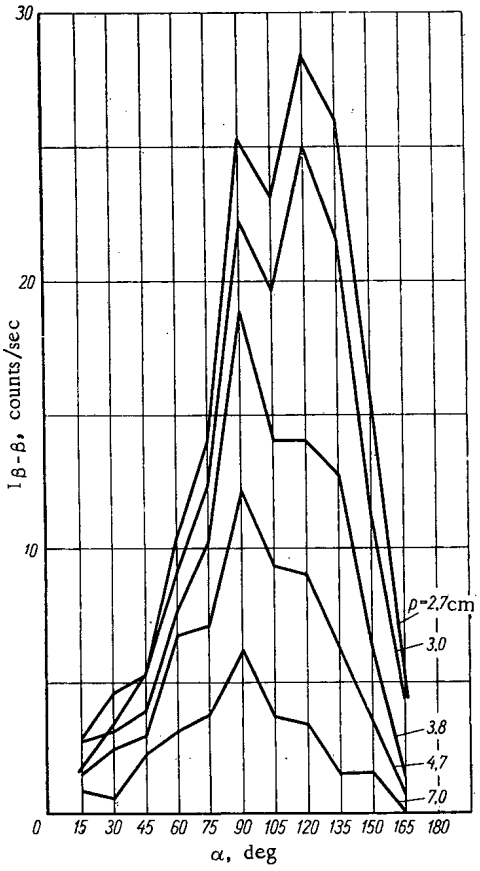

Fig. 2. Angular distribution of intensity of multiply reflected radiation $I_{\beta-\beta}$ as a function of spacing p between slabs.

Translated from Atomnaya Énergiya, Vol. 21, No. 6, p. 497, December, 1966. Original article submitted December 12, 1966.

CALCULATING TEMPERATURE DISTRIBUTION IN FUEL ELEMENTS OF A WATER-COOLED WATER-MODERATED POWER REACTOR

G. V. Sinyutin

UDC 621.039.517.5

An analytical solution is given of the problem of temperature distribution in fuel elements placed in the core of a liquid-cooled reactor, with fuel assemblies consisting of several fuel rods joined by metal inserts. An example of temperature distribution calculations is provided.

The problem reduces to the solution of the heat-conduction equations, one of which is inhomogeneous with boundary conditions of the third kind applicable to two cylinders joined at their end surfaces.

The equations are solved in cylindrical coordinates (r, z) using the following boundary conditions:

equality of temperatures and heat flow values in the plane where the rods are joined (z = 0):

$$T_1(r, 0) = T_2(r, 0), \tag{1}$$

$$\lambda_1 \frac{\partial T_1}{\partial z}(r, 0) = \lambda_2 \frac{\partial T_2}{\partial z}(r, 0); \tag{2}$$

heat-transfer conditions on the rod outer surfaces (r = R):

$$\frac{\partial T_1}{\partial r}(R, z) = -\xi_1 T_1(R, z), \tag{3}$$

$$\frac{\partial T_2}{\partial r}(R, z) = -\xi_2 T_2(R, z). \tag{4}$$

Here T(r, z) is the temperature; λ is the thermal conductivity; $\xi = \alpha/\lambda$; α is the heat-transfer coefficient; the subscript 1 refers to portions of the rod containing uranium (the heat source), subscript 2 refers to portions of the rod containing no heat source.

The principal difficulty in solving the problem is the variable r in Eqs.(1) and (2) and the variable z in Eqs. (3) and (4). But it can be shown that the sum of terms containing z in Eqs.(3) and (4) vanishes. This leads to expressions of the type

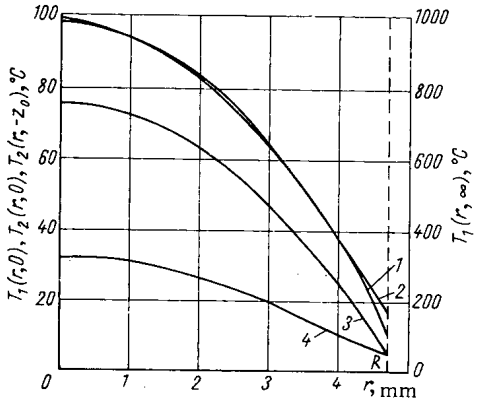

Fig. 1. Radial temperature distribution at various rod cross sections: 1) $T_1(r, z = 0)$; 2) $T_2(r, z = 0)$; 3) $T_1(r, z = \infty)$; 4) $T_2(r, z = -z_0)$.

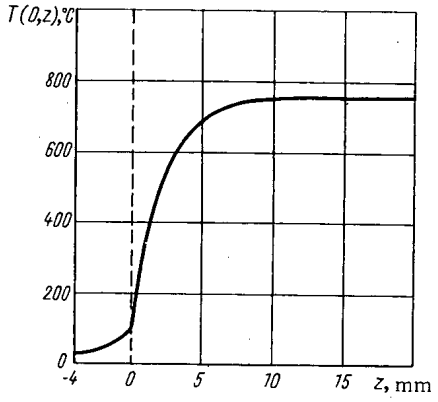

Fig. 2. Axial temperature distribution, UO_2 rod type element with zirconium insert.

Translated from Atomnaya Énergiya, Vol.21, No.6, pp.498-499, December, 1966. Original article submitted December 14, 1965.

$$\eta J_1(\eta R) = \xi J_0(\eta R), \tag{5}$$

where J_0, J_1 are zero-order and first-order Bessel functions of the first kind respectively.

Equations (5) define the infinite spectrum of eigenvalues of the parameters η_1 and η_2: $\eta_1 = \eta_1^i$; $\eta_2 - \eta_2^i$; i = 1, 2, 3 ... (i here is a superscript for notational purposes, not an exponent). The solution is then

$$T_1(r, z) = \sum_{i=1}^{\infty} C_i J_0(\eta_1^i r)\, e^{-\eta_1^i z} + A - \frac{w}{4\lambda_1} r^2; \tag{6}$$

$$T_2(r, z) = \sum_{i=1}^{\infty} D_i J_0(\eta_2^i r)\,[e^{2\eta_2^i z_0} e^{\eta_2^i z} + e^{-\eta_2^i z}], \tag{7}$$

where C_i and D_i are constants; z_0 is half the length of an insert; w is the volume density of heat sources in the uranium; the constant

$$A = \frac{w}{4\lambda_1} R^2 + \frac{w}{2\lambda_1 \xi_1} R.$$

The functions $A - (w/4\lambda_1)r^2$ and $J_0(\eta_2^i r)$ can be expanded in series of Bessel functions with respect to the spectrum η_1^i (Dini series)*.

Now, by substituting $T_1(r, z)$ and $T_2(r, z)$ from Eqs. (6) and (7) into Eqs. (1) and (2), and then replacing these functions by their Dini series expansions, we can find the relationship linking C and D, after some transformations:

$$C_m = \sum_{i=1}^{\infty} D_i \frac{\lambda_2 \eta_2^i}{\lambda_1 \eta_1^m} (1 - e^{2\eta_2^i z_0})\, \gamma_{mi}, \quad m = 1, 2, 3, \ldots, \tag{8}$$

where

$$\gamma_{mi} = \frac{2\,[\eta_2^i J_0(\eta_1^m R) J_1(\eta_2^i R) - \eta_1^m J_0(\eta_2^i R) J_1(\eta_1^m R)]}{R\,[(\eta_2^i)^2 - (\eta_1^m)^2]\,[J_0^2(\eta_1^m R) + J_1^2(\eta_1^m R)]} \tag{9}$$

To determine D_i we obtain an infinite system of inhomogeneous linear algebraic equations with constant coefficients

$$A_m = \sum_{i=1}^{\infty} D_i a_{mi}, \quad m = 1, 2, 3, \ldots, \tag{10}$$

where

$$A_m = \frac{[4A\lambda_1 (\eta_1^m)^2 - w(\eta_1^m R)^2 + 4w]\, J_1(\eta_1^m R) - 2w\eta_1^m R J_0(\eta_1^m R)}{2\lambda_1 (\eta_1^m)^3 R\,[J_0^2(\eta_1^m R) + J_1^2(\eta_1^m R)]}, \tag{11}$$

$$a_{mi} = \gamma_{mi}\left[\left(1 + e^{2\eta_2^i z_0}\right) - \frac{\lambda_2 \eta_2^i}{\lambda_1 \eta_1^m}(1 - e^{2\eta_2^i z_0})\right] \tag{12}$$

By way of illustration, Figs. 1 and 2 give the results of a temperature-distribution calculation in a uranium dioxide fuel element with a zirconium insert. The coolant temperature was assumed zero in the calculations.

* Cf. N. N. Lebedev, Special Functions and Their Uses, Moscow, State tech. lit. press, 1953 [in Russian].

HOW TO MEASURE THE ACTIVE CONCENTRATION OF AEROSOLS OF LONG-LIVED α-ACTIVE ISOTOPES WITH A SCINTILLATION SPECTROMETER

V. P. Grigorov

UDC 543.52:541.182.2/.3

A new variant of a method for measuring the active concentration of aerosols of long-lived α-active isotopes (Pu^{239}, to be specific) without holdup to allow decay of radon and thoron daughters (RaC', ThC, ThC'), is described. α-emission of a sample of aerosol matter is recorded with a scintillation spectrometric probe and a two-channel pulse height analyzer. The compensation channel handles the short-lived isotope portion of the spectrum, to account for short-lived nuclides affecting the counting channel and characterized by the coefficient F.

Aerosol particulate sedimentation methods are evaluated, and a new thin-fiber filtration material, LFS-1, is studied and utilized. A spectrometric α-probe with a CsI(Tl) scintillator was designed and its performance was studied.

Basic factors responsible for systematic errors in measurements are classified: spurious readings (changes in the physicochemical and radiation properties of aerosols, instability of the equipment used, etc.). Analysis of instrumental spectra computed by matrix methods provides determinations of the size of spurious readings and a basis for recommending measuring conditions to minimize these factors. The effect of variations in the activity of ThC and RaC' is eliminated by setting discrimination levels such that the compensation factor F will be unity, independently, for the spectra of these nuclides (Fig. 1). The effect of variations in air dust load is minimized by use of a collimator.

The size of spurious readings due to the total effect of the factors enumerated is $\approx 1 \cdot 10^{-15}$ Ci/liter.

The method proposed has been carefully checked experimentally and has provided a basis for the design of several aerosol radiometers in industrial use.

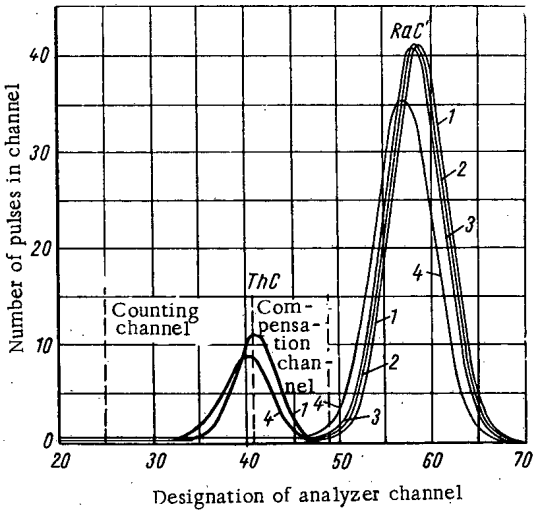

Fig. 1. Calculated spectra of pulse heights (using collimator) at different filter cake thicknesses (mg/cm^2): 1) 0.16; 2) 0.28; 3) 0.4; 5) 0.8. Broken line gives recommended discrimination levels.

Translated from Atomnaya Énergiya, Vol. 21, No. 6, p. 499, December, 1966. Original article submitted May 6, 1966.

AZIMUTHAL DRIFT OF CHARGED PARTICLES IN AN AXIALLY SYMMETRIC MAGNETIC FIELD WITH MIRRORS

V. M. Balebanov and N. N. Semashko

UDC 533.9

From the equations of motion of a charged particle in a mirror trap with a static axisymmetric magnetic field, we can, in the drift approximation, obtain an equation for the angular drift velocity (see, for example, [1]):

$$\dot{\varphi} = \frac{mv^2c}{4eh_0} F(\alpha_0, z), \tag{1}$$

where m is the mass of the particle, e its charge, v the total velocity, c the velocity of light in vacuo, h_0 the intensity of the magnetic field at the point of injection (in the median plane), and $F(\alpha_0, z)$ a function depending on the angle of injection α_0 and the configuration of the magnetic field on the axis of symmetry, h(z). The expression for the azimuthal drift period time taken to drift through an angle 2π) is correspondingly

$$\tau_{dr} = \frac{4\pi e}{c} \cdot \frac{h_0}{E} \cdot \frac{1}{F(\alpha_0, z)} \tag{2}$$

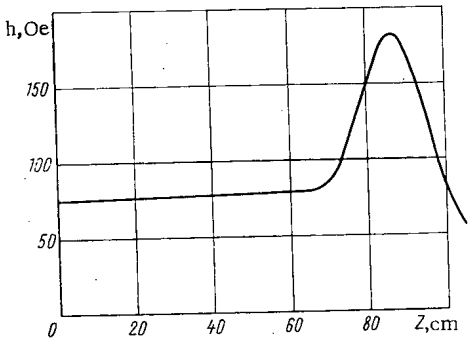

Fig.1. Configuration of magnetic field on axis of apparatus.

(where $E = mv^2/2$ is the total energy of the particle).

For constant magnetic field configuration and given injection angle, (2) implies the well-known relation $\tau_{dr} \sim 1/\rho_0 v$, where $\rho_0 = (mvc/eh_0) \cos \alpha_0$ is the initial value of the Larmor radius. Note that (2) was derived in the drift approximation, and is valid when the adiabaticity parameter $\beta = (\nabla h/h)\rho \ll 1$.

By observing the value of τ_{dr} during several hundreds or thousands of reflections from the magnetic mirrors, we can find the Larmor radius ρ_0 and hence the parameter β at which deviation from drift theory is observed.

For this purpose we studied the drift of electrons in a magnetic field like that of the "Ogra-1" mirror machine [2]

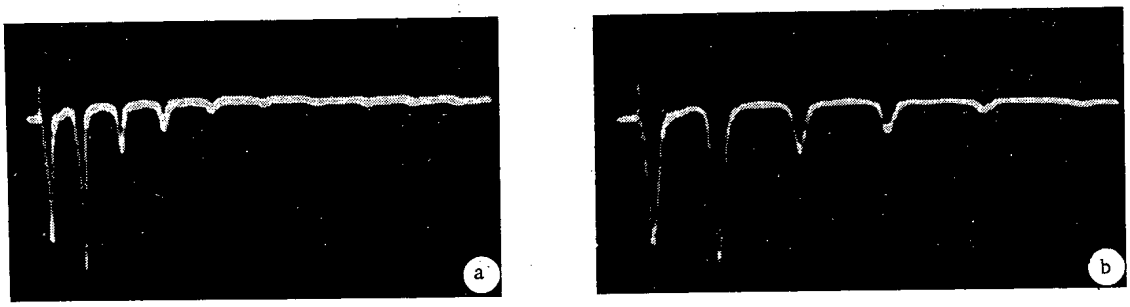

Fig.2. Oscillograms of electron currents at receiving electrode of injector (distance between peaks is equal to time of drift through angle 2π). (a) Scanning duration 50 μsec, ρ_0 = 3 cm; (b) scanning duration 25 μsec, ρ_0 = 4.8 cm.

Translated from Atomnaya Énergiya, Vol.21, No.6, pp.500-501, December, 1966. Original article submitted June 23, 1966.

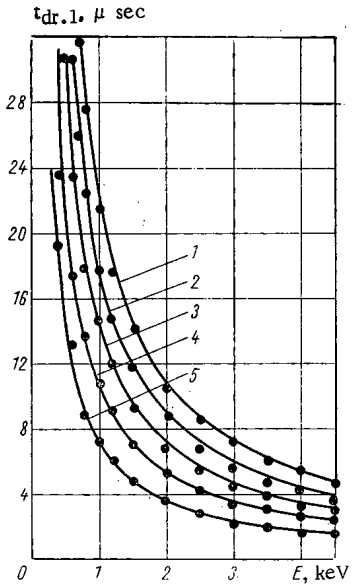

Fig.3. Drift time $\tau_{dr.1}$ versus total energy of electron, E, for various values of h_0 (Oe). [Solid curve is drawn from (2) for $\tau_{dr.1}$ normalized to value $h_0 = 105$ Oe and E = 1 keV ($\rho_0 = 0.95$ cm, $\beta_{max} = 0.038$)]. 1) 105; 2) 87.5; 3) 70; 4) 52.5; 5) 35.

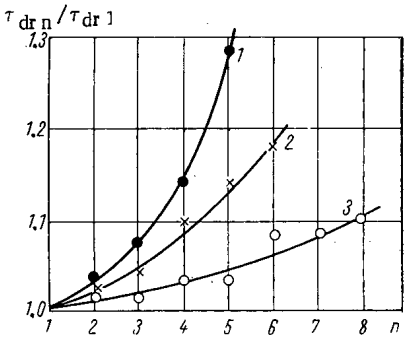

Fig.4. Relative variation of τ_{dr}, versus number of drift revolutions n. 1) $\rho_0 = 6.1$ cm, $\beta_{max} = 0.25$; 2) $\rho_0 = 5.0$ cm, $\beta_{max} = 0.20$; $\rho_0 = 3.1$ cm, $\beta_{max} = 0.12$.

in conditions of optimum positive drift (drift directed towards the direction of the Larmor rotation). The measurements were made with ÉMO-3 apparatus – an electronic model of "Ogra" with scale coefficient 1:7 [3]. The electrons were injected in the central plane of the trap. The angle of injection was 20°; the field configuration remained constant when h_0 was varied, and is shown in Fig.1 for one value of h_0. The method of measuring the azimuthal drift period of the electrons is similar to that described in [4]; it consisted of injecting an electron beam in short pulses (lasting 0.5 μsec) and measuring the duration of their motion in the trap before falling on to the injector. To the frame of the source was fixed a receiving electrode in the form of a hemicyclinder. The time constant of the electrode and measuring circuit was quite small ($RC = 5.10^{-8}$ sec). The signal from the receiving electrode was amplified by an USh-10 amplifier and recorded by a DÉSO-1 oscillograph. In these experiments the energy of the electrons was varied from 0.3 to 4.5 keV, and the magnetic field intensity in the central plane from 35 to 105 Oe, corresponding to initial Larmor radii from $\rho_0 = 0.52$ to 6.1 cm ($\beta_{max} = 0.02$–0.25). The injection radius was 7.2 cm.

Figure 2 shows typical oscillograms, from which we determined the period of azimuthal drift of the electrons. Here the first peak corresponds to electrons incident on the injector after the first reflections from the mirrors (due to the small drift angle of the particles after one reflection in comparision with the angle of "intersection" of the orbit with the injector). The distance between two neighboring peaks on the oscillogram corresponds to the time of drift of the electrons through an angle 2π (the drift period). In these experiments we observed up to 11 peaks. In most cases, τ_{dr} remained constant during all the observed drift periods (except for experiments with large Larmor radii). The errors in the measurement of τ_{dr} were approximately 5%.

Figure 3 plots the drift time $\tau_{dr.1}$, measured from the difference between the first two peaks, versus the total energy of the electrons for various values of h_0 and constant $F(\alpha_0, z)$. It will be seen that the measured values of $\tau_{dr.1}$ corresponding to the first drift rotation through angle 2π agree with (2) over the entire range of measurements.

However, when $\rho_0 > 3$ cm ($\beta_{max} > 0.12$) we observed a gradual increase of τ_{dr} with n (the number of drift revolutions) (Fig.2 b). In this case, the greater ρ_0, the faster did τ_{dr} increase with n (Fig.4). When $\rho_0 = 6.1$ cm ($\beta_{max} = 0.25$), after five drift revolutions (~ 100 reflections from the mirrors) τ_{dr} increased by 30%. This is apparently associated with an increase in the cross-sectional component of the velocity, $v_\perp$, i.e., with an increase in the magnetic moment of an electron.

Thus it follows from our experiments that the drift time of the electrons, when $\rho_0 < 3$ cm ($\beta_{max} < 12\%$), shows satisfactory agreement with drift theory in the first thousand reflection from the mirrors.

However, even with such a relatively small number of vibrations between the mirrors, deviations from drift theory are observed for large Larmor radii ($\rho_0 > 3$ cm, $\beta_{max} > 0.12$).

LITERATURE CITED

1. L. S. Solov'ev, In symposium "Plasma Physics and the Problem of Controlled Thermonuclear Reactions". Vol.III, Moscow, Izd. AN SSSR (1958).
2. I. N. Golovin et al., Usp. fiz. nauk, 73, 685 (1961).
3. V. Balebanov et al., J. Nucl. Energy, Part C., 5, 205 (1963).
4. V. M. Balebanov et al., Atomnaya Énergiya, 15, 4 (1963).

THE 300-MeV ELECTRON SYNCHROTRON OF THE TOMSK POLYTECHNIC INSTITUTE

V. P. Anokhin, A. G. Vlasov, A. A. Vorob'ev,
V. N. Eponeshnikov, I. A. Gabrusenko,
B. N. Kalinin, L. G. Kositsyn, V. A. Kochegurov,
V. N. Kuz'min, G. A. Sipailov, B. A. Solntsev,
V. I. Tolmachev, and I. P. Chuchalin

UDC 621.384.612

In March 1966 a 300-MeV electron synchrotron was put into service at the Nuclear Physics Research Institute of the Tomsk Polytechnic Institute: it was subsequently found convenient to use it for research in nuclear physics.

The work envisaged in this field for the near future falls into two categories: investigation of the cross sections of nuclear photo-effects, and of the photoproduction of pi-mesons from light nuclei.

Figure 1 shows a general view of the equipment. A characteristic feature of the synchrotron is the deep frequency modulation of the accelerating voltage, as the electrons are injected with an energy of 250 keV.

The electromagnet of the synchrotron consists of four quadrants separated by linear gaps of length 0.6 m. The magnetic circuit consists of 24 blocks with C-shaped cross section, with the gap on the outer side. The radius of the orbit in the quadrants is 0.95 m, and the coefficient of decrease of the field is 0.65.

The total weight of steel in the magnet is 14.7 tons, that of copper is 1.5 tons. The synchrotron operates in pulses with recurrence frequency 1 sec^{-1}. The electromagnet is excited by discharge of a

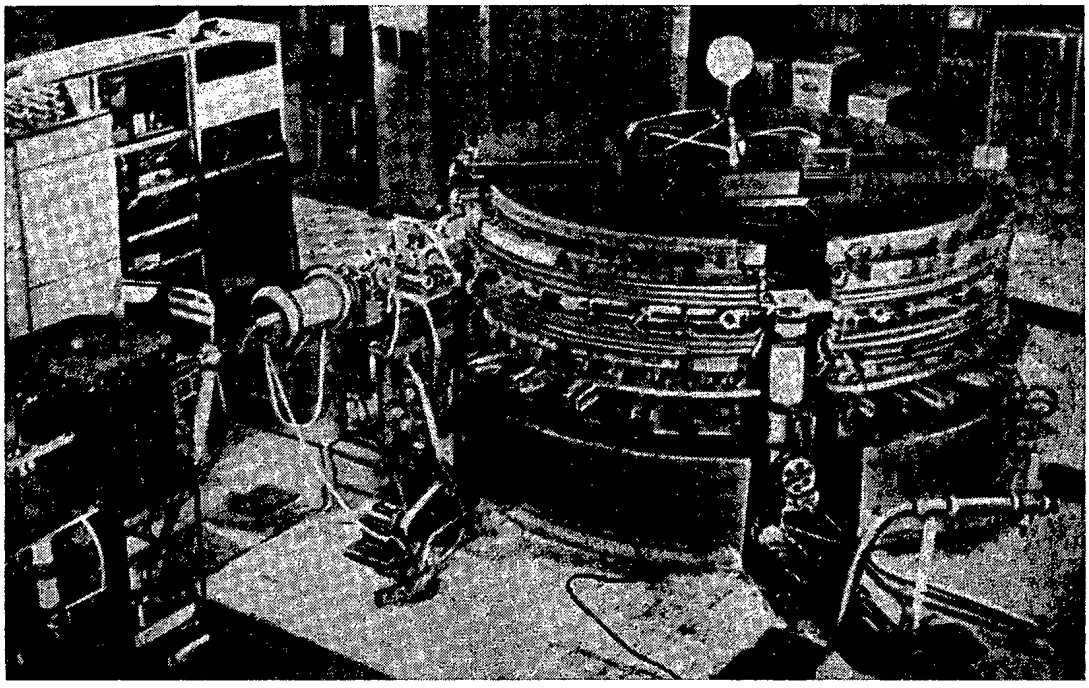

Fig.1. General view of 300-MeV synchrotron.

Translated from Atomnaya Énergiya, Vol.21, No.6, pp.502-503, December, 1966. Original letter submitted August 1, 1966.

battery of capacitors. The current amplitude in the winding is 758 A for a 8.7-kV voltage. The potential across the capacitor battery is stabilized to within ± 0.5%. To reduce power consumption, provision is made for recharging the capacitor battery from the electromagnet.

The injector is a two-electrode accelerator tube fed by pulses from a 250-kV transformer. The transformer pulses are rectangular, the stability of the flat part being not worse than 0.07%.

From the accelerator tube, the beam passes through the injection channel to the vacuum chamber, and is extracted parallel to the orbit by means of an electrostatic inflector located in the linear gap. Owing to the relatively low injection energy, the frequency of the accelerating field at the beginning of an acceleration cycle has to vary from 28.2 to 37.5 Mc/sec in about 300 μsec. To this end the entire hf channel is divided into two. The first channel operates during synchrophasotron acceleration, and changes the accelerating voltage frequency from 28.2 to 37 Mc/sec. Since the operating time of this first channel is short, it is based on GI-14B pulse tubes which can develop sufficient power in the required frequency band.

The first channel consists of a frequency-modulated generator of about 3 kW power, and an amplifier which gives an output power of the order of 6 kW. Frequency modulation is achieved by varying the inductance of the generator coil. This coil is wound on a ferrite ring and placed in the gap of a special electromagnet. The value and form of the excitation current of this electromagnet determines the modulation program. This scheme yields a marked reduction in modulating current and simplifies the circuits for shaping it.

Both stages of the first channel are modulated by a rectangular anode pulse: the output stage is switched in later, so as to attenuate transients occurring when the autogenerator is switched in.

The second channel is operative during the greater part of the acceleration cycle, and gives an accelerating voltage with an amplitude of 1100 V and a frequency of 37.5 Mc/sec. Particle losses during the transition from synchrophasotron to synchrotron acceleration are negligible. The accelerating structure consists of paired toroidal resonators. The transmission band of one of these is broadened by shunting its resistance.

To reduce the sizes of the resonators, each of them has lumped capacitors. The Q-factor of the wide-band resonator is 4,that of the narrow-band resonator is 160.

The resonators are close together, and therefore, to reduce coupling between them, their frequencies are widely separated (30 and 37.5 Mc/sec). To avoid energy losses by the electrons owing to interaction with the narrow-band resonator during the transition from synchrophasotron to synchrotron conditions, a frequency change is provided from 37 to 37.5 Mc/sec.

At present the individual units of the synchrotron are being developed and their stability improved. In future it is hoped to increase the pulse recurrence frequency.

COEFFICIENT OF CAPTURE OF PARTICLES IN AN ACCELERATOR

A. S. Bakai

UDC 621.384.6

The region of stable motion of particles in an accelerator or storage device is delimited by the phase surface of the energy-phase separatrix — an integral curve passing through a "saddle" point. If there is friction or a gradual secular change in the particle energies, the separatrix is not a closed curve (see Fig.1) but marks out a family of phase trajectories (in the figure, the region occupied by these trajectories is left unshaded), tending asymptotically to the equilibrium trajectory which corresponds to the focus Φ in Fig.1.

In calculating the coefficient of capture, we usually determine the ratio of the number of particles which at the moment of injection fall into the phase oscillation region 0 to the total number of injected particles. However, this does not allow for those particles which at first fall into the unshaded part of the phase surface above region 0, but after a time reach the latter region. Such particles sometimes fall into the accelerating phase of the hf field, sometimes into the decelerating phase, and do not, on average, receive energy from it. After a time, therefore, the energy of such a particle, owing to losses by radiation and increase in the equilibrium energy (in the accelerator), will become equal to the equilibrium energy. Capture of the particle by the accelerating field will depend on its phase at this instant. As will be seen from the figure, the initial conditions leading to phase trajectories in region 0 are closely interleaved with those which do not lead to such trajectories. It is therefore natural to determine the probability that a phase trajectory which begins above 0 will ultimately be inside 0 – the relative sizes of the unshaded areas. This probability has been calculated [1].

Sayasov and Mel'nikov [2] obtained a more accurate value for the coefficient of capture by allowing for the effect of changes in the particle energy during acceleration on the shape of the phase oscillation region 0; however, they did not allow for the possibility of capture of particles injected into the part of the phase surface lying above 0.

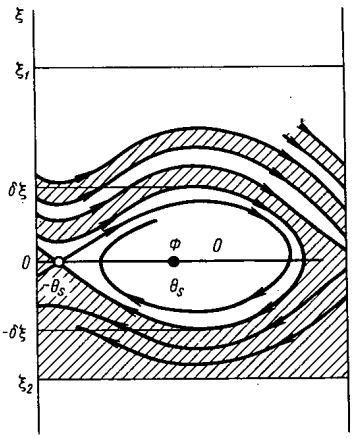

Fig. 1. General appearance of phase picture in the energy-phase plane (the heavy line shows the separatrix).

The equations representing the energy and phase of the particle, after linearization with respect to energy and averaging over rapid alternations, take the following form [3]:

$$\left.\begin{aligned}\dot{\xi} &= \varepsilon(\cos\theta - \cos\theta_s) - \Gamma\xi;\\ \dot{\theta} &= \alpha\xi, \quad \xi = \frac{E-E_s}{E_s},\end{aligned}\right\} \tag{1}$$

where E_S and θ_S are the equilibrium values of the energy and phase, while the coefficients α, ε, and Γ depend on the particular type of accelerator or storage device. For an accelerator they are not constant but depend on the particle velocity. For relativistic particle velocities or in storage devices, their variation is negligible, and the coefficients in (1) can be taken as constant.

Let us introduce a new variable,

$$\sigma = \frac{1}{2}\alpha\xi^2 - \varepsilon(\sin\theta - \theta\cos\theta_s), \tag{2}$$

so that, by (1) and (2),

$$\dot{\sigma} = \left(\frac{1}{2}\dot{\alpha} - \alpha\Gamma\right)\xi^2 - \dot{\varepsilon}(\sin\theta - \theta\cos\theta_s). \tag{3}$$

Translated from Atomnaya Énergiya, Vol. 21, No.6, pp.503-504, December, 1966. Original article submitted April 5, 1966.

We can easily verify that the equation

$$\sigma(\theta, \zeta) = \text{const}$$

represents the integral curves of (1) when $\Gamma = \dot{\alpha} = \dot{\varepsilon} = 0$.

If the injected particles are uniformly distributed in energy in the range $\xi_2 < \xi < \xi_1$, and also in phase, then for the coefficient of capture η we get

$$\eta = \frac{\Sigma_s}{\Sigma_n} = \frac{\Sigma_s}{2\pi(\xi_1 - \xi_2)} = \frac{\Sigma_0 + W 2\pi(\xi_1 - \delta\xi)}{2\pi(\xi_1 - \xi_2)} \quad (\xi_2 < -\delta\xi). \tag{4}$$

Here Σ_S is the area of the unshaded regions of the phase surface (Fig.1) enclosed between the lines $\xi = \xi_1$ and $\xi = \xi_2$; Σ_0 is the area of region 0; $\delta\xi$ is the maximum value of ξ in region 0; and W is the probability that a trajectory which begins in the region $\xi > \delta\xi$ will after a time find itself in 0.

It can be shown [1] that W is given by

$$W = \frac{2\Delta\sigma}{2\pi\varepsilon\cos\theta_s + \Delta\sigma}; \quad \Delta\sigma = \int_t^{t+\frac{1}{2}T_s} \sigma\, dt, \tag{5}$$

where T_S is the phase oscillation period, given by

$$T_s = 2(\varepsilon\alpha)^{-1/2} K\left(\sqrt{\frac{1-\sin\theta_s}{2}}\right).$$

Here $K(\varphi)$ is the complete elliptic integral of the first kind. Integral (5) and the expression for the coefficient of capture take an especially simple form in the practically important cases of relativistic injected-particle velocities and of storage devices, where the coefficients in (1) can be regarded as constant. In these cases,

$$\dot{\sigma} = -\alpha\Gamma\xi^2$$

and

$$\Delta\sigma = \left|\int_0^{\frac{1}{2}T_s} \dot{\sigma}\, dt\right| = \left|\oint_s \dot{\sigma}\frac{d\theta}{\dot{\theta}}\right| = \left|\Gamma\oint_s \xi\, d\theta\right| = \frac{1}{2}\Gamma\Sigma_0. \tag{6}$$

Here the integration is performed along the upper branch of the separatrix, which has an equation of the form

$$\sigma(\theta, \zeta) = \sigma(-\theta_s, 0).$$

Thus, by (4) and (6), we find that

$$\eta = \frac{\Sigma_0}{2\pi(\xi_1 - \xi_2)}\left[1 + \frac{4\pi\Gamma(\xi_1 - \delta\xi)}{4\pi\varepsilon\cos\theta_s + \Gamma\Sigma_0}\right]. \tag{7}$$

The second term in the square brackets in (7) allows for particles which have been injected above the phase oscillation region 0, but ultimately find themselves in this region.

From the above expression we see that the injection conditions must be chosen so that the lower bound of the injected-particle energy shall coincide with the lower bound of the phase oscillation region, i.e., so that $\xi_2 = -\delta\xi$. In addition, the number of captured particles injected into the region $-\delta\xi < \xi < \delta\xi$ may be less than the number of captured particles injected into the region $\xi > \delta\xi$, i.e.,

$$\frac{\Sigma_0}{4\pi\delta\zeta} < W.$$

In this case it is reasonable to choose the injection conditions so that

$$\zeta_2 > \delta\zeta.$$

Note that limitations on the capture coefficient may arise owing to other degrees of freedom of the particle, for example, radial motion in cyclic accelerators or storage rings. The radius of the

trajectory of a particle increases as the energy rises, and when the energy deviates sufficiently from the equilibrium value the particles will collide with the wall of the vacuum chamber. Thus in storage devices where it is desired to attain short accumulation times of the required currents, and thus relatively high capture coefficients, it may be advantageous to make the width of the magnetic track such that the particles with energies above the equilibrium value will not fall on to the wall.

The author is grateful to G. Ya. Lyubarskii for helpful advice.

LITERATURE CITED

1. A. S. Bakai, Differentsial'nye Uravneniya, No.4, 479 (1966).
2. Yu. S. Sayasov and V. K. Mel'nikov, ZhÉTF, 33, 656 (1960).
3. A. A. Kolomenskii and A. N. Lebedev, The Theory of Cyclic Accelerators, Moscow, Fizmatgiz (1962).

STABILIZATION OF LONGITUDINAL INSTABILITIES IN STORAGE DEVICES BY MEANS OF A FEEDBACK SYSTEM

É. A. Zhil'kov and A. N. Lebedev

UDC 621.384.60

It has been shown [1, 2] that under certain conditions a charged azimuthally uniform beam circulating in a storage device may develop unstable longitudinal density fluctuations. Taking as an example the so-called "negative mass" type of instability, we shall consider the possibility of stabilizing the beam by means of an electronic feedback circuit.

Following the notation of Kolomenskii and Lebedev [1], we shall represent a system of logitudinal oscillations in phase space by means of the kinetic equation

$$\frac{\partial f}{\partial t}+\omega_{\text{H}}\left(1+\varkappa\frac{\omega_{\text{H}}R_{\text{H}}}{E_{\text{H}}}w\right)\frac{\partial t}{\partial\vartheta}=-\frac{\partial F_0}{dw}\cdot e\mathscr{E}(\vartheta,\ t), \tag{1}$$

where $f(w, \vartheta, t)$ is the deviation of the distribution function from the equilibrium azimuthally homogeneous value $F_0(w)$; w is the deviation of the pulse from its mean value, ϑ is the generalized azimuth, and $\varkappa$ is the logarithmic partial derivative of the frequency of rotation ω_H with respect to the energy E_H (the subscript H denotes the value at the storage orbit of the particles, which has radius R_H). The quantity $\mathscr{E}(\vartheta, t)$ is the sum of the longitudinal electric field of the space charge,

$$\mathscr{E}'(\vartheta,\ t)=-\frac{\Lambda e}{R_{\text{H}}\gamma^2}\cdot\frac{\partial\rho}{\partial\vartheta};\ \rho=\frac{1}{R_{\text{H}}}\int_{-\infty}^{+\infty}f(w,\ \vartheta,\ t)\,dw;\quad\gamma=\frac{E_{\text{H}}}{mc^2} \tag{2}$$

(where $\Lambda\approx 1$ is a geometrical factor depending on the shape of the chamber [1]), and the electric field of the feedback system $\mathscr{E}''$.

Let us suppose that the sensor of the stablization system is located at the point $\vartheta = 0$, and acts on the linear density ρ of the beam at this azimuth, and that the amplitude characteristic of the feedback circuit is linear. If the azimuthal distribution of the field $\mathscr{E}''$ is represented by a function $\psi(\vartheta)$, normalized to unity, then for the Fourier harmonic $\rho, \mathscr{E} \sim \exp i(\omega t - k\vartheta)$ we have

$$\mathscr{E}''(\omega, k)=eK(\omega)\psi(k)\rho(\omega,\ \vartheta)|_{\vartheta=0}=eK(\omega)\psi(k)\sum_{k\neq 0}\rho(\omega,\ k'), \tag{3}$$

where the function $K(\omega)$ is the frequency characteristic of the feedback circuit.

Combining (2) and (3) with the solution of the kinetic equation (1) in the usual way, we get a dispersion relation

$$1-\frac{ie^2}{R_{\text{H}}}K(\omega)\sum_{k\neq 0}\frac{\psi(k)J_k(\omega)}{1+\frac{e^2\Lambda k}{R_{\text{H}}^2\gamma^2}J_k(\omega)}=0, \tag{4}$$

of which the roots ω_n determine the asymptotic behavior of perturbations to the density. The quantity J_k is related to the equilibrium distribution function

$$J_k(\omega)=\int_{-\infty}^{+\infty}\left[\omega-k\omega_{\text{H}}\left(1+\varkappa\frac{\omega_{\text{H}}R_{\text{H}}w}{E_{\text{H}}}\right)\right]^{-1}\cdot\frac{dF_0}{dw}\,dw, \tag{5}$$

where the integral is taken for a value of ω lying in the upper half-plane and is extended analytically to the lower half-plane. If the stabilization system is switched off, i.e., if $K(\omega)\equiv 0$, the dispersion relation becomes the usual expression [1], because the denominator in the sum in (4) must become zero. In this case the stability is determined by the ratio between two parameters, Δ/ω_H — half the relative

Translated from Atomnaya Énergiya, Vol. 21, No. 6, pp.505-506, December, 1966. Original article submitted March 3, 1966.

scatter of the particles in rotation frequency, and

$$\xi = -\frac{\Lambda r_0 N \mathcal{K}}{R_H \gamma^3 2\pi} \ll 1 \left(r_0 = \frac{e^2}{mc^2} \right), \tag{6}$$

which characterizes the space-charge's influence(N being the number of particles in the beam). If $\Delta^2/\omega_H^2 < \xi$ we shall get a "negative-mass" type of instability, so called because when $\xi > 0$ the quantity $\mathcal{K}$, which in the phase equation plays the role of the effective mass, must be negative. Note that in this case the roots of the dispersion equation ω_n lie on the complex plane near to the points $n\omega_H$ corresponding to equilibrium motion.

At frequencies where the amplification coefficient is not too great, the roots will as before lie in the neighborhood of the points $n\omega_H$, and therefore in the sum in (4) we can leave only one resonance term, and the dispersion equation will take the same form as for the case of a free beam, but with ξ replaced by ξ':

$$\left.\begin{aligned} \xi' &= \xi \left[1 - M(n\omega_H) \cdot \frac{\psi(n)}{n} \right], \\ M(\omega) &= \frac{iR_H\gamma^2}{\Lambda} K(\omega). \end{aligned}\right\} \tag{7}$$

Note, by the way, that the second term in the square brackets has the meaning of a proportionality coefficient between $\mathcal{E}''(\omega, n)$ and $\mathcal{E}'(\omega, n)$, i.e., the field-amplification coefficient. When we use (7) we must have $|M\xi| \ll 1$, for only in this case will the roots of the dispersion equation actually lie near the points $n\omega_H$ so that we can neglect all the nonresonance terms in (4). Physically this means that spontaneous fluctuations of the beam are, as before, a superposition of travelling waves of the type exp $i(\omega_n t - k\vartheta)$, not mutually interacting.

The stability conditions are that ξ' shall be real and $\xi' < \Delta^2/\omega_H^2$ (or, with some margin, $\xi' < 0$): they can be achieved by suitable choice of $K(n\omega_H)$.

In the region where the feedback coefficient ratio is large, the roots of the dispersion equation are far from the points $n\omega_H$ and resonance between the particles and the wave is destroyed. In this case it is essential to retain all the terms of the sum in (4), i.e., the effects of waves with different k linked via the feedback system. If the feedback coefficient is very large ($|M\xi| \gg 1$), the electric field and the perturbations to the density cease to be travelling waves, as in the case when $|M\xi| \ll 1$, but bevome standing waves of the type $\mathcal{E}(t, \vartheta) \sim \psi(\vartheta)$ exp $i\omega_n t$. Since in the nonresonance case the J_k take their asymptotic values

$$J_k \approx \frac{k\omega_H^2 R_H^2 \gamma^2 \xi}{\Lambda e^2 (\omega - k\omega_H)^2}, \quad |\omega - k\omega_H| \gtrsim \Delta, \tag{8}$$

in the denominator of (4) we can neglect the second term in comparison with unity. Summation with respect to k then gives a equation for the natural frequencies ω_n:

$$\frac{d}{dz} \cdot \frac{z}{\sin \pi z} \int_0^{2\pi} \psi(\vartheta)\, e^{iz(\vartheta - \pi)}\, d\vartheta = -\frac{2}{M\xi}; \quad z = \frac{\omega}{\omega_H}. \tag{9}$$

The roots of (9) naturally depend on the actual shape of $\psi(\vartheta)$, and in some cases may in general be nonexistent in the region where $|M\xi| \gg 1$. As an example, consider the case when the field $\mathcal{E}''$ is concentrated at one point opposite the sensor, i.e., $\psi(\vartheta) = \delta(\vartheta - \pi)$. Then

$$\omega_0 \approx -\frac{3\omega_H}{2\pi M\xi},$$

$$\omega_n|_{n>1} \approx \pm \omega_H \left[n + \frac{1}{2} - \pi^{-2} \left(n + \frac{1}{2} \right)^{-1} \right] - \frac{2(-1)^n \omega_H \sin \left[\pi \left(n + \frac{1}{2} \right) \right]^{-1}}{M\xi}. \tag{10}$$

It is easy to see that the stability condition for all n is simply that $M\xi$ shall be real. It is interesting to note that for large n the natural oscillation frequency is almost exactly halfway between two harmonics of the rotation frequency.

LITERATURE CITED

1. A. A. Kolomenskii and A. N. Lebedev, Proc. Inter. Conf. on High Energy Accel. CERN, 1959, p.115; Atomnaya Énergiya, 7, 549 (1959).
2. C. Nielsen, A. Sessler, and K. Symon, Proc. Inter. Conf. on High Energy Accel., CERN, p.239 (1959).

RADIATIVE CAPTURE OF FAST NEUTRONS BY Y^{89}

V. A. Tolstikov, V. P. Koroleva,
V. E. Kolesov, and A. G. Dovbenko

UDC 539.172.4;539.17.012

A relative activation method was used to measure the cross sections of radiative capture of neutrons with energies of 0.16-3.6 MeV by the magic isotope Y^{89}.

The method of measurement has been described in [1, 2]. The reference cross sections used for determining the cross section of radiative capture by Y^{89} from the experimental data were the capture cross section of the thermal neutrons in Y^{89}, producing an activity with $T\frac{1}{2} = 64.4$ h, which was equal to 1.26 ± 0.08 b [3], and the cross section of fission of U^{235} by thermal neutrons, equal to 577.1 ± 0.9 b [4]. The cross section of fission of U^{235} by fast neutrons was taken from the curve recommended in [5].

The measurement results were plotted on a graph and compared with the data of other authors (Fig. 1). Another study [6], covering a narrower energy range, was published while the results of our measurements were being processed; the results of [6] are also shown in the figure. The measurement errors in the figure were total erros, i. e., they include both experimental error and errors in the reference cross sections. The cross sections of Y^{89} radiative capture were calculated on the basis of the statistical theory of nuclear reactions. The method of calculations is explained in detail in [2, 7].

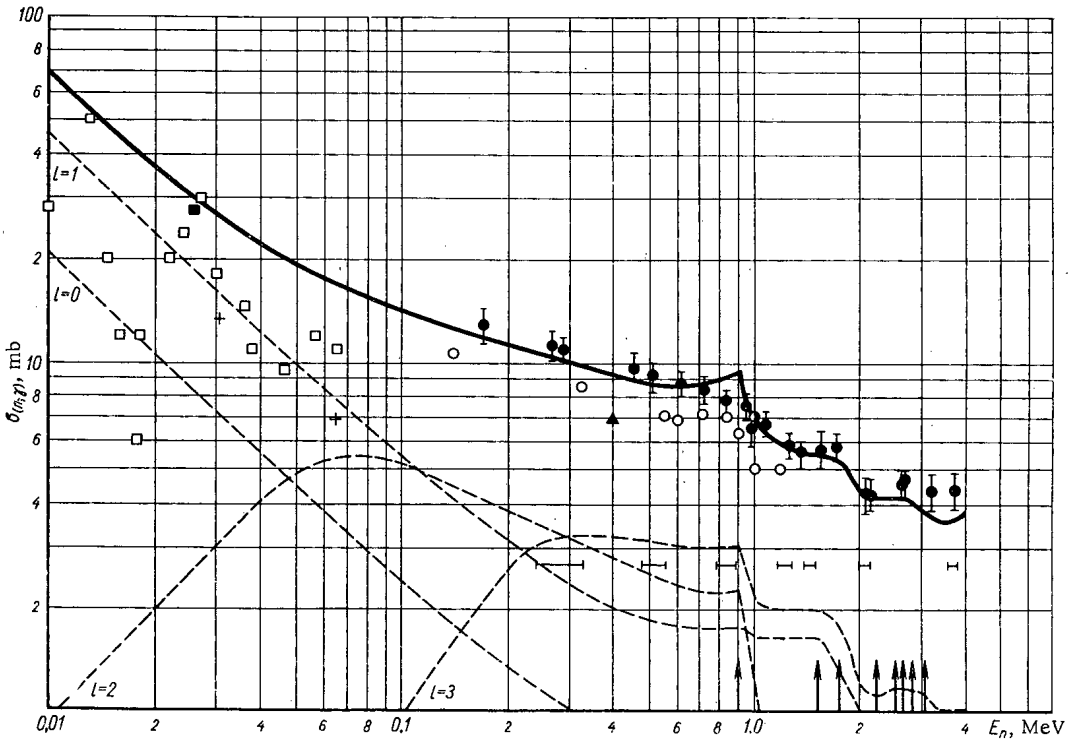

Fig. 1. Results obtained by measuring the cross section of radiative capture of neutrons (Y^{89} (n, γ) Y^{90}) and comparins with the results of other studies and with theoretical data: ●) data of present study; ○) [6]; ▲) [9]; ◑) [10]; ■) [11]; +) [12]; □) [13].

Translated from Atomnaya Énergiya, Vol. 21, No. 6, pp. 506-507, December, 1966. Original article submitted September 2, 1966.

The following parameters were used in determining the nuclear potential: $\varkappa = 0.35 \cdot 10^{-26}$ cm^2; $V_0 = 45$ MeV; $d = 0.5 \cdot 10^{-13}$ cm; $\xi = 0.1$; $R = 6.05 \cdot 10^{-13}$ cm. The compound-nucleus parameter values used in the calculation were B = 6.84 MeV [3] and $a = 8.8$ MeV^{-1}. The best agreement between theoretical and experimental data was obtained for the values $\bar{\Gamma}_\gamma = 0.3$ eV and $\bar{D} = 6000$ eV. The value of $\bar{D}$ agrees with the value of a used in the calculation.

The values of the energies, spins, and parities of the excited levels of the Y^{89} target nucleus which were necessary for the calculation were taken from [8]:

$$0, \left(\frac{1^-}{2}\right); 0.909 \text{ MeV}, \left(\frac{5^+}{2}\right); 1.51 \text{ MeV}, \left(\frac{3^-}{2}\right); 1.75 \text{ MeV},$$
$$\left(\frac{5^-}{2}\right); 2.22 \text{ MeV}, \left(\frac{5^+}{2}\right); 2.53 \text{ MeV}, \left(\frac{7^+}{2}, \frac{5^+}{2}\right);$$
$$2.61 \text{ MeV}, \left(\frac{9^+}{2}\right); 2.84 \text{ MeV}, \left(\frac{3^-}{2}\right); 3.05 \text{ MeV}, \left(\frac{5^-}{2}\right).$$

Here the first number is the energy of the excited level. The agreement with the experimental results is improved if we assign a spin value of $7/2^+$ to the level with energy 2.53 MeV.

The solid curve on the figure represents the total capture cross section, while the dashed curves represent the amounts contributed to the cross section by neutrons with different orbital moments.

The positions of the excited levels of the Y^{89} nucleus are shown by vertical arrows; the horizontal bars represent typical values of the energy spread of neutrons used for irradiating the yttrium.

As can be seen from the figure the theory describes the experiment with relatively good accuracy over practically the entire range of neutron energies. The nonmonotonic variation of radiative-capture cross section as a function of energy is due to competition with inelastic scattering of the neutrons.

LITERATURE CITED

1. Yu. Ya. Stavisskii and V. A. Tolstikov, In the collection "Proceedings of the Second All-Union Conference on Nuclear Reactions at Low and Intermediate Energies (July, 1960)" [in Russian], Moscow, Izd-vo AN SSSR, p. 562 (1962).
2. V. A. Tolstikov et al., Atomnaya Énergiya, 21, 45 (1966).
3. I. V. Gordeev, D. A. Kardashev, and A. V. Malyshev, Nuclear Physics Constants [in Russian], Moscow, Gosatomizdat (1963).
4. J. Stehn et al., Neutron Cross Sections, BNL-325, second edition, Suppl. No. 2, Vol. III, Z-88 to 98 (1965).
5. K. Parker, AWREO-82/63 (1963).
6. H. Grench et al., WASH-1064, p. 67 (1965).
7. V. A. Tolstikov et al., Atomnaya Énergiya, 17, 505 (1964).
8. S. Shafroth, P. Trehan, and D. Van Patter, Phys. Rev. 129, 704 (1963).
9. B. Diven, J. Terrell, and A. Hemmendinger, Phys. Rev., 120, 556 (1960).
10. D. Hughes, R. Gart, and D. Lerin, Phys. Rev., 91, 1423 (1953).
11. R. Booth, W. Ball, and M. MacGregor, Phys. Rev., 112, 226 (1958).
12. R. Macklin, J. Gibbons, and T. Inada, Phys. Rev., 129, 2695 (1963).
13. R. Macklin et al., Nucl. Phys., 43, 353 (1963).

ON THE MEASUREMENT OF THERMAL-NEUTRON FLUXES AND CADMIUM RATIOS FROM THE ACTIVATION OF GOLD

S. S. Bugorkov, A. S. Krivokhatskii, K. A. Petrzhak, N. V. Skovorodkin, and A. V. Sorokina

UDC 539.125.52:539.16.08

One of the present-day methods of measuring a flux of thermal neutrons is measuring the activity of gold produced in the Au^{197} (n, γ) Au^{198} reaction. The capture cross section of gold for thermal neutrons obeys a 1/v law, but for a neutron energy of 4.9 eV there is a strong resonance. In order to eliminate the influence of the resonance part of the cross section, the gold is irradiated both in a cadmium jacket and without such a jacket; the activity of the gold which results from the capture of thermal neutrons below the cadmium resonance is then determined from the formula

$$A_{\text{th}} = A_{\text{noCd}} \frac{R-1}{R},$$

where $A_{\text{no Cd}}$ is the activity of the gold irradiated without a cadmium jacket, and R is the so-called cadmium ratio, equal to the ratio of the activity of the gold irradiated without a cadmium jacket to the activity of the gold irradiated with a cadmium jacket. The activity of gold foil resulting from the capture of thermal neutrons, for which $\sigma_{n,\gamma}(v) = \sigma_0 v_0 / v_0$, is determined by the formula

$$A_{\text{th}} = N_{\text{Au}} (1 - e^{-\lambda t}) \sigma_0 v_0 \int_0^{v_{\text{Cd}}} n(v)\, dv,$$

where N_{Au} is the number of gold atoms in the foil; λ is the radioactive decay constant of the gold; t is the irradiation time; v_0 is the most probable velocity of the Maxwell spectrum neutrons ($v_0 = 2200$ m/sec); σ_0 is the cross section of capture of neutrons with velocity v_0, which for Au^{197} is equal to $(98.8 + 0.3) \cdot 10^{-24}$ cm^2 [1]; n(v) is the density of neutrons with velocity v; $\int_0^{v_{\text{Cd}}} n(v)\, dv = n$ is the total density of thermal neutrons in the velocity range up to the cadmium cutoff. The product $nv_0 = \Phi_0$ is called the effective thermal-neutron flux:

$$\Phi_0 = \frac{A_{\text{noCd}}}{N_{\text{Au}} \sigma_0 (1 - e^{-\lambda t})} \cdot \frac{R-1}{R}.$$

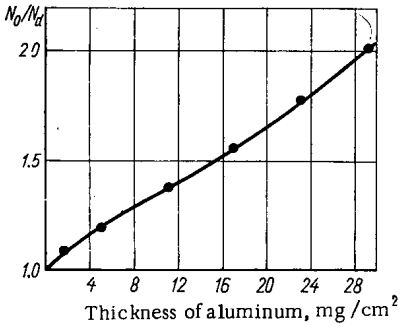

Fig. 1. Absorption of β-particles from Au^{198} by aluminum.

In order to yield the correct cadmium ratio, the neutron density and neutron spectrum should not vary within the indicator, i.e., the irradiated gold should be practically "transparent" to trans-cadmium neutrons. From [2] it follows that this requirement is satisfied by gold foil with a thickness of 100-200 $\mu g/cm^2$. The error in determining the weight on ordinary microbalances is $\geq 2\%$ for a foil weighing 50 μg. The activity of such a foil after irradiation is found to be rather high. Thus, when the irradiation time is 10 min and the flux is 10^{12}-10^{13} neutrons/sec·cm^2, the β activity of a gold foil weighing 50 μg will be more than 10^6-10^7 disintegrations/min. Absolute measurements of such high activities are carried out by means of a β-γ coincidence apparatus or a graduated scintillation spectrometer, as well as by dissolving the gold foil and thereafter measuring the activity of an aliquot part with a $4\pi\beta$-counter. The β-γ coincidence method and the scintillation spectroscopy method

Translated from Atomnaya Énergiya, Vol.21, No.6, pp.508-509, December, 1966. Original article submitted September 2, 1966.

Thermal-Neutron Flux and Cadmium Ratios

Weight of target mg	Thickness of target, mg/cm^2	Activity of target at end of irradiation, disintegrations/min		Cadmium ratio R	Thermal-neutron flux, C_0, neutrons /sec·cm^2
		Without cadmium jacket	With cadmium jacket		
3.5	7	$2{,}93 \cdot 10^9$	$2{,}55 \cdot 10^8$	$11.5 \pm 0{,}4$	$(1{,}98 \pm 0{,}07) \cdot 10^{12}$
$1 \cdot 10^{-3}$	$2 \cdot 10^{-3}$	$8{,}72 \cdot 10^5$	$1{,}01 \cdot 10^5$	$8.6 \pm 0{,}3$	$(2.01 \pm 0{,}08) \cdot 10^{12}$

require complicated apparatus, and the dilution method (the 4 π method) increases both the time required for determining the flux and the radiation exposure of the personnel.

In the present study we tested a method which makes it possible to determine the activity of irradiated gold targets in a $4\pi\beta$ counter without the necessity of dissolving the active gold. In this method, all the chemical operations of dissolving the gold and taking the aliquot parts are carried out before irradiation. This makes it possible to obtain gold targets of any given thickness, for which the weight of the gold is determined with an error of less than 1%.

We prepared a solution of inactive gold with a known weight concentration. From the solution we weighed out the required aliquot part, spread it on a disc of AV00000 aluminum of known thickness, and dried it. In the drying process, the gold was distributed fairly evenly over the surface of the disc, which was confirmed by x-ray examination of the irradiated targets. After drying, the discs were heated to about 300°C and were covered from above with an identical aluminum disc. Discs of pure aluminum were irradiated at the same time as the targets, in order to determine how much background was contributed by the activity induced in the aluminum. For irradiation in a flux of 10^{12}-10^{13} neutrons/sec·cm^2, we spread 1.0-0.5 μg of gold over a 0.5-cm^2 area of a target 16-17 mm in diameter.

Five or six days after the irradiation, which had lasted 2 h, the activity of the targets was measured in a $4\pi\beta$ counter. The background from the aluminum discs was 3% of the activity of the gold after one day and 0.5% after five days; it was caused by the activation of unknown impurities, since the activity of the Al^{28} itself should be down to a few hundredths of 1% of the activity of the gold even 1 h after the irradiation is completed. This background must be found experimentally for each brand of aluminum used.

To determine the absolute activity of the Au^{198}, we must take into account the absorption of β particles from the gold by the aluminum. For this purpose we plotted a curve of the absorption of the β radiation from the Au^{198}. A solution of active gold was spread on a metallized colloidal film with a thickness of about 15 μg/cm^2. After measuring the activity with a 4 $\pi\beta$ counter, we glued aluminum foil of the same thickness on both sides of the film in succession and again measured the activity with a $4\pi\beta$ counter. Figure 1 shows how the ratio of N_0, the activity on the film, to N_d, the activity recorded through the aluminum filter, varies as a function of filter thickness. The graph indicates that for an aluminum foil with a thickness of 21.6 mg/cm^2 which was used in the experiment, the correction for the absorption of β radiation from the Au^{198} was 71%. The measured thermal-neutron fluxes and cadmium ratios are shown in the table; each value was obtained by averaging over three experiments.

It can be seen from the table that the thermal-neutron flux values determined from the activation of the gold foil agree with those obtained with the targets used in the present study. A gold foil with thickness 7 mg/cm^2 is practically transparent to thermal neutrons and gives a correct value of the effective thermal flux. However, the cadmium ratio determined from the activation of such foil is found to be 34% higher than the cadmium ratio obtained from the activation of the proposed targets.

Thus, by using such targets, we can obtain correct values of the thermal-neutron flux and the cadmium ratio, work with much lower activities, eliminate the need for chemical operations with high activities, considerably reduce the amount of gold used, and reduce the time required for determining the thermal-neutron flux.

LITERATURE CITED

1. F. Gloud et al., Nucl. Sci. Engng., 8, 453 (1960).
2. M. Brose, Nucleonik, 6, 134 (1964).

WATER REACTOR HOT LOOP STUDIES

A. P. Veselkin, A. V. Nikitin, and Yu. V. Orlov

UDC 621.039.573

Nuclear reactors are now widely used as sources of ionizing radiation in physics, chemistry, technology, and medicine. But mixed gamma and neutron emission over a broad energy spectrum is not consistently desirable in research. A radiation loop with a set of emitters of different geometrical configurations was built for a water-cooled water-moderated research reactor with a view to expanding its research capabilities.

High-purity water passing through the reactor core at a pressure of 1 ab.atm. and temperature of 20-30°C is activated prior to entering the emitter, which is employed as a source of hard gammas with energies of 6.13 and 7.10 MeV [1]. Induced activity in the water is determined by the decay of the N^{16} formed in the $O^{16}(n,p)N^{16}$ reaction. The intensity of neutron emission accompanying N^{17} decay is lower by two or three orders of magnitude.

Characteristics of the "Ulitka" [Snail] emitter, externally a disk slab wound from 8 × 1 tubing, were studied in detail in the hot loop. The slab O.D. is 470 mm, its I.D. is 30 mm, the turns number 26, and average winding pitch is 8.5 mm on a side. Active water is fed in centrally and drained on the periphery of the slab. The total activity of the source is 3 mCi. Variations in linear activity (μ/cm), i.e., activity per unit tube length along the radius ρ of Ulitka, shows a Gaussian distribution [2]

$$S(\rho) = S(0)\, e^{-\alpha^2\rho^2} \tag{1}$$

and allows for independent control of the main parameters: the smoothness factor α^2 and the activity S(0) at the entrance, calculated by the formulas

$$S(0) = R\,\frac{F}{k_r k_z 3{,}7\cdot 10^7}\,(1-e^{-\lambda t'})\,e^{-\lambda t}, \tag{2}$$

$$\alpha^2 = \frac{\pi\lambda}{wb}, \tag{3}$$

where

$$R = \int_{E\ \text{thres}}^{\infty} \Sigma_{\text{act}}(E)\,\Phi(E)\,dE \tag{4}$$

(here $\Sigma_{act}(E)$ is the macroscopic cross section for the activation reaction, in cm^{-1}; $\Phi(E)$ is the differential fast flux at the core center, in neutrons/cm^2·sec·MeV); k_z is the smoothness factor of the fast flux distribution in core height; k_r is the ratio of fast flux at the site of the experimental channel to neutron flux at the core center; λ is the radioactive decay constant, sec^{-1}; t' is the exposure time of the water in the channel, sec; t is the time it takes the water to flow from the core exit to the emitter entrance, sec; F is the area of the inner cross section of the Ulitka tube, cm^2; w is the water flowspeed in Ulitka cm/sec; and b is the pitch of the Ulitka tube winding, cm.

The fast neutron spectrum in the reactor, $\Phi(E)$, was calculated by a procedure recommended elsewhere [3] for water-cooled water-moderated reactors.

Integration over the source surface yields a formula for the dose rate D at a distance a from the Ulitka plane on its axis (in the absence of any absorber or scatterer between source and detector):

$$D(a) = \frac{\pi p\gamma S(0)}{b}\, e^{\alpha^2 a^2}\{E_1(\alpha^2 a^2) - E_1[\alpha^2(a^2+\rho^2)]\}, \tag{5}$$

where $\rho\gamma$ is the gamma radiation constant of the nuclide, p·cm^2/h·Ci; $E_1(x)$ is the first-order integral-exponential function [1].

Translated from Atomnaya Énergiya, Vol. 21, No. 6, pp. 509-511, December, 1966. Original article submitted December 21, 1965; revised June 14, 1966.

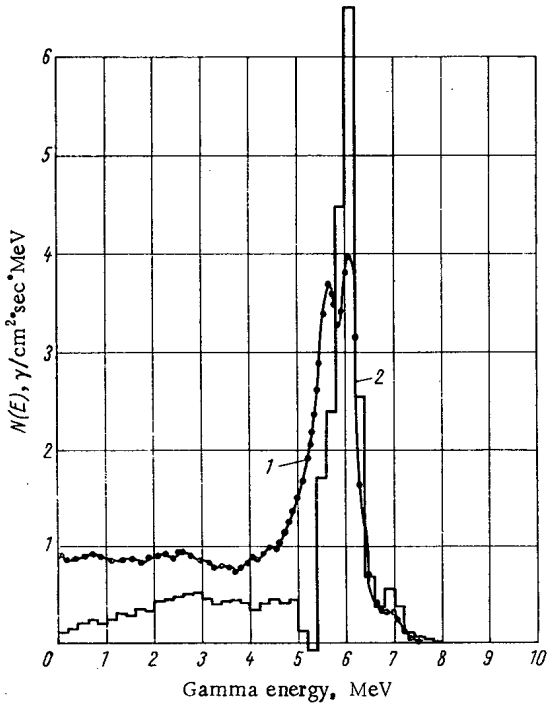

Fig. 1. γ-Ray spectrum of Ulitka source: 1) amplitude distribution; 2) energy distribution.

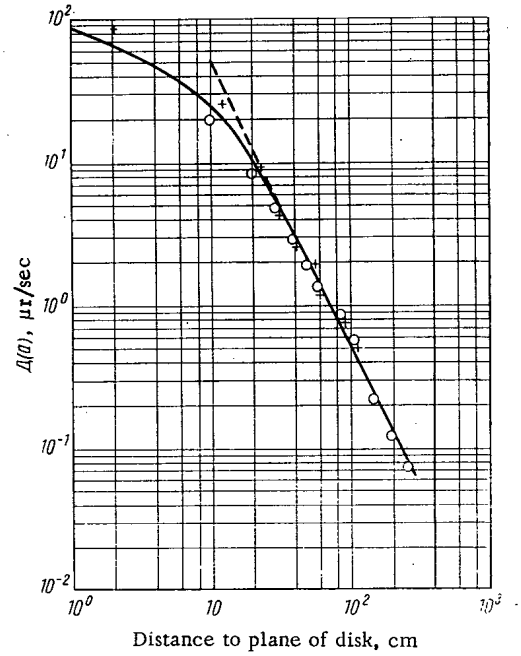

Fig. 2. γ-Dose rate as a function of distance to source plane:———) calculations based on formula (5);- - - - - - - -) calculations based on formula (6); +) dosimeter, 3 cm³ plastic volume; ○) dosimeter, 100 cm³ plastic volume.

Dose rate attenuation satisfies the quadratic law

$$D(a) = \frac{\pi p_\gamma S(0)}{b}\left(\frac{\rho}{a}\right)^2 \qquad (6)$$

at a sufficient distance from the Ulitka plane ($a^2 \gg \rho^2$).

Figure 1 shows the energy and amplitude distribution of gammas (measured with an 80 × 80 mm CsI(Tl) crystal). Reference [4] describes how to convert from amplitude distribution to energy distribution. The energy distribution peaks twice, near energies 6.1 and 7.1 MeV, with an intensity ratio 11 : 1 (N^{16} decay), so that the emitter is practically a source of monoenergetic 6.1 MeV gammas.

By using a lead collimator 150 mm long with a hole 10 mm in diameter, we could measure the source activity distribution over the Ulitka radius at a loop water flowrate of 60 kg/h. The distribution follows Eq. (1) quite closely for $\alpha^2 = 5.48 \cdot 10^{-3}$ cm^{-2}. The computed α^2 is $5.75 \cdot 10^{-3}$. The equilibrium dose rate is established 10 sec after the valve is opened. When the reactor is shut down, dose rate falls to background level with a half-life ≈ 8 sec.

The variation of dose rate to the Ulitka plane is worth finding out in some phases of research. This dependence was measured by using two scintillation plastic gamma-ray dosimeters: one 50 mm in diameter and 50 mm high (volume ≈ 100 cm³), the other 20 mm in diameter and 10 mm high (volume ≈ 3 cm³). The dosimeters were first given an absolute calibration by means of a standard Co^{60} source. Results of measurements and calculations based on Eq. (5) are shown in Fig. 2. Predicted and measured dose rate – distance to emitter plane dependences are the same, and the quadratic law (6) is observed at distances beyond 30 cm. But predicted data are about one half the experimental values in absolute values (Fig. 2 shows predicted results arbitrarily doubled). This discrepancy can be accounted for by the inadequate knowledge of absolute flux and core fast spectrum, activation cross section, and also by the experimental error (± 20%) associated with determination of the absolute value of the gamma-radiation dose rate.

The neutron dose rate of the Ulitka (induced N^{17} activity) was one-hundredth of the gamma-dose rate, according to measurements using a RUS-5.

Relative concentrations of chemical forms of N^{16} in the reactor water were also measured with the aid of the hot loop described here. The procedure used for the measurements was similar to that used in [5]. The radioactive water was let alternately through three ion-exchange columns connected in parallel. The first column contained cation exchange resin, the second contained anion exchange resin, the third a neutral resin which did not trap nitrogen compounds, but did bring about identical holdup conditions and decay of radioactive atoms. After passing through the columns, the water entered a measuring tank, and measurements there yielded information on chemical forms of N^{16} in the reactor water. Only gamma emission of higher than 4.5 MeV energy was recorded there. The pH of the reactor water fluctuated between 6.4 and 6.9. The fraction of anion forms of N^{16} (NO_2^-, NO_3^-, ...) was found to be 60% at 20°C, as against 15% for cation forms (NH_4^+, ...), and 25% for neutral forms (NO, NO_2, N_2, $NH_3 \cdot H_2O$, ...). Comparing these results to the data reported in [5] is no simple matter, since the EBWR is a boiling-water reactor.

The hot loop is now being rebuilt to step up emitter intensity ten times.

The authors are indebted to A. V. Zhenikhova for systematic monitoring of the reactor water pH; to V. V. Gerasimov for setting up the ion exchange columns and for a fruitful discussion of the results; to Yu. G. Anisimov for his kind aid in the measurements and data processing, and to the reactor staff for setting up and operating the hot loop.

LITERATURE CITED

1. Reactor Shielding, Design Manual, T. Rockwell, Van Nostrand, Princeton, N.J. (1956).
2. K. Shur and P. Reuss, Shielding of Nuclear Propulsion Vehicles, Edit. transl. by V. V. Orlov and S. G. Tsypin, Moscow, Foreign lit. press, 1961, p.197 [Russian translation].
3. T. Tagami, M. Jamamoto, and V. Osawa, J. Atomic Energy Society Japan, 6, 260 (1964).
4. Yu. V. Orlov and A. A. Sevost'yanov, Pribory i Tekhnika Éxperimenta, No.1, 45 (1966).
5. R. Mittl and M. Theys, Nucleonics, 19, 81 (1961).

MONITORING THE OXYGEN AND HYDROGEN CONTENTS OF FUSED SODIUM BY MEASURING ITS ELECTRICAL RESISTANCE

V. I. Subbotin, M. N. Ivanovskii, M. N. Arnol'dov, B. A. Shmatko, and A. D. Pleshivtsev

UDC 621.039.534.6

Control of the gaseous impurities of the sodium is a prerequisite for the operation of sodium-cooled nuclear reactors. The presence of dissolved impurities in the liquid metal is known to affect many of its physical properties. Thus changes in these properties can serve to indicate changes in the impurity contents.

Of especial interest is impurity control by electrical resistance measurement, which can easily be achieved by means of simple methods and apparatus, either by remote control or automatically.

Blake [1] described a device based on resistance measurement, with which he monitored the purity of sodium-potassium alloy circulating in a nuclear reactor. He assumed that the resistance of liquid sodium varies because of changes in the content of oxygen present in the alloy as sodium oxide. The effect of temperature on the resistance was eliminated by a special measurement technique. The resistance of the alloy was determined during its purification in a cold trap. The results indicate how the resistance varies with the extent of purification. However, Blake [1] gave no proof that the resistance of the alloy does in fact change because of changes in the oxygen content, nor did he produce a quantitative relation between the resistance and the contents of oxygen or other impurities. He arbitrarily assumed that the relation between the resistance of a sodium-potassium alloy and its oxygen content is similar to the corresponding relation for certain other metals (copper, niobium).

Subsequently Claxton [2] showed that the relation between the resistance and the impurity concentration is not specific for oxygen dissolved in sodium, and hence not for a sodium-potassium alloy. According to these results, the oxygen content in such liquid alloys cannot be monitored by measuring their electrical resistances.

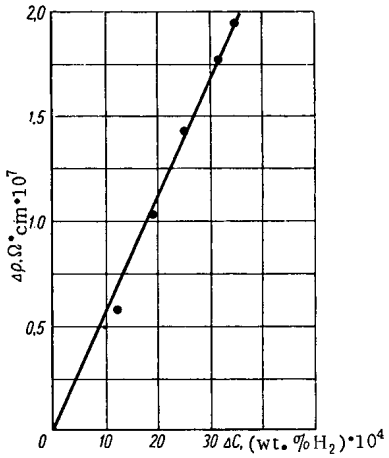

Fig. 1. Electrical resistance of sodium versus hydrogen concentration (sodium temperature: 350°C).

The first experimental data on the relation between the resistance of sodium and its oxygen content were given by Kozlov et al. [3].

The relation given between the resistivity of sodium at 350°C as a function of its oxygen concentration, was as follows:

$$\rho_{350^\circ C} = 0{,}189\,(1 + \Delta C),$$

where ΔC is the change in oxygen concentration in wt.%, ρ is the resistivity in ohm·mm^2/m. The measurements were made in circulation loop by means of a device similar to that described in [1].

The resistance increment per unit oxygen concentration was found to be 20 $\mu\Omega$·cm/wt.% O_2. This value is very high.

Thus the literature contains contradictory data on the relation between the resistance and oxygen content of liquid sodium.

We have measured the resistivity of sodium at 350° C in relation to its oxygen and hydrogen contents. Hydrogen is one of the most characteristic impurities in sodium coolants.

Translated from Atomnaya Énergiya, Vol. 21, No. 6, pp. 511-512, December, 1966. Original article submitted June 23, 1966.

The literature does not contain any experimental data on the relation between the electrical resistance and hydrogen content of sodium.

We used a double dc bridge. The sodium was contained in a measuring tube of 1Kh18N9T steel, with an external diameter of 9 mm and wall thickness of 0.4 mm, into which current and potential electrodes were soldered. The tube was connected to a sodium circulation loop with a pump for driving round the sodium and a device for introducing oxygen and hydrogen into the metal.

The oxygen and hydrogen were introduced in the gaseous form. The certified compositions of these gases were as follows: oxygen) total 99.2%, moisture $< 7 \cdot 10^{-2}$%; hydrogen) total 99.5%, moisture $< 5 \cdot 10^{-2}$%.

The amount of gas introduced was found by measuring its pressure in a tank of known volume at known temperature. In addition, oxygen was also introduced as sodium peroxide. Continual circulation of the sodium through the measurement tube ensured that the composition of the metal was constant during the measurements.

The temperature of the sodium circulating in the loop and through the tube was 350°C. It was held at this level in the measurement tube to within 0.05°C by a thermostat.

The initial impurity content of the sodium used was as follows:

Element	O	Fe, Mg, H, Si, Ca, Al	Ag, Cu, B, Li	Ti	K
Content wt.%	$5 \cdot 10^{-4}$	$< 1 \cdot 10^{-3}$	$< 1 \cdot 10^{-4}$	$1.5 \cdot 10^{-3}$	$3.7 \cdot 10^{-3}$

Chemical analysis revealed that the contents of the other impurities remained unchanged when the oxygen was introduced. Altogether, $1.6 \cdot 10^{-2}$ wt.% of oxygen was introduced in several portions. After the addition of the last portion, the sodium was saturated with sodium oxide at 350°C; the content of this substance was controlled by the distillation method.

During addition of the oxygen, we did not detect any change in the resistance of the measurement tube and sodium greater than the experimental error, which was $5 \cdot 10^{-8}$ Ω (at 350°C, the resistance of the measuring tube and sodium was $5 \cdot 10^{-4}$ Ω). According to Kozlov [3], the addition of this amount of oxygen ought to have changed the resistance of the tube by $8 \cdot 10^{-6}$ Ω.

Thus our results are in harmony with Claxton [2], but disagree with the assumptions of Blake [1] and the results of Kozlov et al. [3]. The reasons for the disagreement with Kozlov are not clear. To elucidate them, the authors of [3] are carrying out a special investigation.

We measured the resistance of oxygen-free sodium (containing $5 \cdot 10^{-4}$ wt.% O_2) to which hydrogen was being added. The contents of oxygen and other impurities remained constant during the addition of the hydrogen.

The gas space above the surface of the fused sodium was 1/4 the volume of the sodium, and was at the same temperature as the latter. According to Addison [4], the amount of free hydrogen in the gas space in these conditions should not exceed 2-3% of the amount dissolved in the sodium.

The measurement results are plotted in Fig. 1.

Thus the hydrogen content of sodium can be monitored with a sensitivity of $3 \cdot 10^{-5}$ wt.% by measuring its electrical resistance. It is, however, difficult to monitor the oxygen content by this method.

LITERATURE CITED

1. R. Blake, Nucleonic, 19, 66 (1961).
2. K. Claxton, J. Nucl. Engng, A/B, 19, 849 (1965).
3. F. A. Kozlov et al., Teplofizika Vysokikh Temperatur, 3, No. 1 (1965).
4. C. Addison, J. Chem. Soc., January, 116 (1965).

RANDOM THERMOELASTIC STRESSES PRODUCED IN A WALL BY TEMPERATURE PULSATIONS

M. Kh. Ibragimov, V. I. Merkulov, and V. I. Subbotin

UDC 621.039.517.5

During stationary heat exchange with longitudinal turbulent flow of a liquid, temperature pulsations occur in the heat-transmitting wall of the heat exchanger. There are various reasons for this. They include hydrodynamic instability and phase changes of the liquid flow, turbulent temperature pulsations in the liquid flow [1], vibrations of the heat-transfer tubes [2], and others. Because of the temperature pulsations, there are continuous instantaneous and random changes in the temperature gradient along the cross section of the heat-transfer walls. This results in thermal stresses which vary with time and are added to the thermoelastic stresses arising from the action of the average temperature drop (the mathematical expectations of a random temperature field). The effects of the resulting stresses on the serviceability of structural components may be considerable in some cases (high thermal loads, concentration of stresses, corrosive action of the coolant on the structural materials) and must therefore be included in calculations of the fatigue strength.

The present article gives an approximate method for calculating the magnitude of random thermoelastic stresses caused by random pulsations in the temperatures at the boundaries of a solid, T_1 and T_2.

The problem is solved for a thin plate, i.e., it is assumed first, that the field of random temperatures is linearly distributed along the cross section of the plate:

$$T = T_0 + z\theta, \tag{1}$$

and, secondly, that the field of temperatures and stresses depends on one variable, namely, time (the spatial correlation scales are fairly high in comparison with the plate thickness, h). Such an approach is widely used in the solution of nonstationary problems in thermoelasticity [3, 4]. The values of the random temperature T_0 and the random temperature gradient θ at the center of the plate (z = 0) are expressed by the formulas

$$T_0 = \frac{T_1 + T_2}{2}; \quad \theta = \frac{T_1 - T_2}{h}, \tag{2}$$

which follow from the boundary conditions that $T = T_0$ when $z = h/2$ and $T = T_2$ when $z = -h/2$.

Experiments have shown that the temperature pulsations in the wall during turbulent heat exchange have a fairly narrow frequency spectrum (0.05-5 cps) [1]. In this case we may consider the situation to be quasistatic, i.e., we may use the solution of the corresponding stationary thermoelastic problems [4].

As an example, let us consider an infinite plate with fixed edges (Problem I) and freely movable edges (Problem II). In both cases we assume that there is no curvature in the plate. Under these conditions the random stresses are expressed by the formulas [5]:

$$\left.\begin{aligned} P_x^{\mathrm{I}} = P_y^{\mathrm{I}} = -\frac{E\alpha_t}{1-\nu}(T_0 + z\theta), \quad P_{xy}^{\mathrm{I}} = 0; \\ P_x^{\mathrm{II}} = P_y^{\mathrm{II}} = -\frac{E\alpha_t}{1-\nu} z\theta, \quad P_{xy}^{\mathrm{II}} = 0, \end{aligned}\right\} \tag{3}$$

where E is the modulus elasticity, α_t is the coefficient of linear expansion, and ν is the Poisson coefficient.

According to the theory of random functions [6], the dispersion of the sum of two random functions is expressible by the formulas

$$\left.\begin{aligned} \sigma_{P_x}^{2\mathrm{I}} = \sigma_{P_y}^{2\mathrm{I}} = \frac{E^2\alpha_t^2}{(1-\nu)^2}(\sigma_{T_0}^2 + z^2\sigma_\theta^2 + 2z\sigma_{T_0}\sigma_\theta R_{T_0\theta}); \\ \sigma_{P_x}^{2\mathrm{II}} = \sigma_{P_y}^{2\mathrm{II}} = \frac{E^2\alpha_t^2}{(1-\nu)^2} z^2\sigma_\theta^2, \end{aligned}\right\} \tag{4}$$

Translated from Atomnaya Énergiya, Vol. 21, No. 6, pp. 513-514, December, 1966. Original article submitted June 20, 1966.

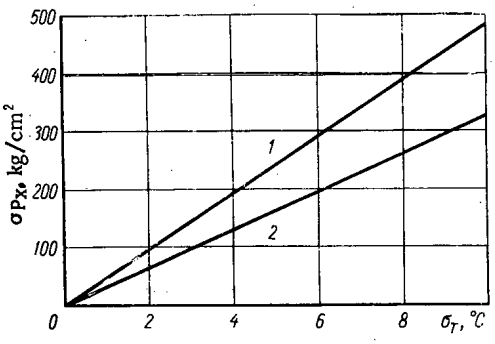

Fig. 1.

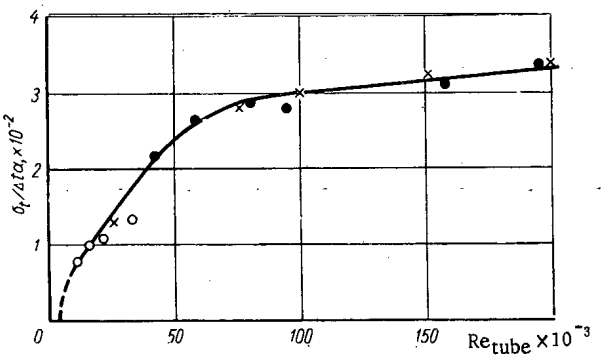

Fig. 2.

Fig. 1. Amplitude of thermal stresses as a function of the intensity of temperature pulsations on the surface of a plate with fixed (1) and free (2) edges.

Fig. 2. Amplitude of temperature pulsations in the wall as a function of Re when heat exchange takes place in a tube [liquid metal (×), water (○)] and when heat is transfered from liquid metal in a double-pipe heat exchanger (●).

where

$$\sigma_{T_0}^2 = \frac{1}{4}(\sigma_{T_1}^2 + \sigma_{T_2}^2 + 2\sigma_{T_1}\sigma_{T_2}R_{T_1T_2});$$

$$\sigma_0^2 = \frac{1}{4}(\sigma_{T_1}^2 + \sigma_{T_2}^2 - 2\sigma_{T_1}\sigma_{T_2}R_{T_1T_2}).$$

Here $R_{T_1T_2}$ is the coefficient of correlation between T_1 and T_2.

The thermoelastic stresses will reach their maximum value on the surface planes of the plate:

$$z = +\frac{h}{2}, \quad \sigma_{P_x}^{I} = \sigma_{P_y}^{I} = \frac{E\alpha_t}{1-\nu}\sigma_{T_1}; \tag{5}$$

$$z = -\frac{h}{2}, \quad \sigma_{P_x}^{I} = \sigma_{P_y}^{I} = \frac{E\alpha_t}{1-\nu}\sigma_{T_2}; \tag{6}$$

$$z = \pm\frac{h}{2}, \quad \sigma_{P_x}^{II} = \sigma_{P_x}^{II} = \sigma_{P_y}^{II} = \frac{E\alpha_t}{1-\nu}\sqrt{\sigma_{T_1}^2 + \sigma_{T_2}^2 - 2\sigma_{T_1}\sigma_{T_2}R_{T_1T_2}}. \tag{7}$$

Figure 1 shows the results obtained by calculating the stress amplitudes by formulas (5)-(7) subject to the conditions that the temperature pulsations in the two planes of the plate, T_1, and T_2, are statistically independent ($R_{T_1T_2} = 0$) and that the amplitudes are equal ($\sigma_{T_1} = \sigma_{T_2}$).

The values of $E\alpha_t$ and ν were taken to be 33 kg/cm^2 and 0.3, respectively. The nature of the temperature pulsations in the heat-transfer wall has been investigated in [1]. Further investigations showed that the pulsation amplitude α_t is a function of the Reynolds number Re and in liquid metals amounts to 3-3.5% of the temperature drop ($t_w - t1$) when Re is large ($> 70.10^3$) (Fig. 2). For heat exchangers we must consider the total temperature drop between the coolants (excluding the temperature drop in the wall). The calculated and experimental results shown in Figs. 1 and 2 enable us to estimate the amplitude of the additional stresses caused in the heat-exchange equipment by the temperature pulsations.

The probability distributions of the amplitudes of the temperature pulsations in the wall — and consequently, of the stress pulsations — practically coincide with the normal law, and therefore the maximum stress pulsations $A_{P\max}$ may exceed the value $2{,}5\sigma_p$ with a probability of 1.5%.

In real energy-loaded systems (heat exchangers, steam generators) operating at the level of allowable thermoelastic stresses, the contribution of the additional stresses may seriously influence the serviceability of structural components.

LITERATURE CITED

1. V. I. Subbotin et al., Énergiya, 18, 525 (1965).
2. C. Peckinpaugh and R. Keaten, Trans. Amer. Nucl. Soc., June, 151 (1964).
3. V. V. Volotin, Prikladnaya Mekhanika i Matematika, 24, 361 (1960).
4. G. Parkus, Transient Temperature Stresses [in Russian], Moscow, Fizmatgiz (1963).
5. V. M. Maizel', A Temperature Problem in the Theory of Elasticity [in Russian]. Kiev, Izd-vo AN USSR (1951).
6. V. S. Pugachev, The Theory of Random Functions and its Application to Automatic Control Problems [in Russian], Moscow, Fizmatgiz (1962).

METHOD FOR CHECKING LEAKTIGHTNESS OF VVR-M REACTOR FUEL ELEMENTS

I. F. Barchuk and D. T. Pilipets

UDC 621.039.547

An efficient technique for checking the leaktightness of fuel elements used in the VVR-M reactor was developed at the Institute of Physics of the Academy of Sciences of the Ukrainian SSR in 1962, and is now in use.

There are quite a few inspection techniques available for the purpose, and they have been reviewed and analyzed by V. I. Polikarpov and associates*. But one drawback common to all of them is the low sensitivity due to low effect/background ratio.

The special feature of this method is that gaseous fission products accumulated in the fuel elements are vacuum-extracted from the nonpressuretight fuel element in large volume, and are then collected and concentrated in a small-volume ionization chamber; the volume ratio is 100:1 in this work. This is a great improvement in sensitivity. The current appearing in the ionization chamber when gaseous products from the fuel element impinge on it acts as a pressuretightness criterion. The current is measured with an automatic recording device. Those fuel elements which give zero readings with the automatic recorder after vacuum has been applied are considered pressuretight. Figure 1 shows the layout of the test arrangement.

The leak monitoring procedure involves four steps:

1. The fuel element to be tested is placed in a vacuum chamber, which is installed in the reactor tank underneath the water level and alongside the core. Pure distillate is pumped into the vacuum chamber, this distillate is diluted and radioactive water entering the vacuum chamber when a fuel element is placed in the chamber goes into the effluent. In this way the system is washed down along with the fuel element surface.

* V. I. Polikarpov et al., Inspection of pressuretightness in nuclear fuel elements, Moscow, State atom press, 1962 [in Russian].

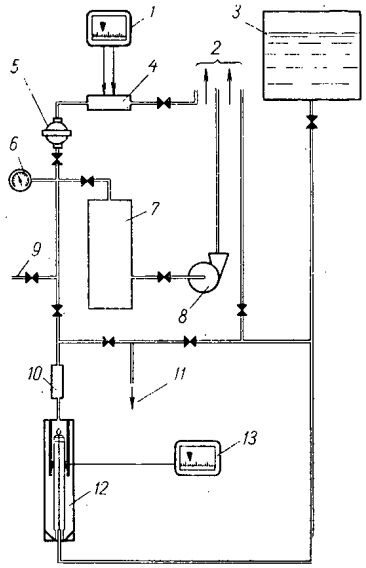

Fig. 1. Layout of test arrangement for monitoring pressure tightness of fuel elements: 1) measurement of ionization current; 2) off to special ventilating duct; 3) distillate tank; 4) ionization chamber (200 cc); 5) filter; 6) vacuum pressure gage; 7) fore-vacuum cylinder (1000 liters); 8) fore-vacuum pump; 9) compressed air line; 10) water-level gage glass; 11) off to special drainage system for effluent; 12) vacuum chamber (18 to 20 liters); 13) fuel-element temperature measurement.

Translated from Atomnaya Énergiya, Vol. 21, No. 6, pp. 514-515, December, 1966. Original article submitted April 7, 1966.

2. Compressed air removes the pure distillate and moisture residue from the system into the effluent system, the ionization chamber and vacuum chamber are purged, and the air is then vented to a special ventilation system. The background in the ionization chamber is measured, and should read zero.

3. Rarefaction in the volume containing the vacuum chamber and ionization chamber is brought about rapidly by means of a constantly evacuated fore-vacuum cylinder, which is disconnected once the required rarefaction is achieved. The fuel element is held for some time at this rarefaction level. If the fuel element jacket is not pressuretight, radioactive gases will escape from the fuel element. The temperature of the vacuum-treated fuel element reaches 75-80°C in 1 h after a reactor on power at 10 MW for a period of some length has been shut down for a week. Thermocouples in contact with the fuel element monitor this temperature inside the vacuum chamber; the automatic recorder measures thermal emf current.

4. Gases extracted from the fuel element are forced into the ionization chamber by the pure distillate, and the ionization current is recorded. On their way to the ionization chamber, the gases also pass through a filter which holds back water vapor and aerosols, whose radioactivity levels and half-lives can be measured if so desired.

A cycle of tests on one fuel assembly lasts about 1 h with the elements held in vacuum for 30 minutes. The arrangement can be operated by a single technician.

URANIUM CONTENT OF CASPIAN SEA SEDIMENTS

G. N. Baturin

UDC 553.495

In connection with the problems of the genesis of uranium deposits in sedimentary rocks, interest has arisen in the processes of distribution and concentration of uranium in present-day sea deposits.

In recent years it has been determined that certain forms of deep-sea deposits of the Black Sea and the Baltic Sea contain up to $(1-3)\cdot10^{-3}$% uranium [1-4], while the concentration of uranium in the waters of these two seas is in the range of $(2-3)\cdot10^{-6}$ g/liter and is practically as low as the uranium content in the waters of the Pacific Ocean [1, 5-7].

Several views were advanced attributing this relatively high uranium content directly or indirectly to the influence of the hydrogen sulfide contained in the water layers of the Black Sea and in the bottom layer of water in the Baltic Sea depressions [1, 7-8]. It may therefore be suggested that hydrogen-sulfide contamination of the lower layers of water is an essential condition for uranium enrichment of sea sediments. However, data on the distribution of uranium in the surface layer of Black Sea and Mediterranean Sea sediments [3] are consistent with the hypothesis that both of these basins are characterized to a greater of lesser extent by sorptive transfer of uranium from the water to the sediments. and the gas content of the water can only affect the rate at which this process takes place. Apparently, in the general case there is a certain sorption equilibrium between the solid and liquid phases, and when there is a high percentage of uranium in the water layer of the basin, we may expect it to be present in the sediments as well, irrespective of the presence of hydrogen sulfide in the water.

The truth of this hypothesis can be tested by considering sediments from the Central Caspian, whose waters contain as much as $6.5-10\cdot10^{-6}$ g/liter of uranium [5] and do not contain any hydrogen sulfide [9, 10].

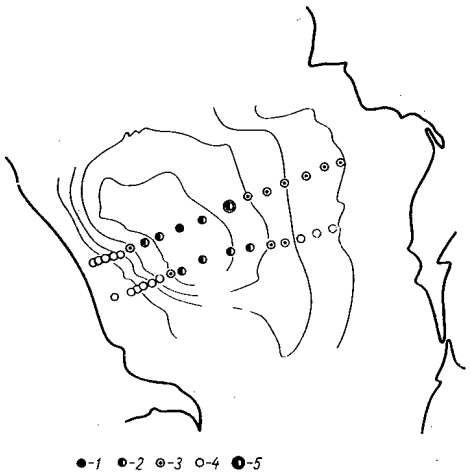

Fig. 1. Distribution of uranium in the surface layer of Central Caspian sediments %: 1) $> 2\cdot10^{-3}$; 2) $(1-2)\cdot10^{-3}$; 3) $(5-10)\cdot10^{-4}$; 4) $< 5\cdot10^{-4}$; 5) site where core was taken.

We found the uranium content of 34 samples taken from the surface layer of Central Caspian sediments. The sediments of the deep-water zone are represented by clayey silts with a low calcium content alternating with clayey-aleuritic and fine-grained aleuritic varieties as the samplings are taken closer to the coast sometimes with an admixture of shell rock (in the eastern zone).

It was found that the sediments under investigation contain $1.0\cdot10^{-4}$ to $2.3\cdot10^{-3}$% uranium. The maximum uranium content values were found in the clayey silts taken from the central part of the Central Caspian basin, and the minimum values were found in the aleuritic silts from the western shelf region (Fig. 1).

According to a well-established general law [11], such a distribution is characteristic for elements migrating in rivers and reaching the sea basin mainly (or largely) in dissolved form. In the present case this law is again confirmed by the uranium content found in 11 suspension samples taken from the arms of the Volga delta from April to June in different years. The ratio of suspended and dissolved uranium in the waters of the Volga is given below:

Average annual turbidity [12]	100 mg/liter
Uranium in solution [5]	$(0.14-1.5)\cdot10^{-6}$ g/liter

Translated from Atomnaya Énergiya, Vol. 21, No. 6, pp. 515-516, December, 1966. Original article submitted June 9, 1966.

Maximum Concentrations of Uranium in Sea Sediments

Sea	Hydrogen sulfide present in the water	Uranium content of water, g/liter	Maximum concentration of uranium in surface layer of of sediments, %
Black	From the 200-m level to the bottom	$(2-3)\cdot10^{-6}$ [5-7]	$2\cdot10^{-3}$ [3]
Baltic	In water near bottom of depressions	Up to $2\cdot10^{-6}$ [1]	$3.2\cdot10^{-3}$ [4]
Central Caspian	None	Up to $10\cdot10^{-6}$ [5]	$2.3\cdot10^{-3}$

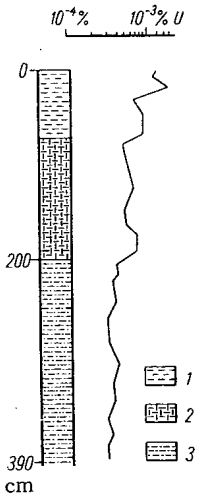

Fig.2. Distribution of uranium in a core: 1) clayey silts (New Caspian deposits); 2) clayey-calciferous silts (New Caspian deposits); 3) aleuritic-clayey silts (deposits from the period of the post-Khvalynskian regression.

Uranium in suspension	$(1.0-2.5)\cdot10^{-6}$ g/g
Fraction of total uranium represented by dissolved uranium	35-90%

As can be seen, dissolved uranium predominates over suspended uranium in the Volga water. In the rivers of the Caucasian coast, which have high turbidity, the relative proportions of suspended and dissolved uranium are apparently reversed. However, since most of the river water coming into the Caspian Sea comes from the Volga (about 80% of the total flow), the percentage of dissolved uranium entering the basin is still considerable.

Because of the many fluctuations in the level of the Caspian Sea during the Late Quaternary period, the question arises: how was this reflected in the uranium content of the sediments and the ratio of dissolved to suspended uranium in the river waters flowing into the basin? The uranium content found in 28 specimens from a core 3.9 m long taken from a depth of 600 m indicates that a high uranium content (5.10^{-4} to 2.10^{-3}%) is characteristic of the entire clayey layer of deep-water New Caspian deposits. In sediments from the lower stratum corresponding to the period of the post-Khvalynskian regression, the aleuritic material is predominant, and the uranium content is reduced to $2.2-4.5\cdot10^{-4}$% (Fig. 2).

Evidently, until the New Caspian period the uranium entered the basin chiefly in the form of detrital particles. Solutions played only a minimum role, and consequently concentration of uranium in the sediments did not take place.

The above data show that when the uranium content of the water is high, the metal may accumulate in the sediment of the basin even when gas conditions are normal (see table).

The conditions necessary for such accumulation apparently also include the presence of silts with a high sorptive capacity and a minimum influx of depleted terrigenous material low in uranium.

In conclusion, the author wishes to express his deep gratitude to A. S. Pakhomova and L. I. Lebedeva, who were kind enough to supply the sediment and suspension samples necessary for this study.

LITERATURE CITED

1. F. Koszy, E. Tomic, and F. Hecht, Geochim. et Cosmochim. Acta, 11, 1-2, 86 (1957).
2. I. E. Starik et al., Dokl. AN SSSR, 139, 1456 (1961).
3. A. V. Kochenov et al., Geokhimiya, No. 3, 302-313 (1965).
4. F. T. Manheim, In the collection: "Questions of Geochemistry and Geochronology of the Ocean"

[in Russian]. Moscow, Mir, p. 107 (1965).
5. I. E. Starik et al., Proceedings of the Radium Institute of the USSR Academy of Sciences, 8, 250 (1958).
6. D. S. Nikolaev et al., Dokl. AN SSSR, 132, 1411 (1960).
7. G. N. Baturin, A. V. Kochenov, and S. A. Kovaleva, Dokl. AN SSSR, 166, 698 (1966).
8. S. Sh. Agamirov, Geokhimiya, No. 1, 92 (1963).
9. S. V. Bruevich, Hydrochemistry of the Central and Southern Caspian [in Russian], Moscow, Izd-vo AN SSSR (1936).
10. M. V. Fedosov, Proceedings of the All-Union Scientific Research Institute of Sea Fishing and Oceanography [in Russian], Vol. 38, No. 1, Moscow, Pishchepromizdat, p. 5 (1959).
11. N. M. Strakov, Principles of Lithogenesis, Vols. 1 and 2, Consultants Bureau, N. Y. (1967).
12. G. V. Lopatin, Alluvia of the Rivers of the USSR [in Russian], Moscow, Geografgiz (1952).

A MATRIX METHOD FOR CALCULATING α-RAY SPECTRA OF THICK SOURCES

V. P. Grigorov

UDC 543.52:539.128.4

We shall use the term "thick source" to mean a source consisting essentially of a specific inactive substance inside which atoms of an active isotope emitting monoenergetic α particles are distributed with a density A' (h) according to a known law. The source thickness H_0 is comparable to but not greater than the path length R_0 of an α particle in the source material (we neglect the mass of the isotope). The active atoms are uniformly distributed over the area.

If we regard the α radiation as isotropic and neglect the reflection of α particles and the slight boundary effect, we can easily calculate from the geometry of the changes involved the relative number N of α particles emitted by the source:

$$N=\frac{1}{2}\int_0^{H_0} A(h)\,h\int_h^{R_0}\frac{1}{r^2}\,dr\,dh, \tag{1}$$

where

$$A(h)=\frac{1}{\int_0^{H_0} A'(h)\,dh}\,A'(h).$$

We divide the path length R_0 of an α particle in the source material into m segments, Δr_i $(R_0=\sum_{i=1}^{m}\Delta r_i)$, and divide the source into k layers of thickness $\Delta h_j (H_0=\sum_{j=1}^{k}\Delta h_j$, each $(k\leq m)$. We must have $\Delta r_l=\Delta h_l$. We introduce the notation

$$h_j=\sum_{l=1}^{j}\Delta h_l;\quad r_i=\sum_{l=1}^{i}\Delta r_l;\quad r_0=h_0=0. \tag{2}$$

It is evident that $h_j=r_j$.

We replace the integral in formula (1) by a sum:

$$N=\frac{1}{2}\sum_{j=1}^{k}\int_{h_{j-1}}^{h_j} A(h)\,h\int_h^{R_0}\frac{1}{r^2}\,dr\,dh. \tag{3}$$

The relative number $N(r_i)$ of α particles which have travelled a path length of r_{i-1} to r_i in the source (where i is some fixed value) is

$$N(r_i)=\frac{1}{2}\sum_{j-1}^{i-1}\int_{h_{j-1}}^{h_j} A(h)\,h\,dh\int_{r_{i-1}}^{r_i}\frac{dr}{r^2}+\frac{1}{2}\int_{h_{j-1}}^{h_i} A(h)\,h\int_h^{r_i}\frac{dr}{r^2}\,dh=\sum_{j=1}^{i-1} A(\bar{h}_j)\,\frac{h_{j-1}+h_j}{r_{i-1}r_i}\,\Delta h_j\Delta r_i+\frac{1}{4}A(\bar{h}_i)\,\frac{\Delta h_i^2}{r_i}, \tag{4}$$

where $\bar{h}_{j-1}$ and $\bar{h}_i$ are average values over the intervals $[h_{j-1}, h_j]$ and $[h_{i-1}, h_i]$. In order to use formula (4), we must know these values. The fundamental approximation of the calculation method under consideration consists in the assumption that the average values $\bar{h}_j$ coincide with the midpoints of the segments, i. e.,

$$\bar{h}_j=\frac{1}{2}(h_{j-1}+h_j).$$

If we give the index i different values from 1 to m, we obtain m equations analogous to Eq. (4); the solutions of these equations together constitute a discrete spectrum of α particle path lengths in the

Translated from Atomnaya Énergiya, Vol. 21, No. 6, pp. 517-518, December, 1966. Original article submitted March 17, 1966.

Elements of the Matrix B

i	Values of j						
	1	2	3	4	5	6	...
1	0.250000	0	0	0	0	0	
2	0.125000	0.125000	0	0	0	0	
3	0.041667	0.125000	0.083333	0	0	0	
4	0.020833	0.062500	0.104167	0.062500	0	0	
5	0.012500	0.037500	0.062500	0.087500	0.050000	0	
6	0.008333	0.025000	0.041665	0.058333	0.075000	0.041667	
...	...	...	...	...	...	...	...

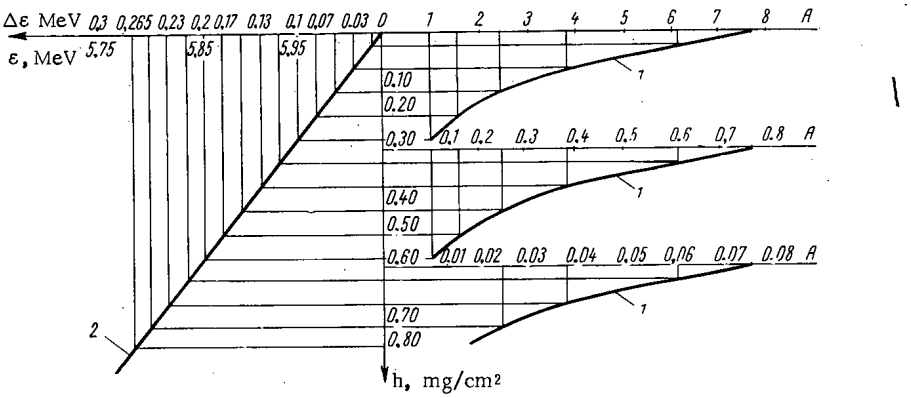

Fig. 1. Auxiliarygraph for calculating the elements a_j of the matrix A: 1) variation of distribution density as a function of the depth A (h); 2) variation of residual energy of the α particles of ThC (6.05 MeV) as a function of their path length in the air-equivalent substance of the source (ε is the energy of the α particles).

source material. It is easily shown that this set of equations can be written in the form of a single matrix equation

$$N = BA, \tag{5}$$

where N and A are column vectors consisting of m and k elements, respectively, while the elements b_{ij} of the matrix B, calculated for specific values of Δh_j and Δr_i, are of the form

$$b_{ij} = \begin{cases} \frac{1}{4}\frac{h_{j-1}+h_j}{r_{i-1}r_i}\Delta h_j \Delta r_i & j < i; \\ \frac{1}{4}\frac{\Delta h^2}{h_i} & j = i; \\ 0 & j > i. \end{cases} \tag{6}$$

To facilitate the subsequent transition from the spectrum of α particle path lengths $N(r_i)$ to the α particle energy spectrum (where we must take into account the variation of the residual energy of the α particle as a function of their path length in the source material), all the segments Δh_j and Δr_i should be taken equal to an arbitrary and sufficiently small "energy" unit (say, 0.02 or 0.05 Mev), i.e., using the above relationship, we should divide H_0 and R_0 into segments in such a way that on each of these segments an α particle will lose the same amount of energy, equal to the energy unit. We take $\Delta h_j = \Delta r_i = 1$, and formula (6) becomes

$$b_{ij} = \begin{cases} \frac{2j-1}{4i(i-1)} & j < i; \\ \frac{1}{4i} & i = j; \\ 0 & j > 1. \end{cases} \tag{7}$$

Part of the matrix B is shown in the table.

When we use this calculation method in practice, we first determine the elements a_j of the matrix A, using an auxiliary graph (for example, the one shown in Fig. 1). The energy axis is divided into segments equal to the chosen energy unit (e.g., 0.02 MeV), and then, using curve 2, we divide the depth axis (the h-axis) into segments corresponding to the energy intervals. From the graph of A(h) (see curve 1) we determine the activity $A(h_j)$ at each point corresponding to the midpoint of the energy interval; we then multiply the resulting values by the width of the interval in mg/cm^2, obtaining the desired elements a_j. The matrix B is multiplied by the resulting matrix A; as a result, we find the matrix N, which is the desired energy spectrum of the α particles.

The precision of the calculations depends on the precision of the geometric construction and the form of the function A(h). If the value of A(h) doubles within one segment Δh_j, the discrepancy between the exact and the approximate data may amount to as much as 8-10%.

It is readily seen that when the distribution density curve varies greatly in segments corresponding to the upper part of the source, the α particle spectrum may be calculated in sections, with a smaller energy unit used in the section made up of these segments.

The matrix B may be set up in such a way that it will be applicable when the angle between the normal to the source surface and the direction of emission of the α particle does not exceed θ. For each depth h_j there is a maximum path length $r_{j\,max}$:

$$r_{j\,max} = \frac{\bar{h}_j}{\cos\theta}. \tag{8}$$

The number of elements in each column of the matrix B is limited and is equal to the number of energy intervals corresponding to $r_{j\,max}$.

The sensitivity function of the spectrometric apparatus (the instrument function), which we use for the transition from the α particle path length spectrum $N(\varepsilon)$ to the pulse amplitude spectrum J(E), may be expressed in the form of a matrix G, each element of which g_{ik} of which represents the relative number of pulses hitting the analyzer channel with discrimination levels from E to $E + \Delta E$ produced by α-particles with energies in the interval from ε to $\varepsilon + \Delta\varepsilon$. The desired pulse amplitude spectrum can be expressed by the matrix equation

$$J = GN = GBA. \tag{9}$$

If the function $G(\varepsilon, E)$ is expressed analytically, e.g., by a Gaussian distribution, then the elements g_{ik} can be calculated. If they are determined experimentally, by using, e.g., thin sources of α particles of various energies or by changing the amplification factor of an amplifier, the use of a matrix will be particularly convenient.

Summing specific elements of the matrix N or J, we can easily calculate the number of α particles which have energies in specific intervals, or the number of pulses whose amplitude lies within the limits determined by the discrimination level.

MEASUREMENT OF THE DOSE OF PRODUCTS OF THE NUCLEAR REACTION $B^{10}(n, \alpha)Li^7$ AND THE TEMPERATURE IN THE REACTION ZONE WHEN THERMAL NEUTRONS ACT ON BORATE GLASSES

S. A. Gabsatarova and A. M. Kabakchi

UDC 614.8:539.12.04

Interest has recently arisen in the use of doses of absorbed neutrons for vulcanizing rubber [1], "spot-welding" various polymer materials [2], and other purposes [3, 4]. To increase the dose in the reaction medium, salts of boron and lithium are added.

In this letter we describe calculations and experimental measurements of the energy transmitted to the medium by the α-particles and Li^7 nuclei created by the action of thermal neutrons on borate glass (containing 16.5% B_2O_3). The dose rate was calculated for n-heptane for the conditions of radiation-thermal cracking.

The optimum thickness for the "operative" layer emitting α particles was taken as equal to the path length of the α particles in the glass. A numerical value of the path, 1.15 mg/cm^2, was taken for mica [5], which is similar to the glass in chemical composition and density. To determine the irradiation intensity of the whole α particle spectrum we found the mean energy of the α particles for each of ten equal and parallel sublayers into which the operative layer was divided. The determination was carried out by graphical integration of the curves plotting α particle energy versus path length for a large number of angles increasing from 0 to φ^0. Figure 1 shows one of these curves. The irradiation intensity was calculated [7] from the relation

$$P = \pi\sigma N_\alpha E_\alpha,$$

where π is the flux density of thermal neutrons, equal to $1.12 \cdot 10^{11}$ neutr/cm^2·sec, σ is the effective cross section, which for boron is $7.55 \cdot 10^{-22}$ cm^2 [6], N_α is the number of α particles formed in each of the sublayers within the angle φ, and E_α is the mean energy of these particles in eV.

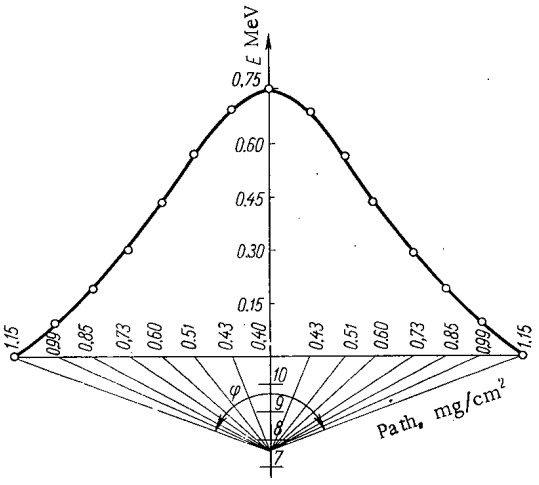

Fig. 1. α-particle energy versus path length for seventh sublayer.

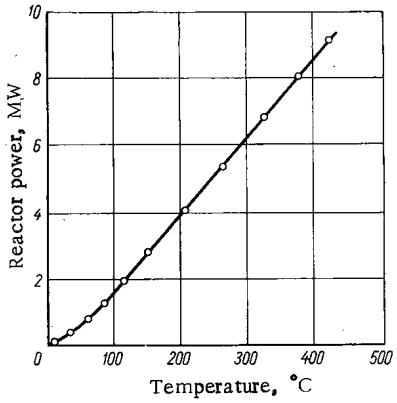

Fig. 2. Temperature developed inside capsule, plotted versus reactor power.

Translated from Atomnaya Énergiya, Vol. 21, No. 6, pp. 519-520, December, 1966. Original article submitted May 31, 1966.

TABLE 1. Calculated Values of Energy Transmitted to Substance by α Particles

Number of sub-layer	Angle φ degrees	$N_\alpha, \times 10^{-18}$ cm^{-2}	$E_{\alpha av}, \times 10^{-5}$ (eV)	P, $\times 10^{-13}$, (eV/cm^2·sec)
1	36	0.329	0.19	0.0526
2	65	0.592	0.577	0.289
3	83	0.757	0.088	0.688
4	100	0.915	1.61	1.24
5	114	1.04	2.22	1.95
6	127	1.16	2.88	2.82
7	140	1.28	3.54	3.83
8	151	1.38	4.52	5.26
9	163	1.49	5.36	6.74
10	175	1.60	5.55	7.50
				$\Sigma P = 3.04 \cdot 10^{14}$

TABLE 2. Calculated Values of Energy Transmitted to Substance by Recoil Li^7 Nuclei

Number of sub-layer	Angle φ degrees	$N_{Li^7}, \times 10^{-18}$ cm^{-2}	$E_{Li_{av}}, \times 10^{-5}$ (eV)	P, $\times 10^{-13}$ (eV/cm^2·sec)
4	48	0.438	0.468	0.173
5	78	0.715	0.646	0.390
6	102	0.931	1.100	0.865
7	122	1.120	1.640	1.540
8	138	1.260	2.140	2.270
9	156	1.430	2.770	3.340
10	173	1.580	3.170	4.230
				$\Sigma P = 1.28 \cdot 10^{14}$

TABLE 3. Results of Experiments to Determine Absorbed Doses

Number of plate	Glass	$D_1 \times 10^{-5}$ rad	$D_2 \times 10^{-5}$ rad	$(D_1 - D_2) \times 10^{-5}$ rad
1	Borate	15.78		7.22
2	"	15.82		7.29
3	"	15.79		7.27
4	"	15.73		7.20
5	"	15.77		7.22
6	Quartz		8.52	
7	"		8.54	

Similarly we calculated the energy emitted from the surface by lithium nuclei. The results are given in Tables 1 and 2. The absorbed dose rate in a capsule with an internal surface of 10 cm^2 containing $1.55 \cdot 10^{-2}$ g heptane was calculated from the data in Tables 1 and 2 for the chosen thermal neutron flux: it was found to be $4.47 \cdot 10^3$ rad/sec.

To check these calculations we carried out dosimetric experiments in one of the experimental holes of the VVR-M Reactor of the Institute of Physics of the Ukrainian Academy of Sciences. The dosimeters were plates of polyvinyl alcohol colored with methylene blue [8]. When the plates are irradiated in a capsule of boron-containing glass, γ-neutron radiation from the nuclear reactor and the products of the reaction $B^{10}(n, \alpha)Li^7$ both act on the plate, whereas on irradiation in a quartz capsule only the γ-neutron radiation from the reactor acts: the energy of the products of the nuclear reaction was found by subtracting the dose acquired by the plates in the second case, D_2, from that acquired in the first case, D_1. The flux density of the thermal neutrons was $1.12 \cdot 10^{11}$ neutr/cm^2·sec and the duration of irradiation was 30 min, giving partial decolorization of the plates. The thermal-neutron flux was registered by means of radioactive indicators with gold foils and cadmium filters; the intensity of coloration and thicknesses of the plates were measured by means of an SF-4 spectrophotometer and an MBI-8m microscope. Table 3 gives the experimental data: the results will be seen to be highly reproducible.

The mean dose rate for plates of polyvinyl alcohol, calculated from the experimental data, was found to be $4.02 \cdot 10^3$ rad/sec; on conversion to n-heptane, allowing for the difference in the electron densities of heptane and polyvinyl alcohol, it was $4.51 \cdot 10^3$ rad/sec. The agreement between the calculated and measured dose rates confirms the validity of the calculations.

Calculations showed that an appreciable part of the kinetic energy of the α particles and Li^7 nuclei was converted in the vessel walls to heat; as a result, the irradiated substance may become heated to the

temperature required for radiation-thermal cracking. We performed experiments to determine the temperature in the capsule, using a chromel-alumel thermocouple and the same experimental hole in which the dosimetric experiments were performed: we found that the temperature can easily be regulated by varying the reactor power. Figure 2 plots the results of one of the temperature experiments: it will be seen that there is a linear relation between the temperature and the reactor power in the range from 250 to 450 °C, which is of interest for radiation-thermal cracking.

LITERATURE CITED

1. H. Anderson, J. Polymer Sci., 43, 59 (1960).
2. I. M. Barkalov et al., Proceedings of Second All-Union Conference on Radiation Chemistry, Moscow, Izd. AN SSSR, p. 616 (1962).
3. E. N. Avdonina and An. N. Nesmeyanov, Dokl. AN SSSR, 154, 851 (1964).
4. An. N. Nesmeyanov et al., Radiokhimiya, 4, 116 (1962).
5. S. Gordon and E. Hart, Rad. Res., 15, 440 (1961).
6. Atlas of Effective Neutron Cross Sections of the Elements, Moscow, Izd. AN SSSR (1955).
7. M. I. Shal'nov, Tissue Dose of Neutrons, Moscow, Gosatomizdat (1960).
8. Ya. I. Lavrentovich et al., Atomnaya Énergiya, 19, 273 (1965).

A QUASISTATIONARY CALORIMETRIC METHOD OF DOSIMETRY FOR HIGH FLUXES OF IONIZING RADIATION

V. M. Kolyada, V. S. Karasev, and K. S. Pedchenko

UDC 536.629

Calorimetric methods of reactor radiation dosimetry have developed greatly in recent times. This is true not only because they can be used for obtaining valuable information on the interaction of radiation with various materials but also because only limited opportunities exist for the use of ionization, chemical, and other methods of dosimetry for measurements in the active zone of a reactor. The latter factor becomes decisive in work with modern high-flux reactors of the VVR-M, SM-2, or VR-2 type, and even more for the reactors now being planned, with a neutron flux of more than 10^{15} thermal neutrons/cm^2·sec [1], where the energy generated in the nonfissionable materials amounts to tens of watts per gram.

The adiabatic [2, 3] and kinetic [4-6] methods used today have inherent temperature limitations. The adiabatic method requires complete thermal isolation of the specimen from the external surroundings, which is difficult to achieve for temperature increase rates of more than 100°C/min [7]. The kinetic method is based on the hypothesis that the temperature increases as an exponential function of time, but this is valid only at low temperatures.

Isothermal calorimeters [8-10] are capable, in theory, of operating in fields of arbitrarily high intensity. However, precise dosimetry requires high-powered electric heaters, thermocouple systems, high-temperature insulation, and radiation shielding, which makes it quite difficult to use them when large amounts of heat are being generated under the limited-volume conditions of the experimental channels.

The VVR-M reactor was equipped for a long time with an isothermal calorimeter which had electrical compensation for the heat generated in the specimen being investigated [11], and this made it possible to determine within 3-5% the amount of energy absorbed in specimens of various dimensions [12]. However, the measurements were made at reactor power values below the nominal value, because of the high density of heat generation in the materials of the calorimeter and the specimen.

In order to raise the upper limit of the measurements, we devised a quasistationary calorimetric method based on the known physical phenomenon that a specific amount of heat is isothermally absorbed (or emitted) when a crystalline solid melts (or crystallizes) (Fig. 1).

If a crystalline solid placed in the experimental channel with a constant wall temperature (T_W=const) is melted by the energy absorbed from the reactor radiation, then evidently the length of the melting plateau (the melting time) (see region 2 in Fig. 1) will be directly related to the magnitude of the absorbed dose by the simple formula

$$Q=\frac{\lambda m}{\Delta\tau}+k, \tag{1}$$

where Q is the radiation energy absorbed per unit time in the calorimeter; λ is the heat of fusion; m is the mass of the working medium; $\Delta\tau$ is the melting time of the working medium determined from the diagram; k is the heat loss of the calorimeter per unit time under isothermal conditions ($T_m - T_W$=const).

Equation (1) contains two unknown quantities, Q and k.

If Q_i is the energy absorbed per unit time for a reactor power N_i, then for small variations in power we have

$$\frac{Q_1}{Q_2}=\frac{N_1}{N_2}=n, \tag{2}$$

which enables us to determine Q_1 and Q_2.

Translated from Atomnaya Énergiya, Vol. 21, No. 6, pp. 520-522, December, 1966. Original article submitted April 14, 1966.

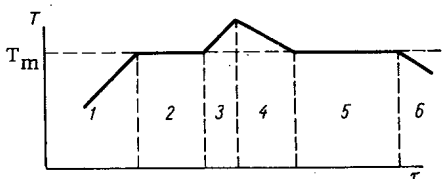

Fig. 1

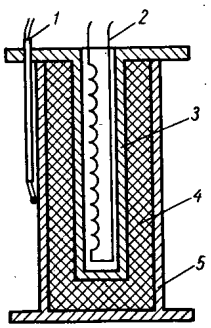

Fig. 2

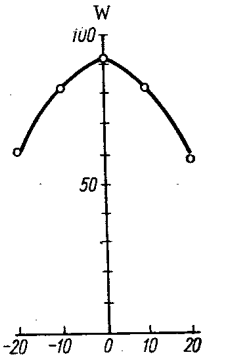

Fig. 3

Fig. 1. Melting-crystallization diagram.

Fig. 2. Quasistationary calorimetric instrument: 1) thermocouple; 2) electric heater; 3) tube for specimen; 4) working medium; 5) thin-walled shell.

Fig. 3. Dependence of the magnitude of the absorbed energy in the calorimeter on the height of the channel (8MW).

For experiments in low-energy channels, where the radiant power is insufficient to melt the working medium, we can determine the absorbed energy from the process of cooling of a working medium whose temperature has been previously raised into the liquid phase by means of a heater (see regions 4, 5, and 6 in Fig. 1).

The quantities Q found by the above method are the sums of the energies absorbed per unit time in the specimen under investigation and in the calorimeter. The latter is easily found by means of a special experiment without a specimen.

A second way of determining the absorbed energy by the quasistationary method requires no changes in reactor power and permits us to measure the absorbed energy directly in the specimen itself. Let the temperature of a calorimeter placed in the irradiation zone without a specimen, under stationary thermal conditions, be somewhat less than the T_m of the working medium. This is relatively easy to achieve by selecting our working medium and heat exchange conditions properly (by using the geometry of the calorimeter, insulation, etc.). If we introduce the specimen under investigation, the heat generated in it will be consumed in melting the working medium and heating it in the liquid phase. If we then remove the specimen from the calorimeter, the temperature of the latter will drop to the initial value ($T < T_m$). In accordance with the resulting melting-crystallization diagram, we set up the system of equations:

$$\left.\begin{aligned} Q_{\text{calor}} + Q_{\text{sp}} &= \frac{\lambda m}{\Delta\tau_1} + k; \\ Q_{\text{calor}} + \frac{\lambda m}{\Delta\tau_2} &= k. \end{aligned}\right\} \qquad (3)$$

Subtracting the second equation from the first, we obtain a value for the radiant energy absorbed per unit time in the specimen.

The calorimetric measurements were made in a vertical channel situated in the beryllium reflector of the reactor (flux density 10^{14} thermal neutrons/cm^2·sec). The experimental apparatus — the quasistationary calorimeter (Fig. 2) — consisted of a thin-walled aluminum shell with centered boreholes, the working medium (tin), a tube containing the heater, and the thermocouples. The stationary temperature, established in the calorimeter at maximum reactor power (8 MW), was less than the melting point of the working medium (232°C). This was done in order that we might test the above-described methods of determining the absorbed energy from the melting time and crystallization time of the working medium and at the same time experimentally determine the error in the measurements, by finding the power of the electric heater by means of electrical measuring instruments and using the simple equations (3). To melt working medium, we applied additional heat by means of an electric heater.

The measurements were made at reactor power values of 6.5 MW and 8 MW, and the calorimeter was shifted along the height of the channel. The melting-crystallization diagrams were recorded with an ÉPP-09M recorder moving at 1440 mm/h.

The measured and calculated data are given below and in Fig. 3:

Melting time of working medium at reactor power of 8 MW and electrical power of 60 W	72 sec
Crystallization time of working medium at reactor power of 8 MW	120 sec
Melting time of working medium at reactor power of 6.5 MW and electrical power of 82 W	64 sec
Crystallization time of working medium at reactor power of 6.5 MW	68 sec
λm	2870 J
Power of electric heater, calculated from melting time and crystallization time at reactor power of 8 MW	63.6 W
Deviation from value obtained with instruments	$\frac{63.6-60}{60}\cdot 100 = 6\%$
Power of heater, calculated from melting time and crystallization time at reactor power of 6.5 MW	87 W
Deviation from value obtained with instruments	$\frac{87-82}{82}\cdot 100 = 6.1\%$
Absorbed radiant energy in the calorimeter, calculated from crystallization time at reactor power values of 8 MW and 6.5 MW	12.2 W/MW
Absorbed radiant energy in calorimeter, calculated from melting time at reactor power values of 8 MW and 6.5 MW	11.4 W/MW
Deviation from average value	$\frac{12.2+11.4}{2} = 11.8 \pm 0.4(3.4\%)$

The results obtained in calculating the energy absorbed in the calorimeter on the basis of the isothermal melting time and crystallization time agree to within ±3.4%, and the results of the heater power calculations on the basis of electrical measuring instruments and the melting-crystallization diagram agree to within 6%. This error can be reduced by using a faster recorder speed.

Thus, in contrast to the present methods of calorimetric dosimetry, the quasistationary method enables us to specify the desired measuring temperature by selecting the appropriate working medium for the calorimeter. This enables us to avoid the high temperatures that arise in the channels of the active zone.

Electrical calibrating heaters are widely used both in adiabatic and in isothermal methods, and this makes the design and operation of the instruments a good deal more complicated. In the method proposed here, there is no need to use such heaters.

An important difference between the quasistationary method and the adiabatic and isothermal methods is that the requirements imposed on the temperature sensor are considerably simplified and reduced; a single thermocouple, which does not require calibration, serves as the sensor in this method, and there is no experimental error due to changes in readings produced by irradiation and other factors.

The quasistationary calorimetric method of reactor radiation dosimetry is simple and highly reliable and yields results with a good accuracy over a wide range of radiation intensities; the upper limit of measurement is practically unbounded, and this is achieved by using substances with the necessary melting points and heats of fusion as the working medium in the calorimeter.

LITERATURE CITED

1. V. V. Goncharov, Report No. 296, presented by the USSR at the Third International Conference on the Peaceful Uses of Atomic Energy (Geneva, 1964).
2. A. Anderson and R. Waite, J. Sci. Instrum., 33, 46 (1956).
3. M. V. Fiveiskii et al., Atomnaya Énergiya, 9, 321 (1960).
4. A. Rurtcher and A. Petschnik, Atompraxis, 9, No. 7 (1963).
5. F. Binford, Nucleonics, 15, 93 (1957).
6. B. Radak et al., Bull. Inst. "Boris Kidrich", Vol. 12, p. 7 (1961).

7. A. Anderson and J. Lainker, Collection of Reports from a Symposium on Various Questions of Dosimetry [Russian translation], Moscow, Gosatomizdat (1962).
8. N. F. Pravdyuk et al., Atomnaya Énergiya, 9, 380 (1960).
9. D. M. Richardson, In the collection "Dosimetry of Ionizing Radiation" [Russian translation], Moscow, Gostekhteorizdat (1966).
10. F. Ayela et al., Bull. inform. sci. and tech., No.82, April (1964).
11. V. S. Karasev and V. M. Kolyada, Atomnaya Énergiya, 19, 74 (1965).
12. V. M. Kolyada and V. S. Karasev, Atomnaya Énergiya, 19, 532 (1965).

FIRST SYMPOSIUM ON LOW-TEMPERATURE PLASMA GENERATORS

B. A. Uryukov

A symposium devoted to research on the properties of the electric arc, its interactions with electrodes, gas streams, and magnetic fields in low-temperature MHD generators, was held July 4-9, 1966, at the Institute of Theoretical and Applied Mechanics of the Siberian Division of the USSR Academy of Sciences (Novosibirsk). The symposium attracted 120 representatives of nearly 50 organizations from over 10 cities throughout the nation. Forty nine papers were read and discussed. The papers submitted encompassed the following topics: 1) theoretical research on interactions between an electric arc and a gas stream and externally applied magnetic field; 2) dimensionless criteria for characterizing the performance of low-temperature plasma generators; 3) experimental research on the electric arc operating under forced heat-transfer conditions; 4) arc transients; 5) electrode sheath effects in high-pressure arcs, electrode spot motion mechanisms, electrode erosion; 6) investigation of breakdown phenomena in a gas stream.

The symposium showed that significant progress has been made in the study of arc combustion in the year elapsed since the Second All-Union Conference on Low-Temperature Plasma Generators (see Atomnaya Énergiya, 19, No.6 (1965)). The number of papers dealing with theoretical arc calculations under stabilized container wall and gas stream conditions increased noticeably. A trend toward semiempirical theories was marked in the treatment of dimensionless criteria. There was heightened interest in the study of plasmotrons featuring magnetic arc stabilization. Experimental research on physical processes at work in the arc column has been expanded. Papers appeared on the structure of electrode sheath processes. The symposium took note of the importance of engineering developments in new advanced designs of plasma heaters for concrete applications. Work on plasmotrons with rising voltage-current characteristics could produce profitable cost dividends, considering the possibility of lossless performance with ballast resistors.

The resolution adopted by the symposium noted at the same time that physical processes occurring in the arc column, and the subject of arc-stream and arc-electrode interaction have not been studied adequately to date. For instance, the quality of theoretical work on arc calculations in a gas stream leaves much to be desired. The range of similitude criteria studied with reference to plasmotron performance is still too meager for any confident predictions of plasmotron performance at levels of interest to industry. Physical experimentation techniques for studying high-pressure arc column processes are still rudimentary. The mechanism behind breakdown development between arc and electrode in plasmotrons and the relationship between heat input to electrodes by surface heating in electrode spots and Joule heating in the interior of the electrodes remain obscure. The effect of the nature of the electrode material and of surface chemical reactions on electrode erosion has been given insufficient study.

A paper presented by A. T. Onufriev and V. G. Sevast'yanenko (ITAM), "Transfer of radiant energy in spectral lines, with allowances for reabsorption," describes an approximate method for calculating radiative energy transfer in a spectral line (or in a system of lines) when the temperature and frequency dependences of absorptivity are important. The spectral range is divided into several intervals within each of which the absorptivity is frequency-averaged

$$k = \left(\frac{\int_{\nu_1}^{\nu_2} k_\nu \, d\nu}{\int_{\nu_1}^{\nu_2} \frac{1}{k_\nu} \, d\nu} \right)^{1/2},$$

Translated from Atomnaya Énergiya, Vol.21, No.6, pp.523-525, December, 1966.

where k is the average absorptivity; k_ν is the local absorptivity at frequency ν ; $\nu_2 - \nu_1$ is the frequency interval in question. This method is highly accurate using a small number of spectral subintervals.

Reports by M. E. Zarudi and I. S. Edel'baum (All-Union Research Institute for Electrothermal Equipment), "Stepwise approximation of temperature profiles and characteristics of channel arcs for argon, nitrogen, hydrogen, helium, and air," and "Electrical arc column calculations in a channel with radiation taken into account" (M. E. Zarudi), discussed methods for wall-stabilized electric arc calculations. The approach involves breaking up the arc combustion channel into several intervals within which the properties of the material (thermal conductivity, electrical conductivity, emissivity) will be temperature-independent. The problem reduces mathematically to solving a system of algebraic equations in which the electric-field intensity appears as the unknown.

G. I. Kozlov (Institute of Problems in Mechanics) studied a model of an arc stabilized by axial gas flow. Assuming that Meeker's theory holds in the region occupied by the arc, he determined the characteristics of the nonconducting region and the arc diameter downstream in the gas. A similar theory was developed by A. B. Kuvaldin and M. Ya. Smelyanskii (Moscow Power Institute), in the paper "Conversion of voltage-current characteristics of an arc swept by a laminar flow." They also delineated the range of applicability of the method (in the case of air, the theory is valid to currents of 1000 A). A paper by A. M. Kruchinin (Moscow Power Institute), "Results of a study of an automatic current stabilization system for electric-arc gas heaters," was devoted principally to the transient period of the thermal equilibrium in an arc swept by longitudinal flow. The arc combustion region is broken up into a laminar conducting region and a nonconducting region with developed turbulence, and an attempt is made to deal with the effect of gas swirling. The dynamic properties of the plasmotron are handled as a controlled system. A high-speed contactless automatic stabilizer designed on the basis of this theory aids stable combustion of an arc supplied from a controlled rectifier with a smoothing choke and with no ballast resistor in the arc circuit. Results of the study were checked out on 50 kW and 1000 kW plasmotron units. The automatic system with close-to-optimum parameters provides excellent arc current stabilization.

A report by S. S. Kutateladze et al. (Institute of Heat Transfer Physics, Siberian Division of the USSR Academy of Sciences), "Dimensionless criteria for characteristics of low-temperature plasma generators," discussed the relationship between the thermal efficiency of plasmotrons and the plasmotron performance parameters, on the basis of the relationship between Stanton number and Reynolds number in heat transfer with a flat plate in a laminar stream. Possible departures from the law as a result of nonisothermal flow, breakdown conditions, and other effects were analyzed. Experimental data on thermal efficiency, relating to argon at pressures to 30 mm Hg, were generalized in the light of the dependence between efficiency, Reynolds number ($0.4 \cdot 10^3$ to $9.4 \cdot 10^3$ range), and mean free path length ($2 \cdot 10^{-5}$ to $4.6 \cdot 10^{-3}$ cm). Note that the mass-average temperature at the plasmotron exit was taken to be a decisive factor.

"Electric arc in argon and cesium stream in the presence of a magnetic field" by V. Yu. Baranov and K. N. Ul'yanov (V. I. Lenin All-Union Electrical Engineering Institute), and "Experimental investigation of the effect of a magnetic field on an electric arc in the presence of gas flow" by A. F. Vitshas et al. (I. V. Kurchatov Institute of Atomic Energy) were papers of interest from the vantage point of gaining an understanding of the physics underlying the combustion process of an arc immersed in transverse flow in a magnetic field. The possibility of the arc glowing in "sweepthrough" flow when molecules of streaming gas pass through the arc, and in "sweep-around" flow when heavy particles are slowed down in the arc, as well as the possible existence of a pulsed breakdown mode in which the arc extends periodically in loops along the flow and becomes shunted, were demonstrated. Critical magnetic field and gas pressure values at which the arc combustion mechanism undergoes changes were determined both theoretically and experimentally. The possible use of an arc in a magnetic field as the pre-ionizer in a nonequilibrium MHD generator and as a plasma generator component was also discussed.

"Experimental investigation of physical processes in an electric arc moving in response to a magnetic field" by V. K. Ivanov discussed probe measurements of the principal conduction zone of an arc moving between parallel electrodes immersed in atmospheric air. This zone is situated in the front of the arc and has appreciable current densities. "Investigation of a dc coaxial plasmotron" by V. S. Kisel' et al. (ITAM) described operational features of a plasmotron consisting of coaxial electrodes with a longitudinal magnetic field over a wide range of gas flowspeeds. At low gas flowspeeds (below 15 m/sec),

an increase in applied magnetic field means higher field intensity across the arc, but the effect of the magnetic field is reversed at higher flowspeeds. Axial gas flowspeeds were studied up to 100 m/sec.

Several papers were devoted to measurements of temperature profiles in arcs swept by longitudinal flow. V. M. Gol'dfarb and A. M. Uzdenov (Leningrad A. I. Gertsen State Pedagogical Institute) described electron temperature and heavy particle temperature variations in an argon burner of fixed arc length, in "Temperature of electrons and heavy particles in an arc with axial argon flow." The gas temperature was determined calorimetrically, and the electron temperature was determined by monochromatic photometry. In agreement with already published results, it was shown that the electron temperature is higher than the temperature of the heavy particles, while the difference between the temperatures narrows down as the current is stepped up, as the gas flowrate is lowered, or as the plasmotron nozzle is taken further off the axis of the arc. The time to reach equilibrium was estimated. "Temperature field of an argon arc" by R. S. Bobrovskaya (All-Union Res. Inst. for Electrothermal Equipment) discussed measurement of the temperature field of a long arc by the intensity ratio of the A I and A II spectral lines, as well as by the intensity ratio of spectral line to background. An exponential fall-off in axial temperature from cathode to anode was reported, along with quasi-isothermal intervals, dips in the temperature profile in the anode sheath region of the arc column. Some interesting findings from temperature field measurements are also to be found in "Stabilized arc in a plasma melting furnace" by the same author, and in "Discussion of axial temperature field in an eddy-stabilized-arc plasmotron," by A. V. Bolotov et al. (Kazakhstan Polytechnic Institute).

Observations of gas flow patterns in a plasmotron end electrode were detailed by A. D. Lebedev et al. (ITAM), "Aerodynamics of a single-chamber eddy-gas-stabilized plasmotron and aerodynamic effects on arc behavior." Visualization of the flow patterns in a transparent plasmotron model was achieved by stirring in oil, sand grains, and dyed water in the gas flow. The gas eddy stream was divided into two zones, the first (closer to the eddy chamber) featuring much greater rotation speeds and axial gas flowspeeds than the second. The zones were separated by an annular eddy device rotating at high speed. The second zone also terminated in an eddy. It is possible for still more zones to exist. A certain functional relationship between the penetration of the first zone in the interior of the electrode, the ratio of the diameters of the end electrode and exit electrode, and the reduced average flowspeed at the plasmotron exit. Experiments conducted on a plasmotron geometrically identical to the above model showed that the position of the arc termination in the end electrode is approximately the same as that of the end of the first zone, if the arc is burning in this electrode with no longitudinal shunting. Similar studies carried out with a two-chamber plasmotron were described by those authors in a companion paper, "Arc voltage regulation in a two-chamber plasmotron by adjusting gas flowrate through eddy chambers."

"Electric field strength in a stabilized arc" by G. Yu. Dautov and M. I. Sazonov (ITAM) cited findings in a dimensionless-criterion treatment of electric field intensity in a sectionalized eddy-stabilized plasmotron. A relationship between the potentials of one interval of arc and plasmotron sections surrounding that interval was established; this relationship is due to an unsustained discharge struck between the arc and the plasmotron sections. The voltage-current curves of that discharge were cited.

"Experimental results on plasmotron arc voltage oscillations" by M. G. Morozov and V. N. Ivanov (Mechanics Research Institute of Moscow State University) pointed out some interesting regularities in the arc shunting process in an eddy-stabilized plasmotron. The effects of polarity and of the dimensions of the exit nozzle on the frequency of voltage ripple and on the shape of shunting oscillograms were dealt with.

"Investigation of electrode sheath phenomena in a moving arc" by V. M. Minorov discussed measurement of the "voltage equivalent" of the heat flow in spots of an arc moving between parallel electrodes in response to a magnetic field, and studies of spot structure and of current density in spots. It was shown that spots break up into a large number of coexisting small spots. The nature of their motion depends on the state of the surface and on electrode polarity. Current density at the cathode is $2 \cdot 10^4$ A/cm^2 and is independent of the velocity of the arc. As the velocity varies from 50 to 150 m/sec, the current density at the anode increases from $1.5 \cdot 10^4$ to $4.5 \cdot 10^4$ A/cm^2. The "voltage equivalents" of the heat flow are 7 V for cathode and 11 V for anode, and are independent of the rate at which the spots move.

"Calculating erosion of cold cathodes in an electric arc" by I. G. Panevin et al. (Moscow S. Ordzhonikidze Aviation Institute) made an attempt to calculate the rate of removal of material from the cathode.

In the view of the authors, the basic contribution to cathode material evaporation is made by internal sources (Joule heating). The results of exploding-wire studies were utilized in calculating metal behavior effects at high current densities (from 10^6 to 10^8 A/cm^2).

The symposium resolution took note of the basic trends evident in research on low-temperature plasma electric arc generators: 1) theoretical studies of interaction between the electric arc, gas flow, and magnetic field in plasmotrons; 2) development of engineering techniques of design using semiempirical theories to account for the behavior of the arc in plasmotrons and to arrive at dimensionless criteria dependences over a wide range of criteria; 3) improved existing techniques and new techniques for precision physical research on the structure of the electric arc under a variety of conditions; 4) theoretical and experimental research on electrode sheath phenomena, erosion of electrodes, the role of electrode materials with different physical properties and design features; 5) the use of transients in plasmotrons.

The symposium noted the absence, throughout the country, of adequate operational information on engineering developments in this field of science. To cope with this, the Institute of Theoretical and Applied Mechanics (IPAM) of the Siberian Division of the USSR Academy of Sciences recommended the organization of an information section on low-temperature plasma generators charged with the task of regularly publishing an information bulletin.

IPAM also suggested scheduling regular symposia on low-temperature plasma generators, with each one centered around a restricted range of related topics.

The symposium proceedings will be published in the periodical Izvestiya Sibirskogo otdeleniya AN SSSR. Tekhnicheskaya seriya [Bulletin of the Siberian Division of the USSR Acad. Sci., Technical series].

CRIMEAN SCHOOL FOR THEORETICAL PHYSICISTS

S. Gerasimov, A. Govorkov,
R. Mir-Kasimov, and V. Zamiralov

The summer International School on the Theory of Elementary Particles, organized under joint auspices of the Academy of Sciences of the Ukrainian SSR and the Dubna Joint Institute for Nuclear Research, was held April 14 through May 5, 1966, at the site not far from Yalta. Participating were about 200 representatives of various scientific institutions in the USSR, Bulgaria, Hungary, the Democratic Republic of Vietnam, the German Democratic Republic, the Chinese Peoples Democratic Republic, Poland, Rumania, Czechoslovakia, and invited guests from Britain, Israel, India, and the USA.

The school's program centered mainly on the theory of symmetries in strong interactions and on the algebra of currents. Some of the reports and papers also shed light on such major problems as breakdown of CP invariance in kaon decay, the solution of dispersion equations, or closed bootstrap solutions, etc.

Many of the reports and lectures were devoted to one of the most thought-provoking hypotheses current in the physics of strong interactions, that of compound models. Lectures by A. N. Tavkhelidze (JINR) reviewed the literature and summarized results on description of the properties of low-lying excited states in baryons and mesons on the basis of the relativistic compound model elaborated by N. N. Bogolyubov and his school. Electromagnetic interactions in the quark model were discussed by A. M. Baldin, V. A. Matveev (JINR), and by V. P. Shelest (Institute of Theoretical Physics, Kiev). Baldin discussed a variant of the theory in which spatial distribution of quarks within the nucleon is concentrated in a region of small radius (on the order of the Compton length of the nucleon), and the observable radius of the nucleon is due mainly to the meson "coat" of the quarks.

The audience was greatly interested in Lipkin's (Israel) lectures on application of the quark model to relationships between interaction cross sections of particles at high energies, proton and antiproton annihilation, renormalization of the axial-vector component in beta decay. Lectures by Marshak (USA) treated the use of the quark model to obtain commutation relations between current operators and generalized charges, lying at the basis of the now highly popular method of algebra of currents.

In a certain sense, the algebra of currents is a new type of symmetry in the theory of elementary particles. In contrast to conventional symmetries, such as isotopic invariance of the eightfold way, the algebra of currents does not presume a classification of particles in terms of irreducible representations of some group, but instead imposes certain commutation relations on physical currents or generalized charges of various fields. A review paper on this theory was presented by A. V. Efremov (JINR). Lectures by I. Yu. Kobzarev and B. L. Ioffe (Institute of Theoretical and Experimental Physics, Moscow [ITEF]) gave detailed accounts of the corollaries deriving from the application of the algebra currents to the study of weak interactions.

Yu. M. Shirokov (Steklov Institute of Mathematics) dealt with the general properties of dynamical moments, of which the currents are a particular case. The intriguing possibility of the existence of conserved tensor currents and their relation to the SU(6) group were discussed by V. I. Ogievetskii and I. V. Polubarinov (JINR).

Mathematical aspects of the theory of noncompact groups were discussed in a series of lectures given by different authors. A cycle of lectures by M. A. Naimark and a lecture by I. M. Gel'fand (Steklov Inst. Math.) dealt with mathematical research on the construction of infinite-dimensional unitary representations of noncompact groups. Lectures by I. T. Todorov (JINR) gave an account of a method for constructing several unitary infinite-dimensional representations of noncompact groups which should be useful in the study of dynamic symmetries. As examples, the author cited oscillator and rotator symmetries, the Chew-Low model, and the hydrogen model. The last example was also discussed in reports

Translated from Atomnaya Énergiya, Vol.21, No.6, pp.525-526, December, 1966.

by V. S. Popov (TEF, Moscow) and Werle (Poland). In the theory of elementary particles, Todorov suggested considering a noncompact group obtained as a semidirect product of a Poincaré group and a group of complex linear transformations in six-dimensional space with a unit determinant, as a dynamical symmetry, thereby generalizing the known static group SU(6). Lectures by Fronsdal (USA) discussed the same relativistic generalization of the SU(6) group.

Relativistic extensions of the static SU(6) group using finite-dimensional representations of noncompact groups run into severe difficulties caused by the required unitarity of the S-matrix. Nguyen Van Hieu (JINR) showed how these difficulties can be obviated in the use of infinite-dimensional representations. Methuse (Britain) pointed out a possible incompatibility between the unitarity and causality requirements of the S-matrix in the group of symmetries including the Poincaré group. Lectures by D. V. Volkov (Physics and Engng. Inst., Khar'kov) discussed finite-dimensional representations of collinear groups deriving from static groups of higher-order symmetries as particles move along a single line.

Numerous topics relating to the applications of one-dimensional dispersion relations without subtractions to determine the electromagnetic properties of baryons were discussed in lectures by L. D. Solov'ev (Institute of High Energy Physics, Serpukhov).

A possible connection between the symmetries of strong interactions between hadrons and dynamical equations in the bootstrap method was reported by P. S. Isaev (JINR).

A. A. Komar (Lebedev Physics Institute of the USSR Acad. Sci.) discussed a general classification of groups currently in use in the theory of elementary particles, in a review paper, and dealt with experimental verification of the groups. Rosenfeld's (USA) lectures containing a survey of the latest experimental data on mesonic and baryonic resonances were greeted with interest.

A survey of theoretical papers on the CP problem (nonconservation of CP parity in K-meson decay) was given by Yu. M. Shirokov. He pointed out the inconsistency of attempts to retain CP invariance in the theory, based on the assumed existence of additional effects simulating CP invariance in the theory (the presence of external galactic fields, the existence of particles similar to the K_2^0-meson and with CP = +1, differences in pion statistics and Bose statistics, etc.).

A review of experimental work on CP parity was given in a lecture by E. O. Okonov (JINR).

An original report by B. A. Arbuzov (Institute of High Energy Physics, Serpukhov) and A. T. Filippov (JINR) was devoted to possible breakdown of CP invariance in a combination of weak and electromagnetic interactions through a change in the usual geometry at close distances. A lecture by V. B. Berestetskii (ITEF, Moscow) presented a review of work on possible violation of C-parity in the interaction of high-spin particles with an electromagnetic field. G. Wick (USA) discussed discrete C, P, and T symmetries and gave information on an original determination of these operations suggested by Wigner, in which the number of components of the wave functions has to be doubled.

V. G. Kadyshevskii, R. M. Muradyan (JINR), and N. N. Achasov (Mathematics Institute of the Siberian Division of the USSR Academy of Sciences, Novosibirsk), reported on possible lepton symmetries.

An attempt to include gravitation in the theory of elementary particles was related by M. A. Markov (JINR).

A communication by D. I. Blokhintsev (JINR) discussed localization of particles in the relativistic theory. D. V. Shirkov (Math. Inst. Siberian Div. USSR Acad. Sci.) gave an account of a dispersion-relations approach to low-energy scattering of hadrons, based on the Mandel'stam representation. The proceedings of the Yalta summer school, supplemented by lectures given by Academician N. N. Bogolyubov on the theory of elementary particle symmetries will be published as a symposium entitled "High energy physics and the theory of elementary particles" by the Naukova dumka press in Kiev.

CONFERENCE ON THE DIFFRACTION TECHNIQUES IN THE STUDY OF CRYSTAL IMPERFECTIONS

O. N. Efimov

A second expanded conference on the study of crystal imperfections by diffraction techniques (x-ray and electron microscope techniques) was held February 2-5, 1966, at the Semiconductor Institute of the USSR Academy of Sciences. The conference attracted over 250 scientists and engineers from different scientific research institutions.

Diffraction techniques for investigating defects have become generally popular in our country and elsewhere in the past few decades. These methods can be used to extract information on the type of defects, their distribution throughout the bulk of the crystal, the nature of stresses introduced by different imperfections into the crystal lattice. The study of crystal imperfections is very much on the order of the day, since many of the physical properties of crystals, semiconductor and laser properties as an example, and the range of applicability of these properties, are determined by imperfections present in the crystals, such as impurity atoms, vacancies and vacancy clusters, and thermal vibrations of the atoms.

The development of diffraction techniques is accompanied by difficulties of its own, the most crucial being the lack of any dynamical theory to account for scattering by crystals having different imperfections. It has been possible to make successful use of one or another acceptable model of crystal scattering in electron microscopic studies of crystals with imperfections, in some cases, but the problem is an extremely involved one in the case of x-ray diffraction, and at present we have no satisfactory quantitative model at all (different models now considered account for only the qualitative aspect of modification of scattering by defect crystals or deformed crystals). The construction of such a rigorous quantum-mechanical theory appears to be in the offing in the near future.

The conference discussed the status of the dynamical theory of scattering by crystals with imperfections, diffraction techniques for studying imperfections in crystals, and progress achieved in practical applications of such techniques. Reports were heard on the general problems in the dynamical theory of scattering related to the study of crystal imperfections (Z. G. Pinsker), fundamentals of techniques in diffraction electron microscopy (V. N. Rozhanskii), the present state of electron microscopic techniques in experimental research on crystal imperfections (L. M. Utevskii). Topographical techniques in the study and interpretation of crystal imperfections were reported on by A. M. Elistratov (since deceased), I. L. Shul'pin, and V. F. Miuskov. Quantitative methods for studying the general degree of perfection of crystals were discussed by the late A. M. Elistratov and by O. N. Efimov. An interesting paper, "Suppression of nuclear reactions in resonance interaction of particles with nuclei in ideal crystals (nuclear anomalous absorption effect in crystals)", was presented by Yu. M. Kagan and A. M. Afanas'ev, who demonstrated the possible existence of such an effect and gave an explanation for it.

Several original papers on electron microscopy were also presented: one on diffraction contrast from twins in martensite, and on precipitations of a second phase in nimonic type alloy; one on the study of dislocations accompanying crystal growth, or appearing in various processes applied to specimens and imperfections, and on dislocations forming in the breakdown of metallic solid solutions at different stages.

Reports on work involving diffuse scattering of x-rays reported applications to the study of the structure of decaying solid solutions (using the example of ionic and metallic solid solutions), and based on the current kinematical theory of scattering.

Quite a few papers were devoted to the study of defects in almost perfect crystals by methods based on dynamical effects. Among these are topographical x-ray techniques (Borrman, Lang, Berg-Barrett, Fujiwara, Kossel) and quantitative x-ray techniques (involving integral characteristics and absorption discontinuities). In contrast to the preceding conference, at which work on the study of imperfections in

Translated from Atomnaya Energiya, Vol. 21, No. 6, pp. 526-527, December, 1966.

germanium and silicon dominated the discussion, the 1966 conference was more representative of the increasing number of problems being solved and tackled in research, at a level which can make increasing use of dynamical techniques. The scope of practical problems now includes germanium and silicon single crystals, Al_2O_3 crystals, artificial quartz, ammonium and potassium dihydrophosphate crystals, various epitaxial films, etc.

The reports dealt with the most pressing problems in research on crystal imperfections encountered in the growing of perfect single crystals and epitaxial films, in the fabrication of diffusion instruments, in radiation studies, and in other fields.

Several papers were devoted to quantitative treatment of the overall degree of perfection of crystals containing imperfections such as radiation defects, vacancies and vacancy clusters, thermal vibrations of atoms.

The conference should stimulate an expansion of experimental and theoretical work capable of solving not only purely theoretical problems in the physics of real crystals, but also practical problems in a variety of fields of contemporary engineering and industry where perfect single crystals are required.

SYMPOSIUM ON THE DISPOSAL OF RADIOACTIVE WASTES IN SEAS, OCEANS, AND SURFACE WATERS

V. M. Vdovenko, L. I. Gedeonov,
and P. M. Chulkov

The International Atomic Energy Agency held a symposium in Vienna, May 16-20, 1966, to discuss the disposal of radioactive wastes in the seas, oceans, and surface waters of the world. The symposium was attended by 160 scientists from 25 countries and from five international agencies.

Reports fell into three groups.

The first group included 29 papers devoted to physical and biological transport of isotopes in the disposal of radioactive wastes in seas, oceans, and surface waters. These papers dealt with dilution, dispersion, precipitation, absorption of radioactive materials by organisms in rivers and in various land-locked water reservoirs. They also reported results of research on the migration of artificially radioactive isotopes and, in this context, on the turbulent diffusion of water masses at the mouths and estuaries of rivers, gulfs and inlets, and coastal waters at waste disposal sites, as well as propagation of radioisotopes in the open sea or ocean.

The second group of papers analyzed human exposure to radiation as a result of the disposal of radioactive wastes in seas, oceans, and surface waters. The flow of radioactive isotopes through food cycles and their incorporation in food cycles through irrigation, external radiation dosage and exposure estimates for individuals or groups through the disposal of radioactive wastes in the water environment were studied. Several reports dealt with programs and research findings preceding the research on radioactive waste disposal at sea.

A third group of papers dealt with the possible effect of radioactive wastes on the resources of the seas, oceans, and surface waters. The somatic effect of radiation exposure on aquatic organisms and the genetic results affecting populations of aquatic organisms were investigated in these papers.

A large number of the papers dealt with radioecological and radiobiological problems.

We realize from a perusal of the symposium materials that disposal of radioactive wastes in seas or rivers is still a common practice. Reports were made on the disposal of wastes into the Columbia, Clinch, and Tennessee rivers (USA); into the Solway Firth inlet; into the mouth of the Blackwater river (Britain); into the North Sea in the Petten area near Amsterdam (Netherlands); in the Rhône river (France); in the Tvären Gulf on the Baltic Sea (Sweden). Sea disposals in the Trombay area near Bombay (India) are also known. Extensive research on the degree of dilution of waste simulants has been carried out at Cape Ag (France), where a large spent-fuel reprocessing plant is soon to go into operation.

The greatest volume of radioactive-waste disposal in sea water is at Windscale (Britain), where the activity runs into tens of thousands of curies annually in total beta-activity.

All the countries disposing of radioactive wastes in open waters are engaged in extensive dosimetric monitoring programs and scientific research programs applying modern techniques (multidimensional gamma-ray spectrometry) and sophisticated instrumentation and equipment: ships, specially designed equipment, large-scale simulated plants. Experiments involving mass tagging of fish and marine animals, as well as radioecological experiments in specially set aside natural water reservoirs, are in progress. This work is accompanied by observations and monitoring of global radioactive fallout levels.

Many investigators in capitalist countries have failed to take proper notice of the threat of proliferation of local radioactive contamination into global proportions as a result of continued expanded use

Translated from Atomnaya Énergiya, Vol. 21, No. 6, pp. 527-528, December, 1966.

of atomic energy and the projected increase in the number of plants reprocessing spent nuclear fuel. The local situation is assessed as a favorable one in the reports submitted by these scientists. A degree of alarm is noted only in contributions made by West Germans.

Soviet scientists have always insisted that the problem of disposal of radioactive wastes in seas, oceans, and surface waters must be approached as a problem of international import.

This point of view, expressed by the majority of specialists in the Soviet Union, is now shared by a considerable portion of investigators in the socialist countries and by some scientists in those countries where the sea and its resources play an important economic role. The viewpoint is based on the fact that the disposal of industrial radioactive wastes in open waters, seas, and oceans is considered inadmissible in view of the potential hazard of worldwide radioactive pollution, the possible consequences of which could be danger to ocean resources and to humans, in the light of data now available. Dumping radioactive wastes in territorial waters cannot be considered merely an internal matter of each government, since radioactive materials can cause harm to the population of neighboring states, and to the resources of international waters as a whole, through migration.

A fully developed presentation of the opinions of Soviet specialists may be found in articles by V. P. Spitsyn and B. S. Kolychev (Atomnaya Énergiya, 9, 58 (1960); 10, 634 (1961)).

The opposite point of view is that of representatives of countries with small and densely populated territory. The viewpoints of scientists from such countries is expressed most clearly in the writings and statements of G. J. Dunster (Britain). On the scientific and technical plane, this viewpoint holds that disposal of wastes in surface water systems and at sea can be organized with proper observance of public health and hygiene norms and with no hazard to the resources of seas and oceans. A careful study need only be made of possible consequences of waste disposal with a view to preventing hazardous conditions. On the juridical plane, the viewpoint holds that we are dealing so far only with disposal of radioactive wastes in internal water reservoirs and territorial waters, and that as long as this is the case the problem of the possible radiation environment resulting is the internal affair of each state. In cases where radioactive wastes go beyond the limits of territorial waters and get into international waters, we can be guided by article 25 of the April 29, 1958 Convention on the Open Seas, according to which nations are obligated to observe all rules and regulations which may be elaborated by the competent international agencies.

The data reported at this symposium are evidence that disposal of radioactive wastes in the ocean and in other open water systems have aggravated radioactive pollution of the ocean to such an extent that it now merits immediate attention.

For example, the bottom sediments of the Columbia River (USA) alone contain isotopes with activity in the neighborhood of 30,000 Ci. Sr^{90} activity in the Clinch river (USA) amounts to about 1110 Ci. The plutonium production plant at Marcoule (France), which has been on stream for over seven years at this writing, dumped 2584 Ci of waste effluent activity into the Rhone river in 1965. The Windscale plant (Britain) disposes of beta-active isotopes with a total activity in the neighborhood of 50 kCi annually at sea. No exact information was presented at the symposium on the total amount of wastes disposed of, including burial of medium-level wastes at sea and disposal of high-activity wastes in containers.

The development outlook for nuclear power and the rates of growth of total reactor output on a worldwide basis in the future must be known in order to forecast the amount of radioactive wastes to be disposed of. The solution of this problem in a first approximation is achievable through analysis of Kr^{85} content in the world atmosphere. Rapid development of nuclear production worldwide will render the problem of radioactive wastes disposal even more acute in the very near future.

INDEX

SOVIET ATOMIC ENERGY

Volumes 20 and 21, 1966

SOVIET ATOMIC ENERGY
Volumes 20 and 21, 1966
A translation of Atomnaya Énergiya)

L

M

Z

TABLE OF CONTENTS

SOVIET ATOMIC ENERGY

Volumes 20 and 21, 1966

(A translation of Atomnaya Énergiya)

Volume 20, Number 1 January, 1966

Volume 20, Number 2 February, 1966

Engl./Russ.

Volume 20, Number 3 March, 1966

Volume 20, Number 4 April, 1966

Volume 20, Number 5 May, 1966

Volume 20, Number 6 June, 1966

Volume 21, Number 1 July, 1966

Volume 21, Number 2 August, 1966

Volume 21, Number 3 September, 1966

Volume 21, Number 4 October, 1966

Volume 21, Number 5 November, 1966

Volume 21, Number 6 December, 1966

NOTE

This index lists all material that appears in the original Russian journal. Items originally published in English or generally available in the West are not included in the translation and are shown in brackets. Whenever possible, the English-language source containing the omitted items is given.

Crystallization Processes

Edited by N. N. Sirota, F. K. Gorskii and V. M. Varikash

Institute of Solid State Physics and Semiconductors Academy of Sciences of the Belorussian SSR, Minsk.

Translated from Russian by Geoffrey D. Archard
Corrected by the editors for the American edition.

Devoted to a consideration of the mechanism and kinetics of crystallization and the production of single-crystal semiconductor materials, their purification and the controlled distribution of impurities. Several articles in this important new volume cover theoretical and experimental aspects of the relief and the state of the surface of growing crystals and the surface energy at crystal-melt boundaries. Attention is given to the competing mechanism in crystallization processes, compared with experimental data on the temperature-dependence of crystallization parameters, the linear velocity of crystallization, and the rate of crystal growth. A number of papers consider the structural and kinetic laws of crystal dissolution and the role of the structure of liquids in crystallization processes.

Most of the articles in this collection were presented at the All-Union Conference on the Theory of Crystallization, Thermodynamics, and the Kinetics of Phase Transformations. Translated from a four-part Russian volume, *Mechanism and Kinetics of Crystallization*, the present work comprises two of the sections. The remaining two parts are being published simultaneously in a translation entitled *Solid State Transformations*. The Russian text from which the translation was prepared was thoroughly corrected by the editors.

169 pages

Crystallization Processes: $22.50

Solid State Transformations: $22.50

Set Price: $40.00

CONSULTANTS BUREAU 227 West 17th Street, New York, New York 10011

A DIVISION OF PLENUM PUBLISHING CORPORATION